

Turbulence Modeling for Heated Developing Supercritical Flows

Atharv Naik

Master of Science Thesis

Turbulence Modeling for Heated Developing Supercritical Flows

MASTER OF SCIENCE THESIS

For the degree of Master of Science in Energy, Flow and Process
Technology at Delft University of Technology

Atharv Naik

September 24, 2023

DELFT UNIVERSITY OF TECHNOLOGY
DEPARTMENT OF
PROCESS AND ENERGY

The undersigned hereby certify that they have read and recommend to
the Faculty of Mechanical, Maritime and Materials Engineering (3mE)
for acceptance of the thesis entitled

**Turbulence Modeling for Heated Developing
Supercritical Flows**

by

ATHARV NAIK

in partial fulfillment of the requirements for the degree of
MASTER OF SCIENCE.

Dated: September 24, 2023

Supervisor(s):

Prof.dr. R. Pecnik

Ir. A.M. Hasan

Reader(s):

Prof.dr.ir. BJ Boersma

Dr.ir. J.W.R. Peeters

Abstract

In recent years, a considerable amount of research has been directed towards making energy generation more efficient to combat global warming. To aid this goal, the use of supercritical fluids (SCFs) is gaining a lot of traction. SCFs have only one phase and experience a sharp variation of thermophysical properties when heated sufficiently. These facts can be exploited to gain several advantages over conventionally used sub-critical fluids. However, the strong property variation in heated SCFs also complicates the flow Physics considerably if the wall heating is strong enough. Further, the flows in such settings are often turbulent and spatially developing. For these flows, a strong variation of properties can lead to a modulation of turbulence, which the conventional turbulence models can not predict well. This thesis is an attempt to better understand how spatially developing heated supercritical turbulent flows behave and use this understanding to improve turbulence model predictions.

In this thesis, we investigate two supercritical heated developing turbulent flows from Nemati et al. (2015) [1]. One case is oriented horizontally and the other is oriented vertically. The latter has an additional effect of buoyancy resulting from its vertical orientation and strong density variation near the wall. We analyze how the strong property variation modulates the turbulence in both cases. Then, we assess if Semi-Local Scaling (SLS) and Apparent Reynolds Number (ARN) theories can characterize the modulated turbulence. Further, we propose a methodology to make use of ARN by itself, and in combination with SLS to improve turbulence model predictions.

The results indicate that ARN theory provides a robust way to sensitize conventional turbulence models to the additional effects arising in supercritical heated developing turbulent flows due to property variation. Additional research in turbulent heat flux modeling is deemed necessary to improve the model performance further.

Acknowledgements

Needless to say, this thesis journey has been the most challenging endeavour I have undertaken in my life. It has taught me to be more patient, more perseverant and to put in the work without worrying too much about results. While I am grateful towards my fate for nudging me towards this journey, I am even more grateful towards the people who have supported me throughout the course of this journey. The next couple of paragraphs will be my humble attempt to pen down these feelings of gratitude.

I would like to thank my supervisor Prof.dr. Rene Pecnik for trusting me with this topic and providing me with much-needed support and guidance. I would also like to thank my daily supervisor Ir. Asif Hasan for facilitating enlightening discussions, showing faith in me, and most importantly, being patient with me. Both of my supervisors have played another important role in my journey - inspiring me by showcasing their brilliance, which I am thankful for, and in awe of. I would further like to thank Dr. Jundi He for helping me understand ARN theory and sharing the data from his paper. I would also like to express my sincere gratitude towards Prof.dr. B.J. Boersma, and Dr. Jurriaan Peeters for being a part of my thesis committee and taking time out to read my thesis.

To say that the past two years have been full of ups and downs would be an understatement. I would like to thank my family for always having my back through thick and thin. Without their support, I would never have been able to chase my dreams. In the same vein, I would like to thank my friends for being my family away from home. Without their love, patience, and emotional support, I doubt if I would have made it to the finish line.

Delft, University of Technology
September 24, 2023

Atharv Naik

"If something burns your soul with purpose and desire, it's your duty to be reduced to ashes by it. Any other form of existence will be yet another dull book in the library of life."

- *Charles Bukowski*

Table of Contents

1	Introduction	1
1-1	Background	2
1-1-1	Supercritical Fluids	2
1-1-2	How property variation affects turbulent flows	3
1-1-3	Influence of buoyancy and thermal acceleration on turbulence	5
1-1-4	How property variation affects heat transfer	6
1-1-5	Heat transfer deterioration and heat transfer recovery regimes	8
1-2	Advancements in turbulence modeling for buoyancy and thermal acceleration affected flows	8
1-3	Semi Local Scaling	11
1-4	Apparent Reynolds Number theory	11
1-5	Research objectives, scope, and goal	13
2	Theoretical Framework	15
2-1	Governing equations: Instantaneous Form	15
2-1-1	Non-dimensional form	17
2-2	Governing equations: Reynolds Averaged Navier -Stokes (RANS)	19
2-3	Turbulence Modeling	21
2-3-1	Modeled RANS governing equations	23
2-3-2	Turbulent Kinetic Energy	24
3	Numerical set-up	26
3-1	Simulation domain	26
3-2	Numerical method	27
4	Case Description and Discussion	29
4-1	Case description	29
4-2	Discussion	31
4-2-1	Effects of property variation on both cases	31
4-2-2	Semi-local scaling	34
4-2-3	ARN theory	37
4-2-4	Simultaneous application of SLS and ARN theories	39
5	Methodology	40
5-1	ARN theory	40

5-2	Reconstruction of flow field using ARN theory	43
5-3	ARN theory to improve RANS models	44
5-4	Combining SLS and ARN theories	45
6	Results and Discussion	47
6-1	Case A	47
6-1-1	MK turbulence model	48
6-1-2	SA Turbulence model	51
6-1-3	$k - \omega$ SST turbulence model	54
6-2	Case B	56
6-2-1	MK turbulence model	57
6-2-2	SA turbulence model	59
6-2-3	$k - \omega$ SST turbulence model	62
7	Summary and Conclusions	66
A		68
A-1	Experiments, Turbulence models and Working Fluids for the numerical studies	68
B		69
B-1	Modeled turbulent transport equations	69
B-1-1	Myong-Kasagi turbulence model	69
B-1-2	Menter's $k - \omega$ SST turbulence model	70
B-1-3	Spalart-Allmaras turbulence model	70
B-2	Semi-Locally scaled transport equations	71
B-2-1	Myong Kasagi turbulence model	71
B-2-2	Menter's $k - \omega$ SST turbulence model	72
B-2-3	Spalart-Allmaras turbulence model	72
C		73
C-1	RANS Code Validation	73
	Bibliography	74

List of Figures

1-1	Phase diagram of Water [2]	2
1-2	Variation of c_p , ρ , μ , and λ for Water, at various supercritical pressures [3] .	3
1-3	A unified explanation for flow laminarisation in heated flows [4]	12
3-1	Computational domain for the RANS simulations	26
3-2	Staggered mesh cell	27
4-1	Bulk velocity, density and viscosity vs z/D for Cases A and B	30
4-2	Re_τ vs z/D for Cases A and B	30
4-3	Re_τ^* vs y for Cases A and B.	31
4-4	$\tilde{u}_z/u_{\tau,0}$ vs y^{+0} for Cases A and B	31
4-5	$-2\rho\overline{u_r''u_z''}\frac{\partial\tilde{u}_z}{\partial r}$ vs y for cases A and B.	32
4-6	$-\rho\overline{u_r''u_r''}\frac{\partial\tilde{u}_z}{\partial r}$ vs y for cases A and B.	32
4-7	$\overline{\rho u_r''u_r''}$ vs y for cases A and B.	33
4-8	$\overline{\rho u_\theta''u_\theta''}$ vs y for cases A and B.	33
4-9	$\nu_t/\nu_{w,0}$ vs y^{+0} for cases A and B.	34
4-10	SLS turbulent stresses vs y^* for cases A and B	36
4-11	Wall normal Reynolds stress anisotropy vs y^* for cases A and B	37
4-12	Wall normal Reynolds stress anisotropy vs y^* for cases A and B	37
4-13	SLS viscous stresses vs y^* for cases A and B	38
4-14	Eddy viscosity scaled with centerline viscosity vs y^{+1} for cases A and B	38
4-15	Eddy viscosity scaled with centerline viscosity vs y^+ for cases A and B	38
4-16	Eddy viscosity scaled with locally averaged viscosity vs y^{*1} for cases A and B	39
5-1	Streamwise mean momentum budget, case B [1]	43
6-1	Eddy viscosity and streamwise velocity (Case A, MK).	48
6-2	Radial temperature profile and Radial turbulent heat flux (Case A, MK). . . .	49
6-3	Wall temperature comparison (Case A, MK).	50

6-4	Wall temperature comparison (Case A, SA).	51
6-5	Eddy viscosity and streamwise velocity (Case A, SA).	52
6-6	Radial temperature profile and Radial turbulent heat flux (Case A, SA).	53
6-7	Eddy viscosity and streamwise velocity (Case A, SST).	54
6-8	Radial temperature profile and Radial turbulent heat flux (Case A, SST).	55
6-9	Wall temperature comparison (Case A, SST).	56
6-10	Eddy viscosity and streamwise velocity (Case B, MK).	57
6-11	Radial temperature profile and Radial turbulent heat flux (Case B, MK).	58
6-12	Wall temperature comparison (Case B, MK).	59
6-13	Eddy viscosity and streamwise velocity (Case B, SA).	60
6-14	Radial temperature profile and Radial turbulent heat flux (Case B, SA).	61
6-15	Wall temperature comparison (Case B, SA).	62
6-16	Wall temperature comparison (Case B, SST).	62
6-17	Eddy viscosity and streamwise velocity (Case B, SST).	63
6-18	Radial temperature profile and Radial turbulent heat flux (Case B, SST).	64
C-1	Validation: streamwise velocity vs y^+	73
C-2	Validation: Reynolds shear stress vs y	73

Chapter 1

Introduction

Global warming is arguably one of the biggest issues that we face in the current day and age. This problem is exacerbated by the use of fossil fuels in the energy industry. To tackle this problem, there needs to be a complete transition to renewable sources of energy. However, what impedes this transition is the intermittency of renewable energy sources. A considerable amount of research in the fields of large-scale energy storage and renewable energy is needed in order to completely rely on the latter. Nuclear energy offers a viable alternative because it does not contribute to greenhouse gas emissions. It can be utilized for mitigating fossil fuel dependence and thus, can aid the energy transition process.

In the Nuclear power plants, even though the mode of heat generation is different, the end goal is to drive steam turbines. The conventionally used pressurized water reactors (PWRs) in the nuclear energy sector make use of subcritical water at high pressure as a primary coolant for the reactor core. This primary coolant heats up the secondary coolant which is at a lower pressure, in order to generate steam. In contrast to this, the Supercritical Water-cooled Reactors (SCWRs) make use of supercritical fluids (SCFs) as the primary coolant. This provides a huge advantage, as SCFs do not have the problem of boiling crisis (due to phase change) encountered in subcritical fluids [5]. This is because SCFs only have one phase.

However, when SCFs are strongly heated, they display a very sharp variation of thermophysical properties. This happens around the ‘pseudo-critical temperature’. Because of this, they display peculiar heat transfer characteristics and complicated flow physics around the pseudo-critical temperature. This is a phenomenon that needs to be understood and predicted well to design systems such as SCWRs. This is a pressing problem as it will help reduce the dependence on fossil fuels.

The conventional turbulence models are unable to give a good prediction of heated developing supercritical turbulent flows around the pseudo-critical temperature. This problem is related to the strong variation of thermophysical properties and will be discussed in the following sections. This thesis aims to better understand the flow physics of heated developing supercritical turbulent flows and use this understanding to improve the performance of conventional turbulence models.

The following sections will give the necessary background knowledge required to understand this thesis. This will be followed by an assessment of relevant literature, the definition of the research objectives, the scope, and the goal of this thesis.

1-1 Background

1-1-1 Supercritical Fluids

A fluid is said to be in the ‘supercritical’ state when it is at pressures and temperatures that are higher than their critical values. The critical point is the point above which the distinction between liquid and gaseous phases ceases to exist; there is only one phase: the supercritical phase.

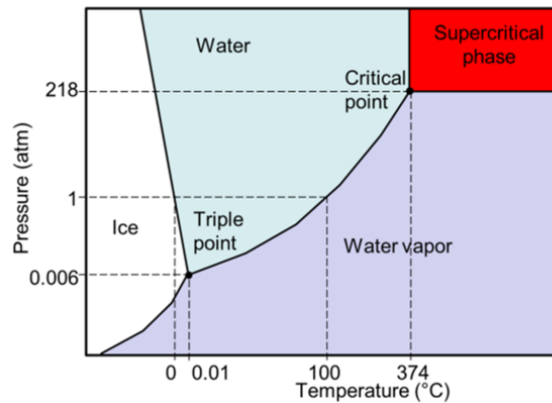


Figure 1-1: Phase diagram of Water [2]

At subcritical conditions, we get a so-called first-order phase transition, wherein the density changes in a discontinuous manner across the phase boundary. The two states involved can co-exist in equilibrium at the phase boundary indicated by a solid black line in figure 1-1. Upon moving beyond the critical point, we get a second-order phase transition. Here, a continuous change in density and other thermophysical properties is observed. The fluid transitions between a liquid-like and a gas-like state.

Thus, by altering the pressure and the temperature of the fluid in the supercritical region, one can get a gas-like or a liquid-like property variation. The regions of these two types of variation are separated by the Widom Line, which is the locus of pseudocritical temperatures (T_{pc} ; explained below) for different critical pressures.

Variation of properties in supercritical fluids

The thermophysical properties (including transport properties) of fluids undergo a drastic change in their values in a very narrow range, around the pseudo-critical temperature (T_{pc}). T_{pc} is defined as the point at which the specific heat (c_p) is maximum for a given supercritical pressure. The trend of the variation in density (ρ), viscosity (μ), thermal conductivity (λ) and c_p around T_{pc} can be observed in figure 1-2, from [3].

Thus, the fluid properties show a very strong dependence on temperature near T_{pc} . The governing equations for fluid flow undergoing heat transfer near T_{pc} are strongly coupled. As a result of this, we get strong non-ideal fluid behavior and peculiar heat transfer characteristics in the said region.

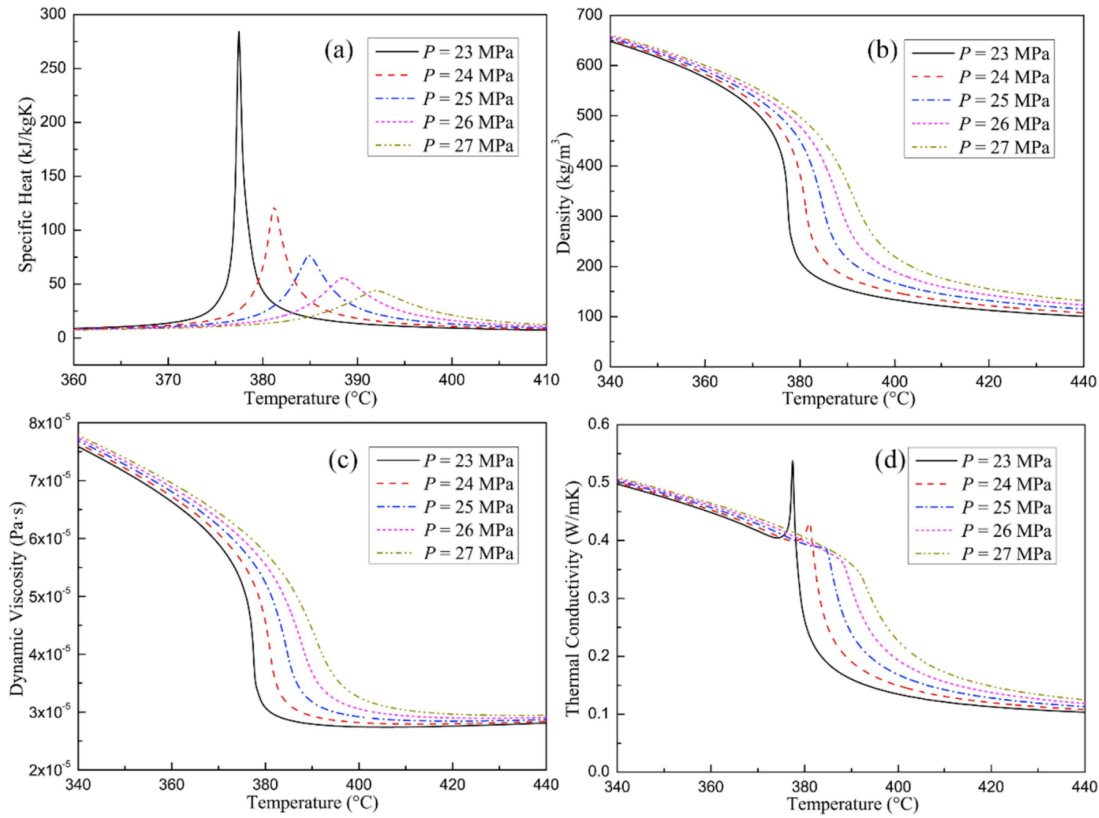


Figure 1-2: Variation of c_p , ρ , μ , and λ for Water, at various supercritical pressures [3]

1-1-2 How property variation affects turbulent flows

Traditionally, temperature has been treated as a passive scalar that does not influence the flow field. Energy equations are solved alongside momentum equations only when knowledge of the thermal field is required. However, in cases similar to the above-mentioned, the variation of thermophysical properties due to heating is so strong that it modulates turbulence and temperature no longer remains a ‘passive scalar’.

A plethora of industrial turbulent flows are subjected to a heat flux at the wall, which causes the wall temperature (T_w) to increase compared to the bulk temperature (T_b). If the wall heating is strong enough, it raises the temperature of the near-wall fluid close to T_{pc} , while the bulk temperature (T_b) remains below T_{pc} ($T_b < T_{pc} < T_w$). Consequently, a strong property variation is observed near the wall. A short explanation of how the near wall variation in properties, namely density and viscosity affect turbulent flows for such a case will be given below, on the basis of [4].

The explanation will be made from the perspective of a *turbulent pipe flow in the upward direction (against gravity) subjected to a high enough wall heat flux*. Also, this explanation only refers to the variation of averaged properties, not the fluctuations. The concept of averaging will be discussed in section 2-2 of the next chapter. The reference fluid is supercritical water (SCW), from figure 1-2. Extrapolation to other types of flows should be done considering the frame of reference, trends of property variation, and flow direction using the same general principles.

Effects of strong property variation on turbulent flows

Near wall acceleration of fluid

- **Density variation**

- **Buoyancy**

For this explanation, we assume $T_b < T_{pc} < T_w$. From figure 1-2, the density of SCW decreases drastically near T_{pc} . Thus, upon moving from the pipe centerline to the wall, the fluid density will drastically reduce. Consequently, the gravity force acting on the fluid in the near-wall region decreases. As a result, the near-wall fluid accelerates in the streamwise direction non-uniformly depending on the local density. This effect is limited to flows that aren't horizontally oriented.

- **Reduced turbulent shear stress**

Due to the strong reduction of density near the wall, there is a reduction in turbulent shear stresses ($\overline{\rho u''_z u''_r}$), which in turn reduces the flow resistance. This leads to a near-wall flow acceleration in the streamwise direction.

- **Viscosity variation**

- **Reduction in viscous friction**

From the figure 1-2, the viscosity of fluid also decreases drastically as T_{pc} approaches. Thus, near the wall, the friction due to viscosity decreases. As a result, there is a local flow acceleration in the streamwise direction.

Reduction of streamwise pressure gradient

In response to the local flow acceleration, the streamwise pressure gradient driving the flow reduces in order to maintain a constant mass flow rate. This effect has a tendency to cause a uniform cross-sectional bulk flow deceleration.

Axial fluid expansion (Thermal acceleration)

The increase in T_b along the streamwise direction due to wall heating leads to a decrease in the bulk density of the fluid. In response to this, the bulk velocity increases to maintain mass conservation. This causes a uniform cross-sectional acceleration of the bulk flow. Since the effects of this phenomenon are not local and are mass-conserving, it does not modify the pressure gradient.

No slip boundary condition at the wall

In this explanation, the local property variation eventually leads to a bulk flow deceleration. Whereas a reduction in bulk density necessitates bulk flow acceleration. Based on which effect is more dominant, we have a net deceleration/acceleration of the bulk flow. However, due to the no-slip condition, the effects of viscosity cause a lower localized deceleration/acceleration near the wall. The opposition of the tendency of the fluid to undergo a bulk acceleration/deceleration by no slip gives rise to non-uniform inertia force in the flow.

Modification of the streamwise velocity profile

A local flow acceleration can lead to uniform bulk deceleration, and the latter is less effective in the vicinity of the wall. Thus, we get a velocity profile that becomes progressively steeper in the vicinity of the wall and flatter in the core. If this effect is very strong and the domain is long enough, an ‘M-shaped’ velocity profile is obtained eventually.

The contribution of ‘buoyancy’ to this effect is known as the ‘indirect effect of buoyancy’. In the following subsection, we will describe how this in addition to thermal acceleration affects the shear production of turbulence. Although we will only address buoyancy and thermal acceleration, the reader can make extrapolations about all the effects mentioned above. Also, when the heat flux is very strong, density fluctuations can become important and provide an additional source/sink of turbulence. This is known as the ‘direct effect of buoyancy’, and will also be discussed.

1-1-3 Influence of buoyancy and thermal acceleration on turbulence

Indirect (external) effect

In general, external buoyancy effects are due to radial gradients in density, whereas thermal acceleration effects are due to axial gradients in density [6]. As discussed, the presence of wall-normal density gradients in the vicinity of the wall leads to near-wall acceleration and core deceleration. To reiterate, this statement is for non-horizontal flows. Consider the Production terms of Turbulent Kinetic Energy (TKE) and Reynolds shear stress (in radial coordinate system) [7]:

$$P_k = -\overline{\rho u_r'' u_r''} \frac{\partial \tilde{u}_r}{\partial r} - \overline{\rho u_r'' u_z''} \frac{\partial \tilde{u}_r}{\partial z} - \frac{\tilde{u}_r \overline{\rho u_\theta'' u_\theta''}}{r} - \overline{\rho u_r'' u_z''} \frac{\partial \tilde{u}_z}{\partial r} - \overline{\rho u_z'' u_z''} \frac{\partial \tilde{u}_z}{\partial z}, \quad (1-1)$$

$$P \frac{\overline{\rho u_r'' u_z''}}{\rho u_r'' u_z''} = -\overline{\rho u_r'' u_r''} \frac{\partial \tilde{u}_z}{\partial r} - \overline{\rho u_z'' u_z''} \frac{\partial \tilde{u}_r}{\partial z} - \overline{\rho u_z'' u_r''} \frac{\partial \tilde{u}_r}{\partial r} - \overline{\rho u_r'' u_z''} \frac{\partial \tilde{u}_z}{\partial z}. \quad (1-2)$$

Terms containing wall normal gradient of streamwise velocity

When there is no flow acceleration, the dominant terms in the P_k and $P \frac{\overline{\rho u_r'' u_z''}}{\rho u_r'' u_z''}$ equations are $-\overline{\rho u_r'' u_z''} \frac{\partial \tilde{u}_z}{\partial r}$ and $-\overline{\rho u_r'' u_r''} \frac{\partial \tilde{u}_z}{\partial r}$, respectively. Due to the indirect effects of buoyancy, the magnitude of $\frac{\partial \tilde{u}_z}{\partial r}$ increases in the viscosity-dominated region (where it only contributes slightly to turbulent production). Also, it reduces away from the wall (where it progressively decreases the production).

Terms containing the streamwise gradient of streamwise velocity

Due to thermal acceleration, the terms $-\overline{\rho u_z'' u_z''} \frac{\partial \tilde{u}_z}{\partial z}$ and $-\overline{\rho u_r'' u_z''} \frac{\partial \tilde{u}_z}{\partial z}$ from equations 1-1 and 1-2 can also become important. Since thermal acceleration leads to $\frac{\partial \tilde{u}_z}{\partial z} > 0$, this can cause a reduction in the magnitude of P_k and $P \frac{\overline{\rho u_r'' u_z''}}{\rho u_r'' u_z''}$.

The production of streamwise Reynolds stresses takes place through shear. Then, energy is transferred to the wall-normal and spanwise Reynolds stresses through the return to isotropy term. Thus, a reduction in streamwise Reynolds stresses will lead to a reduction in spanwise and wall-normal Reynolds stresses as well. Due to this, there will be an overall reduction in TKE and thus turbulence levels.

Direct (structural) effects

Often, the effects of density fluctuations are ignored in the analysis of turbulent flows. This is because, in most low Mach number cases, turbulent flows can be characterized properly as long as the mean property variations are taken into account (Morkovin's hypothesis of the negligible effect of density fluctuations [8]). However, density fluctuations are important in the generation of vortices in the streamwise direction [9]. As a result, density fluctuations can play a role in affecting the near-wall regeneration of turbulence and cause an attenuation of the same. In certain flows with a high amount of wall heating, the turbulence can not be characterized well by just considering the variation of averaged properties.

The source term arising due to the correlation of density fluctuations with other quantities is called the Buoyancy Production term, and for TKE is given by:

$$G_k \approx \frac{1}{Fr_0} \overline{\rho' u'_z}. \quad (1-3)$$

If we have a flow that is heated/cooled such that $\frac{\partial \rho}{\partial z} > 0$, we get an unstably stratified flow and vice versa for stable stratification. Whether the above-mentioned term acts as a source or a sink will depend upon the nature of the stratification of the flow.

Consider a fluid particle in an upward flow, that is displaced by a positive u'_z (thus, upwards). If we have stable stratification, it will be transported into a region of lower density. The buoyancy force will push the higher-density particle back to its original position, effectively damping the turbulent fluctuation [7]. On the other hand, if a fluid particle is transported upwards by u'_z in a region of higher density (unstable stratification), buoyancy force will aid the process, and effectively contribute to the turbulence. Therefore, G_k acts as a source in unstably stratified flows, and as a sink in stably stratified flows.

A general idea of how the variation in thermophysical properties eventually leads to a modification in turbulence can be obtained from the above explanation. Properties do not always have to vary in the same way as the example. However, depending on the nature of the variation, extrapolations can be made. Similar to turbulence, the heat transfer characteristics of the flows are also affected by property variation. The same will be elaborated upon below.

1-1-4 How property variation affects heat transfer

In industrial applications where fluid flows are used as a medium of heat transfer, convective heat transfer is usually the most prevalent. Convective heat transfer takes place through the motion of the fluid flow and consists of two components: conduction (heat diffusion) and advection (bulk motion of fluid). In turbulent flows, we have an additional mechanism of turbulent mixing. This subsection will outline how property variation directly/ indirectly influences these heat transfer mechanisms.

Direct influence of property variation

For forced convection cases, the experimentally fitted Dittus-Boelter correlation [10] is used to obtain the Nusselt number as:

$$Nu = 0.023 Re_b^{0.8} Pr_b^{0.4}. \quad (1-4)$$

Heat transfer coefficient (h_c) for a pipe with diameter D can be obtained from Nu using:

$$h_c = Nu \times (\lambda_b/D). \quad (1-5)$$

The mass flow rate for a pipe flow can be given by:

$$\dot{m} = \pi/4 \times \rho_b u_b D^2. \quad (1-6)$$

Plugging (1-5), (1-6), $Re_b = \frac{\rho_b u_b D}{\mu_b}$, $Pr_b = \frac{\mu_b c_{p,b}}{\lambda_b}$ into (1-4), we get:

$$h_c = (0.028 \times \dot{m}^{0.8} / D^{1.8}) \times (\lambda_b^{0.6} \mu_b^{-0.4} c_{p,b}^{0.4}). \quad (1-7)$$

Thus, for a constant mass flux and pipe diameter:

- h_c increases with an increase in λ_b .
- h_c increases with a decrease in μ_b .
- h_c increases with an increase in $c_{p,b}$.

When the wall heating for supercritical flows is considerably high, we get a strong property variation near the wall. As explained before, this leads to a modulation of the flow itself. In such cases, the effects of property variation on h_c can no longer be analyzed by isolating the effects of individual properties.

Indirect influence of property variation on Laminar convection

As discussed, property variation can lead to near-wall acceleration/ deceleration. In a laminar case, near-wall flow acceleration will aid the advection of heat and will improve heat transfer. Effects will be the opposite for near-wall deceleration. In the case of individual properties varying in opposite ways, the total effect will depend on whether we have a net acceleration or deceleration. Laminar flows are not relevant to this thesis, and will not be mentioned further.

Indirect influence of property variation on Turbulent convection

Heat transfer in a turbulent flow is dominated by turbulent mixing. Even though near-wall acceleration increases the velocity near the wall, it causes an overall reduction in the production of turbulence as discussed above. Consequently, the heat transfer effectiveness decreases in turbulent flows due to acceleration caused by property variations. A near-wall deceleration has the opposite effect and enhances the heat transfer effectiveness in turbulent flows.

1-1-5 Heat transfer deterioration and heat transfer recovery regimes

To sum up the discussion, the effects of strong property variation can either aid the turbulence or act towards reducing it. In the case where they reduce the turbulence levels, there will be a ‘heat transfer deterioration’ (HTD), due to ineffective turbulent mixing. If there is a restoration in the turbulence levels due to the structural effects of buoyancy, there will be a ‘heat transfer recovery’ (HTR).

In some cases, the effects of property variation are not strong enough to modulate the flow. Still, the variation in thermophysical properties may lead to better heat transfer characteristics. This can be predicted by equation 1-4 and is known as ‘heat transfer enhancement’ (HTE). The streamwise wall temperature profile gives an indication of the nature of the heat transfer regime.

Previous subsections 1-1-2, 1-1-3 and 1-1-4 give us a general idea of how strong property variation affects the heat transfer mechanism and turbulence in supercritical flows. For this thesis, we are interested in being able to predict the aforementioned effects well, using turbulence modeling. The following section focuses on the current progress and challenges associated with predicting such flows with CFD.

1-2 Advancements in turbulence modeling for buoyancy and thermal acceleration affected flows

As can be inferred, the mechanism of heat transfer to supercritical fluids is complicated. The presence of buoyancy effects adds another layer of complexity to the top. Most experimental investigations having the influence of buoyancy made measurements of T_w , T_b and h_c , and fitted correlations for h_c . However, to fully characterize this phenomenon, a detailed description of the velocity field, thermal field, and turbulent statistics is necessary. Also, the experimental correlations which do work well, often work only for specific cases. Thus, a numerical study of the flow and thermal fields using CFD serves as a necessary supplement to experiments [3], as it can provide detailed information about the physics. However, because of a steep variation of properties near T_{pc} , especially in turbulent flows at a comparatively high value of heat fluxes, there have not been any satisfactory computational methods in the literature [11].

The relevant literature in this field was reviewed. The experimental studies reproduced by them, along with the working fluids and turbulence models employed are listed in the appendix. Since most of these studies did not give satisfactory results, only useful insights obtained from these papers will be described in this section.

S. He et al. (2005) [12] emphasized that the use of standard $k - \epsilon$ models coupled with simple wall functions is not suitable for problems with such a strong near-wall variation of properties. They proposed that the use of Low Reynolds number models be made for this purpose. Upon carrying out a sensitivity analysis of different thermophysical properties, they found density variation to be the primary factor responsible for HTD.

S. He et al. (2008b) [13] labeled the region around T_{pc} as the Large-Property-Variation (LPV) region. It was observed that as one moves downstream, the LPV region in supercritical fluids becomes broader due to the application of heat flux, and moves away from

the wall. Alteration of turbulence is expected only when the LPV region moves out of the viscous sublayer and affects the production of TKE.

S. He et al. (2004) [14] simulated turbulent mixed convection heat transfer experiments for Supercritical CO₂ (SCO₂). They compared the performance of a few commonly used turbulence models while employing the Generalized Gradient Diffusion Hypothesis (GGDH) for modeling the buoyancy production term. The $k - \epsilon$ models used by them mainly differ in the formulation of damping functions. Following are their findings: LS [15] and AKN models overpredict the laminarization, whereas CH [16] and LB [17] models fail to predict the initial overshoot of wall temperature. Wilcox's $k-\omega$ [18], and MK [19] models predict too weak of an influence of buoyancy.

S. He et al. (2008a) [20] carried out an assessment of the performance of different turbulence models in predicting supercritical heat transfer in vertical tubes. On the basis of the nature of damping functions, they divided the models into Group 1 (LS [15], YS [21], AKN [22]; Re_t based), Group 2 (CH [16], MK [19]; y^+ based), and V2F [23] which behaves similar to Group 2. Here, Re_t and y^+ refer to turbulent Reynolds number and wall-scaled wall normal distance respectively. Group 1 damping functions respond strongly to changes in local flow conditions, and significantly overpredict flow laminarization and HTD. Group 2 damping functions respond rather weakly to local flow conditions, and perform better than group 1 models for conditions of weak buoyancy due to some canceling effects. The V2F model was found to perform the best for the given set of conditions. The use of constant turbulent Prandtl number (Pr_t) for modeling the turbulent heat fluxes was also tested. Results showed that radial turbulent heat flux could be modeled well for low buoyancy cases but not for high buoyancy cases. Axial turbulent heat flux could not be modeled well for any case using constant Pr_t . The buoyancy production of turbulence could not be reproduced for any of the models tested. Also, for the strong buoyancy case, none of the models predicted the heat transfer recovery properly.

Zhao et al. [24] analyzed the influence of various aspects of LRN $k - \epsilon$ models such as Pr_t , damping functions, and the method used to model buoyancy production on the predictions of HTD and HTR. The following observations were reported by them. GGDH is found to be superior to SGDH (simple GDH), however, in low buoyancy cases, it does not make much of a difference (due to the insignificance of the buoyancy production term). Altering the value of constant Pr_t is not expected to significantly affect the TKE levels (and thus the bigger picture). As for damping functions, it was noticed that they remain close to zero for a much greater distance from the wall than expected. As a result, some models damp the near-wall turbulence too much and predict a much higher HTD.

Pucciarelli et al. [25] investigated the use of Algebraic Heat flux models (AHFM) instead of GGDH in order to model the buoyancy production term. AHFM requires the additional solution of enthalpy variance and dissipation equations. A wide range of conditions were simulated and compared against different experimental datasets. They stated that the accurate modeling of buoyancy production term is crucial in order to predict the onset of HTR, which depends on the TKE levels. Results using AHFM were sensitive to the model constants used, however, they provided an improved estimation of buoyancy production compared to GGDH. The quality of results obtained improves slightly, however at the additional computational cost of solving two extra equations. The literature assessed presents a common consensus about the modeling of the buoyancy production term. In order to get a good prediction of the same, complex closure techniques such as AHFM are deemed necessary.

Most computational studies draw conclusions and tune their models by making comparisons with rather old experimental studies [11]. These studies are not expected to have a high level of accuracy with respect to mean or turbulent statistics in the near-critical region. The development of Reynolds Averaged Navier Stokes (RANS) models for such cases is impeded by a lack of reliable experimental data on hydraulic drag and internal flow structures, and flow statistics [26]. Thus, making accurate predictions about the flow field using Direct Numerical Simulations (DNS) is crucial to be able to make robust and accurate turbulence models.

Bae et al. (2005) [26] carried out a DNS of turbulent pipe flows with SCO2 as the fluid. They found the ratio of $\rho'_{rms}/\langle\rho\rangle$ to reach around 50-60 % near the T_{pc} region, thus invalidating Morkovin's hypothesis [8] and making the density fluctuations important. They also found that the values of streamwise and wall-normal Reynolds stress, and the axial turbulent heat flux are strongly dependent on their respective buoyancy production terms in strongly heated vertical supercritical flows. Analysis of the downward flows revealed that the buoyancy production terms always increase their respective turbulence statistics, as expected.

Nemati et al. [1] in their DNS study reported that first and second-order moments in the mean energy equation are expected to be important. Unlike for constant property cases where they are zero, here they strongly modified the average heat flux distribution at and near the wall. Further, they reported an averaging artifact called Jensen inequality. It causes an averaged thermophysical quantity (mainly c_p and λ) to significantly deviate from the value of same quantity evaluated at the averaged temperature. The difference between them increases with an increase in enthalpy fluctuations.

The following inferences can be made from the literature surveyed. The DNS studies primarily mention the observations about flow physics of strongly heated supercritical developing flows. Terms that are often negligible for constant property or subcritical flows become important for these flows. RANS studies primarily focus on testing out the conventional turbulence models for supercritical heated cases. There is no common consensus reported on the performance of different turbulence models, and sometimes contradictory findings are reported. Thus, a gap exists between DNS and RANS studies which could be bridged. It is hypothesized that if the improvements in turbulence modeling are proposed on the basis of observations in physics, we would have a better chance of building better and more robust models.

There are a few theories in the literature that isolate the leading-order effects of strong property variation on turbulence. Semi-local scaling (SLS) [27] and Apparent Reynolds Number theory (ARN) [28] are such theories related to the modulation of turbulence due to strong property variation and the streamwise body forces resulting from strong property variation, respectively. A scaling analysis that better characterizes the modulated turbulence lies at the heart of both theories. One approach to improve the turbulence model predictions could be to make use of these scaling laws. A successful attempt at doing so would give us better results without having to test new closure techniques for a wide range of flows. This study is an effort to understand and make use of these theories to improve the turbulence models within the context of this thesis topic. A brief description of both theories is provided in the following sections.

1-3 Semi Local Scaling

To proceed further, it is necessary to be familiar with the ‘Law of the wall’ for wall-bounded turbulent flows in the near wall region. There are two distinct scaling regions in wall-bounded turbulent flows, the inner and the outer region [29]. For both regions, friction velocity u_τ is taken as the velocity scale. However, the length scale for the outer region is H (depends on geometry), and for the inner region is $\delta_\nu = \nu_w/u_\tau$ (depends on wall properties). This law states that scaled velocity profile ($\bar{u}^+ = \bar{u}/u_\tau$) becomes independent of flow geometry and Reynolds number near the wall, as a function of normalized length scale $y^+ = y/\delta_\nu$. Thus, a universal collapse of the scaled velocity profile is obtained in the near-wall region.

However, this universal collapse is obtained only for the mean velocity. Turbulent statistics are a unique function of wall-normal distance and friction Reynolds number, such that $\overline{u'_i u'_j}/u_\tau^2 = f(y/h, Re_\tau)$ [27]. The function f is a generalized function, and may not be known a priori [27]. For the inner region, the expression reduces to $\overline{u'_i u'_j}/u_\tau^2 \approx f(y^+, Re_\tau)$. No universal scaling law with respect to Re_τ exists, as the statistics may or may not collapse for flows with different Re_τ .

This ‘incompressible’ version of the Law of the Wall is based on experimental observations for constant property flows and does not work for flows with strong property variation. By assuming Morkovin’s hypothesis [8] and neglecting property fluctuations, the scaling law for variable property turbulent flows can be written as $\overline{\rho u'_i u'_j}/\tau_w \approx f(y/h, Re_\tau, \bar{\rho}, \bar{\mu})$. Huang et al. [30] proposed the use of ‘semi-local scales’ (SLS) utilizing locally averaged properties for defining the characteristic scales, given by $u_\tau^* = \sqrt{\tau_w/\bar{\rho}}$ and $\delta_\nu^* = \bar{\nu}/u_\tau^*$. Also, the semi-local Re_τ and semi-local wall normal distance are given by $Re_\tau^* = h/\delta_\nu^*$ and $y^* = y/\delta_\nu^*$. This was based on heuristic arguments.

Patel et al. (2015) [27] developed a mathematical framework, to show that for variable property flows the near-wall mean and turbulent flow statistics are a unique function of y^* and Re_τ^* . Thus, they show that the leading order effect of property variation on fully developed turbulent flows can be characterized well by Re_τ^* .

The work of Patel et al. is talked about in-depth in chapter 4

1-4 Apparent Reynolds Number theory

S. He et al. (2016) [28] presented a novel viewpoint regarding laminarization in fully developed turbulent flows subjected to streamwise body forces. The effects of property variation in heated supercritical turbulent flows can be looked at as streamwise body forces. This is because they cause a near-wall acceleration/ deceleration in the flow, as explained in subsection 1-1-2. Thus, the total flow can be generalized as a body-force-influenced (BFI) flow.

Conventionally, ‘laminarization’ refers to the fact that BFI flows tend to become less turbulent compared to other undisturbed flows at the same Reynolds number. However, they showed that the BFI flow behaves similarly to an undisturbed constant property turbulent flow, which has a lower Reynolds number. This undisturbed constant property flow and its Re_τ are known as Equal Pressure Gradient (EPG) flow and Apparent Reynolds Number (ARN) respectively. The EPG flow is driven by the same pressure gradient as the BFI flow.

When a flow is strongly heated, non-uniform body forces start acting on it. In the cases where this causes a near-wall acceleration, the pressure gradient driving the total flow reduces, as explained in subsection 1-1-2. Stronger body forces lead to a larger reduction in the pressure gradient. This causes the ARN to decrease, making the flow less turbulent.

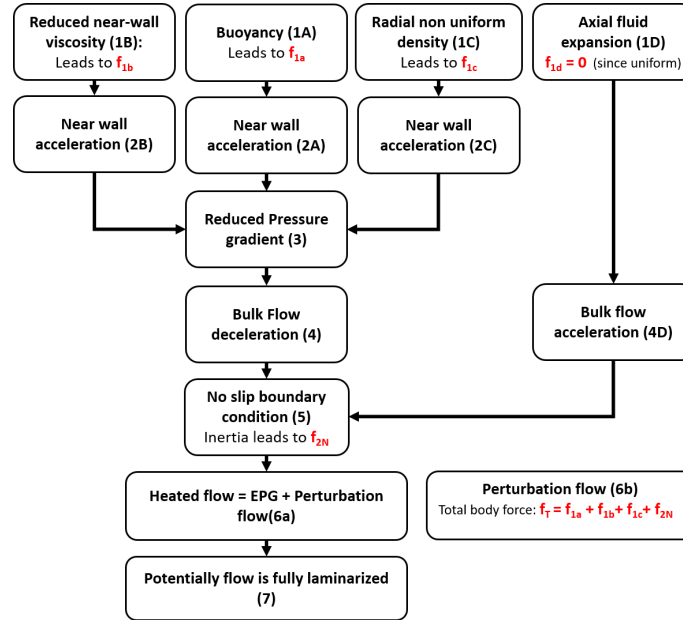


Figure 1-3: A unified explanation for flow laminarisation in heated flows [4]

The primary hypothesis of this paper states that the addition of non-uniform body forces to a flow initially driven only by a pressure gradient does not affect the turbulent mixing characteristics of the flow. It merely causes a ‘perturbation flow’ on the top of the EPG flow. Stronger body forces cause a larger perturbation flow and a lower ARN. Further, the eddy viscosity of the flow remains largely unchanged, compared to the EPG flow. They proposed that the total flow be represented as a summation of the EPG flow and a perturbation flow caused by body forces. Their hypothesis implies that:

$$\nu_{t, \text{total flow}} = \nu_{t, \text{EPG flow}} \cdot \quad (1-8)$$

S. He et al. [28] successfully tested out their hypothesis for fully developed flows subjected to artificially imposed non-linear body forces. J. He et al. [4] expanded this work, in order to account for the buoyancy force and spatial development in heated vertical supercritical flows. The effects of buoyancy and inertia cause localized acceleration/deceleration and hence can also be thought of as streamwise ‘pseudo-body forces’.

An attempt to explain the same, with the help of the theory given in this paper was made in subsection 1-1-2. The only thing that needs to be added to the explanation is the concept of non-uniform pseudo-body forces. To aid the same, a simplified version of the schematic from J. He et al. [4] has been inserted (figure 1-3).

From the figure, the effects of near-wall density variation (manifesting as buoyancy and a change in turbulent stresses), viscosity variation, and non-uniform inertia forces (important for spatially developing flows) are responsible for causing non-uniform body forces in such flows. Hence, they are modeled as pseudo-body forces. The total non-uniform pseudo body force (f_T) is obtained by summing up the individual components from 1A, 1B, 1C, and 5. As before, an increasing f_T causes an increasing perturbation flow which reduces the ARN of the EPG flow.

1-5 Research objectives, scope, and goal

From the literature survey, we know that there hasn't been considerable progress in RANS modeling of heated developing supercritical turbulent flows. This hinders the turbulence models from being able to give an accurate prediction of heat transfer deterioration/recovery in such flows. These kinds of flows are important in applications such as Supercritical Water-cooled Reactors (SCWRs) in the Nuclear Energy sector [4]. Thus, being able to predict such flows well is crucial in order to aid the energy transition process, which is the need of the hour.

Heated developing supercritical turbulent flows have a very strong variation of thermo-physical properties. This leads to the equations for momentum and energy transport being strongly coupled and complicates the physics considerably. However, most of the conventional turbulence models have originally been derived for and tuned to constant property fully developed turbulent flows. As a result, the conventional models do not give good predictions for these flows. A good understanding of the physics of these flows will take us a step closer to building better RANS models. In order to aid this, Semi-Local Scaling and Apparent Reynolds Number theory seem to be promising prospects. The former, due to its ability to account for strong property variation in turbulent flows, and the latter due to being proven to work well with flows subjected to buoyancy and spatial development. Keeping this in mind, the following research objectives have been formulated.

Research Objective 1:

To analyze the modulation of turbulence in developing heated supercritical flows. Also, to assess whether Semi-Local Scaling and Apparent Reynolds Number theories can characterize these flows well.

We have an overarching idea of how the mean flow and turbulent statistics are affected by strong heating and spatial development from the literature. However, a deeper understanding of these phenomena and the turbulence-modulating mechanisms is deemed necessary. This will also help us understand why the aforementioned theories are successful/unsuccessful in characterizing our cases. In order to fulfill this research objective, the DNS data of heated developing supercritical turbulent flows from the Ph.D. work of Dr. Hassan Nemati [1] will be analyzed. The assessment of SLS and ARN theories will also be performed on the DNS data.

Research Objective 2:

To use the inferences from the previous research objective to improve the performance of conventional RANS models for heated developing supercritical turbulent flows.

From the literature, we know that the primary drawbacks of the conventional turbulence models lie in the formulations of their damping functions and the buoyancy production term. This thesis will focus on the former issue. The unsatisfactory performance of damping functions renders the conventional models unable to give a good prediction of the near-wall eddy viscosity. We will try to use the insights obtained from the results of research objective 1 to tackle this problem. The turbulence models that have been chosen for this task are Myong-Kasagi (MK) [19], Menter's $k - \omega$ SST [31], and Spalart Allmaras (SA) [32].

Thus the **goal** of this thesis is to get a deeper understanding of turbulence modulation in

heated developing supercritical turbulent flows and use it to improve RANS turbulence models. The results and inferences will be for spatially developing supercritical turbulent flows subjected to a constant wall heat flux. However, the findings from this thesis are expected to be relevant for a wide range of spatially developing flows subjected to streamwise non-uniform body forces.

For reasons that will be discussed in chapter 4, the **scope** of this thesis is limited to laminarizing flows. These are the flows in which shear production is the dominant mechanism of turbulence generation throughout the domain. Also, in this thesis, we will only make use of eddy viscosity turbulence models.

The outline of this thesis is as follows:

- **Chapter 2** describes the governing equations relevant to the cases we have considered and the basics of turbulence modeling.
- **Chapter 3** provides an overview of the in-house RANS code that was used for this thesis.
- **Chapter 4** briefly introduces the cases that were simulated in this thesis. This is followed by a discussion on how the turbulence is modulated due to strong property variation in the chosen cases. Later, we evaluate the applicability of ARN and SLS theory for the chosen cases.
- **Chapter 5** starts off with a detailed explanation of ARN theory. Later, the methodology that can be adopted to use ARN and SLS theories for turbulence modeling is described.
- **Chapter 6** elaborates on the results obtained by implementing the methodology mentioned in the previous chapter. The results are compared with conventional and semi-locally scaled turbulence models.

Theoretical Framework

In this chapter, the instantaneous form of the governing equations for turbulent flows will be provided. Then, these equations will be statistically averaged to obtain the Reynolds Averaged Navier Stokes (RANS) equations. Finally, the commonly used closure techniques to model the additional terms in RANS equations will be discussed.

2-1 Governing equations: Instantaneous Form

In this study, DNS data from Nemati et al. [1] was utilized. These simulations have been carried out at supercritical pressure, with CO₂ as the fluid. Due to the strong heating and supercritical pressure, we have a significant variation of thermophysical properties in the domain. In such flows, the fully compressible Navier-Stokes equations are very difficult to solve numerically [26]. This is due to the severe time step restrictions resulting from the small time scales of acoustic waves. Hence the low Mach Number approximation of the Navier-Stokes equation, which ignores the acoustic waves caused by pressure fluctuations and compressibility effects was utilized by Nemati et al.[1]. This is valid, as long as the magnitude of the velocity in the domain is much lower than the speed of sound.

Thus, the pressure field can be decomposed into its thermodynamic (P_0) and hydrodynamic ($p(x, t)$) components. Consequently, all the thermo-physical properties can be determined as a function of thermodynamic pressure, independent of hydrodynamic variations (as $P_0 \gg p(x, t)$). This is synonymous with saying that the heat transfer processes in consideration are thermodynamically at a constant pressure, which is a common assumption for low-speed incompressible flows [26]. Also, viscous dissipation and gravitational work terms have been neglected in the energy equation, because their effects are very small in low-speed flows [26].

Because the simulation domain is a pipe, the governing equations have been written in cylindrical form, with z as the streamwise, θ as the circumferential, and r as the radial coordinates. The governing equations can be written in their dimensional form as given below.

Continuity equation:

$$\frac{\partial \rho}{\partial t} + \frac{1}{r} \frac{\partial r \rho u_r}{\partial r} + \frac{1}{r} \frac{\partial \rho u_\theta}{\partial \theta} + \frac{\partial \rho u_z}{\partial z} = 0. \quad (2-1)$$

Conservation of momentum in radial direction:

$$\frac{\partial \rho u_r}{\partial t} + \frac{1}{r} \frac{\partial r \rho u_r u_r}{\partial r} + \frac{1}{r} \frac{\partial \rho u_r u_\theta}{\partial \theta} + \frac{\partial \rho u_r u_z}{\partial z} - \frac{\rho u_\theta u_\theta}{r} = -\frac{\partial p}{\partial r} + \frac{1}{r} \frac{\partial r \tau_{rr}}{\partial r} + \frac{1}{r} \frac{\partial \tau_{r\theta}}{\partial \theta} - \frac{\tau_{\theta\theta}}{r} + \frac{\partial \tau_{rz}}{\partial z}. \quad (2-2)$$

Conservation of momentum in circumferential direction:

$$\frac{\partial \rho u_\theta}{\partial t} + \frac{1}{r} \frac{\partial r \rho u_\theta u_r}{\partial r} + \frac{1}{r} \frac{\partial \rho u_\theta u_\theta}{\partial \theta} + \frac{\partial \rho u_\theta u_z}{\partial z} + \frac{\rho u_\theta u_r}{r} = -\frac{1}{r} \frac{\partial p}{\partial \theta} + \frac{1}{r^2} \frac{\partial r^2 \tau_{\theta r}}{\partial r} + \frac{1}{r} \frac{\partial \tau_{\theta\theta}}{\partial \theta} + \frac{\partial \tau_{\theta z}}{\partial z}. \quad (2-3)$$

Conservation of momentum in axial direction:

$$\frac{\partial \rho u_z}{\partial t} + \frac{1}{r} \frac{\partial r \rho u_z u_r}{\partial r} + \frac{1}{r} \frac{\partial \rho u_z u_\theta}{\partial \theta} + \frac{\partial \rho u_z u_z}{\partial z} = -\frac{\partial p}{\partial z} + \frac{1}{r} \frac{\partial r \tau_{zr}}{\partial r} + \frac{1}{r} \frac{\partial \tau_{z\theta}}{\partial \theta} + \frac{\partial \tau_{zz}}{\partial z} + \rho g. \quad (2-4)$$

Conservation of energy:

$$\frac{\partial \rho h}{\partial t} + \frac{1}{r} \frac{\partial r \rho h u_r}{\partial r} + \frac{1}{r} \frac{\partial \rho h u_\theta}{\partial \theta} + \frac{\partial \rho h u_z}{\partial z} = \frac{1}{r} \frac{\partial}{\partial r} \left(r \lambda \frac{\partial T}{\partial r} \right) + \frac{1}{r} \frac{\partial}{\partial \theta} \left(\frac{\lambda}{r} \frac{\partial T}{\partial \theta} \right) + \frac{\partial}{\partial z} \left(\lambda \frac{\partial T}{\partial z} \right), \quad (2-5)$$

where the diffusion terms of the energy equation can be expressed in terms of enthalpy, with the help of the following general relation:

$$dh = \left. \frac{\partial h}{\partial T} \right|_p dT + \left. \frac{\partial h}{\partial p} \right|_T dP. \quad (2-6)$$

As discussed, the low Mach approximation lets us assume a constant thermodynamic pressure in the domain. Thus,

$$dh = \left. \frac{\partial h}{\partial T} \right|_p dT. \quad (2-7)$$

Specific heat capacity (c_p) is defined as:

$$c_p = \left. \frac{\partial h}{\partial T} \right|_p. \quad (2-8)$$

Thermal diffusivity is defined as:

$$\alpha = \frac{\lambda}{c_p}. \quad (2-9)$$

Combining equations 2-5, 2-7, 2-8, and 2-9, we get:

$$\frac{\partial \rho h}{\partial t} + \frac{1}{r} \frac{\partial r \rho h u_r}{\partial r} + \frac{1}{r} \frac{\partial \rho h u_\theta}{\partial \theta} + \frac{\partial \rho h u_z}{\partial z} = \frac{1}{r} \frac{\partial}{\partial r} \left(r \alpha \frac{\partial h}{\partial r} \right) + \frac{1}{r} \frac{\partial}{\partial \theta} \left(\frac{\alpha}{r} \frac{\partial h}{\partial \theta} \right) + \frac{\partial}{\partial z} \left(\alpha \frac{\partial h}{\partial z} \right). \quad (2-10)$$

The stress tensors from equations 2-2, 2-3, and 2-4 are given as:

$$\tau_{rr} = \mu \left(2 \frac{\partial u_r}{\partial r} - \frac{2}{3} \nabla \cdot u \right), \quad (2-11)$$

$$\tau_{\theta\theta} = \mu \left(2 \left(\frac{1}{r} \frac{\partial u_\theta}{\partial \theta} + \frac{u_r}{r} \right) - \frac{2}{3} \nabla \cdot u \right), \quad (2-12)$$

$$\tau_{zz} = \mu \left(2 \frac{\partial u_z}{\partial z} - \frac{2}{3} \nabla \cdot u \right), \quad (2-13)$$

$$\tau_{r\theta} = \tau_{\theta r} = \mu \left(r \frac{\partial}{\partial r} \left(\frac{u_\theta}{r} \right) + \frac{1}{r} \frac{\partial u_r}{\partial \theta} \right), \quad (2-14)$$

$$\tau_{rz} = \tau_{zr} = \mu \left(\frac{\partial u_z}{\partial r} + \frac{\partial u_r}{\partial z} \right), \quad (2-15)$$

$$\tau_{z\theta} = \tau_{\theta z} = \mu \left(\frac{\partial u_\theta}{\partial z} + \frac{1}{r} \frac{\partial u_z}{\partial \theta} \right), \quad (2-16)$$

where,

$$\nabla \cdot u = \frac{1}{r} \frac{\partial r u_r}{\partial r} + \frac{1}{r} \frac{\partial u_\theta}{\partial \theta} + \frac{\partial u_z}{\partial z}. \quad (2-17)$$

The state variables utilized for calculating the temperature and thermophysical properties are thermodynamic pressure (P_0) and enthalpy (h).

2-1-1 Non-dimensional form

In this thesis, the equations will be scaled with respect to the inlet (unheated) wall parameters unless mentioned otherwise. The variables will be non-dimensionalized as follows:

$$\begin{aligned} x_i^* &= \frac{x_i}{D}, \quad t^* = \frac{t}{D/u_{\tau,0}}, \quad u_i^* = \frac{u_i}{u_{\tau,0}}, \quad p^* = \frac{p}{\rho_{w,0} u_{\tau,0}^2}, \\ \rho^* &= \frac{\rho}{\rho_{w,0}}, \quad \lambda^* = \frac{\lambda}{\lambda_{w,0}}, \quad c_p^* = \frac{c_p}{c_{pw,0}}, \quad \mu^* = \frac{\mu}{\mu_{w,0}}, \\ \alpha^* &= \frac{\lambda \rho_{w,0} c_{pw,0}}{\lambda_{w,0} \rho c_p}, \quad h^* = \frac{h - h_0}{c_{pw,0} T_{w,0}}, \quad T^* = \frac{T}{T_{w,0}}, \\ Q^* &= \frac{q_w D}{\lambda_{w,0} T_{w,0}} = q^* Re_{\tau,0} Pr_{w,0}, \quad q^* = \frac{q_w}{\rho_{w,0} u_{\tau,0} c_{pw,0} T_{w,0}}, \\ Re_{\tau,0} &= \frac{\rho_{w,0} u_{\tau,0} D}{\mu_{w,0}}, \quad Pr_{w,0} = \frac{\mu_{w,0} c_{pw,0}}{\lambda_{w,0}}, \quad \beta_{w,0} = \frac{-1}{\rho_{w,0}} \left. \frac{\partial \rho}{\partial T} \right|_{w,0}, \\ \frac{1}{Fr_{\tau,0}} &= \frac{gD}{u_{\tau,0}^2} = \frac{Gr_0}{\beta_{w,0} T_{w,0} Re_{\tau,0}^2 Q^*}, \quad Gr_0 = \frac{\rho_{w,0}^2 g \beta_{w,0} q_w D^4}{\mu_{w,0}^2 \lambda_{w,0}}. \end{aligned}$$

Here, the superscript ‘*’ refers to non-dimensional, the subscripts ‘0’ and ‘w’ refer to inlet and wall, $u_{\tau,0}$ is the friction velocity at the inlet, q_w is the wall heat flux (constant for cases investigated), $Re_{\tau,0}$ is the inlet friction Reynolds number, $Pr_{w,0}$ is the inlet wall Prandtl Number, $Fr_{\tau,0}$ is the inlet wall Froude Number, Gr_0 is the inlet Grashof Number, $\beta_{w,0}$ is the inlet wall volume expansivity, and D is the pipe diameter.

Upon substituting the non-dimensional variables into the governing equations 2-2, 2-3, 2-4, and 2-10, we get the equations given below. Also, even though the equations are non-dimensional, the ‘*’ superscript has not been included for brevity.

Continuity equation:

$$\frac{\partial \rho}{\partial t} + \frac{1}{r} \frac{\partial r \rho u_r}{\partial r} + \frac{1}{r} \frac{\partial \rho u_\theta}{\partial \theta} + \frac{\partial \rho u_z}{\partial z} = 0. \quad (2-18)$$

Conservation of momentum in radial direction:

$$\frac{\partial \rho u_r}{\partial t} + \frac{1}{r} \frac{\partial r \rho u_r u_r}{\partial r} + \frac{1}{r} \frac{\partial \rho u_r u_\theta}{\partial \theta} + \frac{\partial \rho u_r u_z}{\partial z} - \frac{\rho u_\theta u_\theta}{r} = -\frac{\partial p}{\partial r} + \frac{1}{r} \frac{\partial r \tau_{rr}}{\partial r} + \frac{1}{r} \frac{\partial \tau_{r\theta}}{\partial \theta} - \frac{\tau_{\theta\theta}}{r} + \frac{\partial \tau_{rz}}{\partial z}. \quad (2-19)$$

Conservation of momentum in circumferential direction:

$$\frac{\partial \rho u_\theta}{\partial t} + \frac{1}{r} \frac{\partial r \rho u_\theta u_r}{\partial r} + \frac{1}{r} \frac{\partial \rho u_\theta u_\theta}{\partial \theta} + \frac{\partial \rho u_\theta u_z}{\partial z} + \frac{\rho u_\theta u_r}{r} = -\frac{1}{r} \frac{\partial p}{\partial \theta} + \frac{1}{r^2} \frac{\partial r^2 \tau_{\theta r}}{\partial r} + \frac{1}{r} \frac{\partial \tau_{\theta\theta}}{\partial \theta} + \frac{\partial \tau_{\theta z}}{\partial z}. \quad (2-20)$$

Conservation of momentum in axial direction:

$$\frac{\partial \rho u_z}{\partial t} + \frac{1}{r} \frac{\partial r \rho u_z u_r}{\partial r} + \frac{1}{r} \frac{\partial \rho u_z u_\theta}{\partial \theta} + \frac{\partial \rho u_z u_z}{\partial z} = -\frac{\partial p}{\partial z} + \frac{1}{r} \frac{\partial r \tau_{zr}}{\partial r} + \frac{1}{r} \frac{\partial \tau_{z\theta}}{\partial \theta} + \frac{\partial \tau_{zz}}{\partial z} + \frac{1}{Fr_{\tau,0}} \rho. \quad (2-21)$$

Conservation of energy:

$$\frac{\partial \rho h}{\partial t} + \frac{1}{r} \frac{\partial r \rho h u_r}{\partial r} + \frac{1}{r} \frac{\partial \rho h u_\theta}{\partial \theta} + \frac{\partial \rho h u_z}{\partial z} = \frac{1}{Re_{\tau,0} Pr_{w,0}} \left(\frac{1}{r} \frac{\partial}{\partial r} \left(r \alpha \frac{\partial h}{\partial r} \right) + \frac{1}{r} \frac{\partial}{\partial \theta} \left(\frac{\alpha}{r} \frac{\partial h}{\partial \theta} \right) + \frac{\partial}{\partial z} \left(\alpha \frac{\partial h}{\partial z} \right) \right). \quad (2-22)$$

The stress tensors in non-dimensional momentum equations 2-19, 2-20, and 2-21 are given as:

$$\tau_{rr} = \frac{\mu}{Re_{\tau,0}} \left(2 \frac{\partial u_r}{\partial r} - \frac{2}{3} \nabla \cdot u \right), \quad (2-23)$$

$$\tau_{\theta\theta} = \frac{\mu}{Re_{\tau,0}} \left(2 \left(\frac{1}{r} \frac{\partial u_\theta}{\partial \theta} + \frac{u_r}{r} \right) - \frac{2}{3} \nabla \cdot u \right), \quad (2-24)$$

$$\tau_{zz} = \frac{\mu}{Re_{\tau,0}} \left(2 \frac{\partial u_z}{\partial z} - \frac{2}{3} \nabla \cdot u \right), \quad (2-25)$$

$$\tau_{r\theta} = \tau_{\theta r} = \frac{\mu}{Re_{\tau,0}} \left(r \frac{\partial}{\partial r} \left(\frac{u_\theta}{r} \right) + \frac{1}{r} \frac{\partial u_r}{\partial \theta} \right), \quad (2-26)$$

$$\tau_{rz} = \tau_{zr} = \frac{\mu}{Re_{\tau,0}} \left(\frac{\partial u_z}{\partial r} + \frac{\partial u_r}{\partial z} \right), \quad (2-27)$$

$$\tau_{z\theta} = \tau_{\theta z} = \frac{\mu}{Re_{\tau,0}} \left(\frac{\partial u_\theta}{\partial z} + \frac{1}{r} \frac{\partial u_z}{\partial \theta} \right), \quad (2-28)$$

where,

$$\nabla \cdot u = \frac{1}{r} \frac{\partial r u_r}{\partial r} + \frac{1}{r} \frac{\partial u_\theta}{\partial \theta} + \frac{\partial u_z}{\partial z}. \quad (2-29)$$

Froude number ($Fr_{\tau,0}$) from streamwise momentum equation 2-21 which is a function of Gr_0 , $Re_{\tau,0}$, Q^* , and the unheated reference condition, is representative of the buoyancy effect [7]. For a given $Re_{\tau,0}$, Q^* , and the inlet reference condition, one can vary D , and thus the Gr_0 to adjust the strength of buoyancy effects [7]. In equation 2-21, if the flow is in the direction of gravity (downward), it takes a positive sign, and vice versa for flow against gravity.

The equations provided in this section are solved for DNS, where all the scales of the flow need to be resolved. Thus, a very fine mesh is needed even at relatively moderate Reynolds numbers, making DNS computationally very expensive. In applications where a high level of detail is not required, the statistically averaged form of these equations is solved. The same will be discussed below.

2-2 Governing equations: Reynolds Averaged Navier - Stokes (RANS)

For the cases under consideration, the simulation geometry is a pipe and is heated symmetrically. The resulting turbulent flow is statistically homogenous in the circumferential direction. Thus, the equations presented in the previous section are statistically averaged over time, and over the circumferential direction, to obtain RANS equations. Two different types of averaging could be applied, which will be discussed below.

Reynolds Averaging

When Reynolds averaging is applied to a variable γ , it can be decomposed into a mean component $\bar{\gamma}$, and a fluctuating component γ' . Thus,

$$\gamma = \bar{\gamma} + \gamma', \quad (2-30)$$

where,

$$\bar{\gamma} = \frac{1}{N_t N_\theta} \sum_1^{N_t} \sum_1^{N_\theta} \gamma. \quad (2-31)$$

N_θ and N_t are the number of samples taken in circumferential direction and time respectively.

Also,

$$\overline{\gamma'} = 0, \quad (2-32)$$

Favre Averaging

For variable density flows, it is common to use density-weighted averaging, to account for strong density fluctuations. This enables us to keep a relatively simple form of equations, similar to conventional RANS equations. Under Favre averaging, a variable γ can be decomposed into a density-weighted mean component $\tilde{\gamma}$ and fluctuating component γ'' . Thus,

$$\gamma = \tilde{\gamma} + \gamma'', \quad (2-33)$$

where,

$$\tilde{\gamma} = \frac{\overline{\rho\gamma}}{\bar{\rho}}. \quad (2-34)$$

Also,

$$\overline{\gamma''} \neq 0. \quad (2-35)$$

However,

$$\overline{\rho\gamma''} = 0. \quad (2-36)$$

The goal when simultaneously utilizing both Favre and Reynolds averaging methods is to obtain a relatively simple form of governing equations, with fewer terms. To enable the same, the velocity and enthalpy are Favre averaged, whereas the pressure and thermo-physical properties are Reynolds averaged. Even though both methods will be utilized, the governing equations will still be called Reynolds Averaged Navier-Stokes equations.

For a circumferentially homogenous turbulent flow, the governing equations become two-dimensional, and the following assumptions hold:

$$\tilde{u}_\theta = 0, \quad (2-37)$$

$$\overline{\frac{\partial}{\partial \theta}} = 0. \quad (2-38)$$

Upon using Reynolds and Favre averaging, the variables can be decomposed as follows:

$$\rho = \bar{\rho} + \rho', \quad p = \bar{p} + p', \quad \mu = \bar{\mu} + \mu', \quad \alpha = \bar{\alpha} + \alpha', \quad u_i = \tilde{u}_i + u''_i, \quad h = \tilde{h} + h''. \quad (2-39)$$

By substituting equation 2-39 into the governing equations 2-19-2-29, applying Reynolds averaging and simplifying the equations using 2-32, 2-36, 2-37, and 2-38, RANS equations can be obtained as given below.

Continuity equation:

$$\frac{\partial \bar{\rho}}{\partial t} + \frac{1}{r} \frac{\partial r \bar{\rho} \tilde{u}_r}{\partial r} + \frac{\partial \bar{\rho} \tilde{u}_z}{\partial z} = 0. \quad (2-40)$$

Conservation of momentum in radial direction:

$$\frac{\partial \bar{\rho} \tilde{u}_r}{\partial t} + \frac{1}{r} \frac{\partial r \bar{\rho} \tilde{u}_r \tilde{u}_r}{\partial r} + \frac{\partial \bar{\rho} \tilde{u}_r \tilde{u}_z}{\partial z} = -\frac{\partial \bar{p}}{\partial r} + \frac{1}{r} \frac{\partial r \bar{\tau}_{rr}}{\partial r} - \frac{\bar{\tau}_{\theta\theta}}{r} + \frac{\partial \bar{\tau}_{rz}}{\partial z} - \frac{1}{r} \frac{\partial r \overline{\rho u''_r u''_r}}{\partial r} - \frac{\partial \overline{\rho u''_r u''_z}}{\partial z} + \frac{\overline{\rho u''_\theta u''_\theta}}{r} \quad (2-41)$$

Conservation of momentum in axial direction:

$$\frac{\partial \bar{\rho} \tilde{u}_z}{\partial t} + \frac{1}{r} \frac{\partial r \bar{\rho} \tilde{u}_z \tilde{u}_r}{\partial r} + \frac{\partial \bar{\rho} \tilde{u}_z \tilde{u}_z}{\partial z} = -\frac{\partial \bar{p}}{\partial z} + \frac{1}{r} \frac{\partial r \bar{\tau}_{zr}}{\partial r} + \frac{\partial \bar{\tau}_{zz}}{\partial z} + \frac{\bar{p}}{Fr_{\tau,0}} - \frac{1}{r} \frac{\partial r \overline{\rho u''_z u''_r}}{\partial r} - \frac{\partial \overline{\rho u''_z u''_z}}{\partial z}. \quad (2-42)$$

Conservation of energy:

$$\begin{aligned} \frac{\partial \bar{\rho} \tilde{h}}{\partial t} + \frac{1}{r} \frac{\partial r \bar{\rho} \tilde{h} \tilde{u}_r}{\partial r} + \frac{\partial \bar{\rho} \tilde{h} \tilde{u}_z}{\partial z} &= \frac{1}{Re_{\tau,0} Pr_{w,0}} \left(\frac{1}{r} \frac{\partial}{\partial r} \left(r \bar{\alpha} \frac{\partial \tilde{h}}{\partial r} \right) + \frac{\partial}{\partial z} \left(\bar{\alpha} \frac{\partial \tilde{h}}{\partial z} \right) + \frac{1}{r} \frac{\partial}{\partial r} \left(r \bar{\alpha} \frac{\partial \tilde{h}''}{\partial r} \right) \right. \\ &\quad \left. + \frac{\partial}{\partial z} \left(\bar{\alpha} \frac{\partial \tilde{h}''}{\partial z} \right) + \frac{1}{r} \frac{\partial}{\partial r} \left(r \alpha' \frac{\partial \tilde{h}''}{\partial r} \right) + \frac{\partial}{\partial z} \left(\alpha' \frac{\partial \tilde{h}''}{\partial z} \right) \right) - \frac{1}{r} \frac{\partial r \overline{\rho h'' u''_r}}{\partial r} - \frac{\partial \overline{\rho h'' u''_z}}{\partial z}. \end{aligned} \quad (2-43)$$

The stress tensors in equations 2-41 and 2-42 are given as:

$$\bar{\tau}_{rr} = \frac{2}{Re_{\tau,0}} \left(\bar{\mu} \frac{\partial \tilde{u}_r}{\partial r} + \overline{\mu' \frac{\partial u''_r}{\partial r}} + \bar{\mu} \frac{\partial \overline{u''_r}}{\partial r} - \frac{1}{3} \bar{\mu} \nabla \cdot \tilde{u} - \frac{1}{3} \bar{\mu} \nabla \cdot \overline{u''} - \frac{1}{3} \overline{\mu' \nabla \cdot u''} \right), \quad (2-44)$$

$$\bar{\tau}_{\theta\theta} = \frac{2}{Re_{\tau,0}} \left(\bar{\mu} \frac{\tilde{u}_r}{r} + \bar{\mu} \frac{\overline{u''_r}}{r} + \mu' \frac{\overline{u''_r}}{r} - \frac{1}{3} \bar{\mu} \nabla \cdot \tilde{u} - \frac{1}{3} \bar{\mu} \nabla \cdot \overline{u''} - \frac{1}{3} \overline{\mu' \nabla \cdot u''} \right), \quad (2-45)$$

$$\bar{\tau}_{zz} = \frac{2}{Re_{\tau,0}} \left(\bar{\mu} \frac{\partial \tilde{u}_z}{\partial z} + \overline{\mu' \frac{\partial u''_z}{\partial z}} + \bar{\mu} \frac{\partial \overline{u''_z}}{\partial z} - \frac{1}{3} \bar{\mu} \nabla \cdot \tilde{u} - \frac{1}{3} \bar{\mu} \nabla \cdot \overline{u''} - \frac{1}{3} \overline{\mu' \nabla \cdot u''} \right), \quad (2-46)$$

$$\bar{\tau}_{rz} = \bar{\tau}_{zr} = \frac{1}{Re_{\tau,0}} \left(\bar{\mu} \frac{\partial \tilde{u}_z}{\partial r} + \overline{\mu' \frac{\partial u''_z}{\partial r}} + \bar{\mu} \frac{\partial \overline{u''_z}}{\partial r} + \bar{\mu} \frac{\partial \tilde{u}_r}{\partial z} + \overline{\mu' \frac{\partial u''_r}{\partial z}} + \bar{\mu} \frac{\partial \overline{u''_r}}{\partial z} \right), \quad (2-47)$$

where,

$$\nabla \cdot \tilde{u} = \frac{1}{r} \frac{\partial r \tilde{u}_r}{\partial r} + \frac{\partial \tilde{u}_z}{\partial z}, \quad (2-48)$$

$$\nabla \cdot u'' = \frac{1}{r} \frac{\partial r u_r''}{\partial r} + \frac{\partial u_z''}{\partial z}. \quad (2-49)$$

As mentioned, the point of using a combination of Reynolds and Favre averaging is to keep the number of terms to a minimum. Also, the primary purpose of using the Favre average is to include the effect of strong density fluctuations in averaged velocity and enthalpy. However, as the turbulent statistics of the diffusion terms do not inherently have density in them, it is common to report them in the form of Reynolds averaged velocity and enthalpy as follows:

$$u_i = \bar{u}_i + u_i', \quad h = \bar{h} + h' \quad (2-50)$$

This works towards reducing the number of terms, as $\bar{\gamma}' = 0$, but, $\bar{\gamma}'' \neq 0$.

However, the RANS governing equations 2-41-2-49 are solved for \tilde{u}_i , and \tilde{h} . Decomposing the diffusion terms as equation 2-50 leads to additional unknowns, namely \bar{u}_i and \bar{h} . Thus, it is not appropriate to apply Reynolds decomposition in the diffusion term, from a RANS modeling perspective [7].

2-3 Turbulence Modeling

The emergence of additional terms can be seen in equations 2-41, 2-42, and 2-43, due to the application of the averaging procedure to the non-linear advection terms. We end up having more variables than equations and thus need closure equations for the same. Turbulence models are employed in order to model and thus get a good approximation of the extra terms. A brief overview of commonly used modeling techniques is given below.

Turbulence models can broadly be categorized as follows:

Eddy viscosity models

The eddy viscosity/ Boussinesq closure hypothesis involves treating the turbulent stress tensor in an analogous way to the viscous stress tensor. Thus, the terms of the turbulent stress tensor are expressed using the strain rate tensor, and a proportionality constant. The proportionality constant in question is nothing but the turbulent/ eddy viscosity μ_t . Thus, the Reynolds stresses can be expressed as:

$$\overline{\rho u_r'' u_r''} = -\mu_t \left(2 \frac{\partial \tilde{u}_r}{\partial r} - \frac{2}{3} \nabla \cdot \tilde{u} \right) + \frac{2}{3} \bar{\rho} \tilde{k}, \quad (2-51)$$

$$\overline{\rho u_\theta'' u_\theta''} = -\mu_t \left(2 \frac{\tilde{u}_r}{r} - \frac{2}{3} \nabla \cdot \tilde{u} \right) + \frac{2}{3} \bar{\rho} \tilde{k}, \quad (2-52)$$

$$\overline{\rho u_z'' u_z''} = -\mu_t \left(2 \frac{\partial \tilde{u}_z}{\partial z} - \frac{2}{3} \nabla \cdot \tilde{u} \right) + \frac{2}{3} \bar{\rho} \tilde{k}, \quad (2-53)$$

$$\overline{\rho u_r'' u_z''} = -\mu_t \left(\frac{\partial \tilde{u}_r}{\partial z} + \frac{\partial \tilde{u}_z}{\partial r} \right), \quad (2-54)$$

where \tilde{k} (turbulent kinetic energy) is given by:

$$\tilde{k} = \frac{1}{2\bar{\rho}} (\overline{\rho u_r'' u_r''} + \overline{\rho u_\theta'' u_\theta''} + \overline{\rho u_z'' u_z''}) \quad (2-55)$$

Different methods can be employed in order to calculate the value of μ_t . The methods can be classified on the basis of the number of equations they solve as given below.

- **Zero equation/ Algebraic models:** These models calculate μ_t using Algebraic relations (revolving around Prandtl's mixing length hypothesis) and local flow quantities. Thus, they do not solve any differential equations. They work well for simple flows, however, in complex turbulent flows with effects such as flow separation/ non-ideal fluid behavior, they do not give an accurate description of turbulence physics.
- **One equation models:** In order to calculate μ_t , these models solve one transport equation. They are usually able to give a more accurate description of the turbulent flow field than the zero equation models for complex flow scenarios.
- **Two equation models:** Two equation models, namely of the classes $k - \epsilon$ and $k - \omega$ have gained a lot of popularity in engineering applications. As the name suggests, these models solve the transport equations for TKE and the dissipation of the TKE (which could either be ϵ or $\omega = \epsilon/k$). The characteristic turbulent scales required for computing the eddy viscosity are thus calculated from k and ϵ or ω .

The $k - \epsilon$ class of models can further be categorized into low and high Reynolds Number (LRN and HRN) models. In HRN models, the first computational point lies in the log-law region, and a fine mesh is not required near the wall. The region between the wall and the first mesh cell is characterized using empirical 'wall functions'. This makes the computational load low, and the code more stable. However, it is only valid for simple flows with a very high Re, and a very thin near-wall region. In LRN models, the first computational point lies in the viscous sublayer, and thus a fine mesh is required near the wall. Also, damping functions are employed in LRN models, to get an accurate description of near-wall behavior, and equations are integrated up to the wall. They can overcome the shortcomings of HRN models.

$k - \omega$ model has superior performance near the wall and does not require the use of damping functions. However, it is sensitive to the inlet free-stream properties. To overcome this, the $k - \omega$ SST model switches from $k - \omega$ to $k - \epsilon$ behavior in the free stream.

- **$v^2 - f$ model :** This model, in addition to k and ϵ , solves transport equations for two additional quantities. They are v^2 , which can be interpreted as the velocity fluctuation normal to the streamlines, and f which is an elliptic relaxation function. The strength of this model lies in the fact that it does not employ damping functions for predicting near-wall behavior. Thus, the turbulence damping due to wall blocking and pressure effects is predicted by the solution of the mentioned equations. μ_t is then calculated as a function of v^2 .

Reynolds stress models

This approach involves solving transport equations for Reynolds stresses along with a transport equation for dissipation rate ϵ . Modeling assumptions are necessary in order to solve the closure problem. Thus, the eddy viscosity approach is avoided, and the terms of Reynolds stress tensor are computed directly. This approach provides an advantage in scenarios where the eddy viscosity hypothesis is invalid, such as flows with a high degree of anisotropy.

The scope of this thesis study has been limited to eddy viscosity turbulence models. Namely, an LRN $k - \epsilon$ model Myong-Kasagi (MK) [19], a one equation model Spalart-Allmaras (SA) [32], and Menter's $k - \omega$ SST model [31] were used.

The extra terms in the energy equation (turbulent heat flux) also need closure. The same will be discussed below.

Turbulent Heat Flux models

The transport of a scalar (enthalpy in this case) by turbulence can be modeled in a similar way to the eddy viscosity hypothesis. This is accomplished using the gradient-diffusion hypothesis. The diffusion coefficient utilized in modeling turbulent heat flux is known as ‘eddy diffusivity’ (α_t). Thus, the turbulent heat fluxes can be written as:

$$\overline{\rho u_z'' h''} = \bar{\rho} \alpha_t \frac{\partial \tilde{h}}{\partial z}, \quad (2-56)$$

$$\overline{\rho u_r'' h''} = \bar{\rho} \alpha_t \frac{\partial \tilde{h}}{\partial r}. \quad (2-57)$$

A commonly used technique to model α_t is using a constant turbulent Prandtl number (Pr_t), such that:

$$\alpha_t = \frac{\mu_t}{\bar{\rho} Pr_t} \quad (2-58)$$

However, this approach assumes a high level of similarity between turbulent momentum and scalar transport. This might not be valid for complex flow scenarios where a high level of similarity can not be assumed.

Another method utilized in order to model α_t is to solve transport equations for enthalpy variance (k_θ), and its dissipation (ϵ_θ). The characteristic scales needed in order to compute α_t can be obtained using a combination of quantities such as k , ϵ , k_θ , and ϵ_θ . However, the focus of this thesis is not on improving the thermal turbulence model. We will assess how far can the turbulence model predictions be improved using a constant Pr_t . In the future, this work can be extended to more complicated thermal turbulence models.

An idea of the different closure techniques for the additional turbulent quantities can be obtained from the description provided in this section. Upon using them, the modeled RANS governing equations can be obtained, which are inserted in the following subsection.

2-3-1 Modeled RANS governing equations

Conservation of momentum in radial direction:

$$\begin{aligned} \frac{\partial \bar{\rho} \tilde{u}_r}{\partial t} + \frac{1}{r} \frac{\partial r \bar{\rho} \tilde{u}_r \tilde{u}_r}{\partial r} + \frac{\partial \bar{\rho} \tilde{u}_r \tilde{u}_z}{\partial z} = \frac{2}{r} \frac{\partial}{\partial r} \left(r \left(\frac{\bar{\mu}}{Re_{\tau,0}} + \mu_t \right) \frac{\partial \tilde{u}_r}{\partial r} \right) + \frac{\partial}{\partial z} \left(\left(\frac{\bar{\mu}}{Re_{\tau,0}} + \mu_t \right) \left(\frac{\partial \tilde{u}_z}{\partial r} + \frac{\partial \tilde{u}_r}{\partial z} \right) \right) \\ - \frac{2}{3} \frac{1}{r} \frac{\partial}{\partial r} \left(r \left(\frac{\bar{\mu}}{Re_{\tau,0}} + \mu_t \right) \nabla \cdot \tilde{u} \right) - 2 \left(\frac{\bar{\mu}}{Re_{\tau,0}} + \mu_t \right) \frac{\tilde{u}_r}{r^2} + \frac{2}{3} \left(\frac{\bar{\mu}}{Re_{\tau,0}} + \mu_t \right) \nabla \cdot \tilde{u} - \frac{\partial \bar{p}_m}{\partial r}, \end{aligned} \quad (2-59)$$

where $\bar{p}_m = \bar{p} + 2\bar{\rho}k/3$.

Conservation of momentum in axial direction:

$$\begin{aligned} \frac{\partial \bar{\rho} \tilde{u}_z}{\partial t} + \frac{1}{r} \frac{\partial r \bar{\rho} \tilde{u}_z \tilde{u}_r}{\partial r} + \frac{\partial \bar{\rho} \tilde{u}_z \tilde{u}_z}{\partial z} = 2 \frac{\partial}{\partial z} \left(\left(\frac{\bar{\mu}}{Re_{\tau,0}} + \mu_t \right) \frac{\partial \tilde{u}_z}{\partial z} \right) \\ + \frac{1}{r} \frac{\partial}{\partial r} \left(r \left(\frac{\bar{\mu}}{Re_{\tau,0}} + \mu_t \right) \left(\frac{\partial \tilde{u}_z}{\partial r} + \frac{\partial \tilde{u}_r}{\partial z} \right) \right) + \frac{\bar{\rho}}{Fr_{\tau,0}} - \frac{2}{3} \frac{\partial}{\partial z} \left(\frac{\bar{\mu}}{Re_{\tau,0}} + \mu_t \right) \nabla \cdot \tilde{u} - \frac{\partial \bar{p}_m}{\partial z}. \end{aligned} \quad (2-60)$$

Conservation of energy:

$$\frac{\partial \bar{\rho} \tilde{h}}{\partial t} + \frac{1}{r} \frac{\partial r \bar{\rho} \tilde{h} \tilde{u}_r}{\partial r} + \frac{\partial \bar{\rho} \tilde{h} \tilde{u}_z}{\partial z} = \frac{1}{r} \frac{\partial}{\partial r} \left(r \left(\frac{\bar{\alpha}}{Re_{\tau,0} Pr_{w,0}} + \frac{\mu_t}{Pr_t} \right) \frac{\partial \tilde{h}}{\partial r} \right) + \frac{\partial}{\partial z} \left(\left(\frac{\bar{\alpha}}{Re_{\tau,0} Pr_{w,0}} + \frac{\mu_t}{Pr_t} \right) \frac{\partial \tilde{h}}{\partial z} \right). \quad (2-61)$$

In order to model μ_t , Turbulent Kinetic Energy (TKE) is a very commonly used quantity. Its transport equation along with common modeling assumptions are provided in the following subsection.

2-3-2 Turbulent Kinetic Energy

The exact TKE equation can be obtained by summing up Reynolds stress transport equations and dividing both sides by 2. The Reynolds stress equations in turn need to be derived from fully compressible Navier-Stokes equations. From Bae et al. [26], the equation can be written as:

$$\frac{\partial \bar{\rho} \tilde{k}}{\partial t} + \frac{\partial \tilde{u}_j \bar{\rho} \tilde{k}}{\partial x_j} = -\overline{\rho u_i'' u_j''} \frac{\partial \tilde{u}_i}{\partial x_j} - \overline{\tau_{ij}''} \frac{\partial u_i''}{\partial x_j} - \overline{u_i''} \frac{\partial \bar{p}}{\partial x_i} + \overline{u_i''} \frac{\partial \tilde{\tau}_{ij}}{\partial x_j} + \overline{p'} \frac{\partial u_i''}{\partial x_i} + \frac{\partial}{\partial x_j} \left(\overline{u_i'' \tau_{ij}''} - \frac{\overline{\rho u_j'' u_i'' u_i''}}{2} - \overline{p' u_j''} \right), \quad (2-62)$$

$$\tilde{\tau}_{ij} = (\bar{\mu} + \mu') \left(\frac{\partial \tilde{u}_i}{\partial x_j} + \frac{\partial \tilde{u}_j}{\partial x_i} \right), \quad \tau_{ij}'' = (\bar{\mu} + \mu') \left(\frac{\partial u_i''}{\partial x_j} + \frac{\partial u_j''}{\partial x_i} \right),$$

where Favre decomposition has been applied to the stress tensor τ_{ij} , and Einstein notation has been utilized to keep the equation concise.

The buoyancy production term can be obtained by summing up the third and fourth terms in equation 2-62 and simplifying. The procedure mentioned in [7] will be followed for the same. For the cylindrical coordinate system, we get:

$$-\overline{u_z''} \left(\frac{\partial \bar{p}}{\partial z} - \frac{\partial \tilde{\tau}_{rz}}{\partial r} \right) \approx -\frac{\bar{\rho}}{Fr_{\tau,0}} \cdot \overline{u_z''},$$

$$-\overline{u_z''} \left(\frac{\partial \bar{p}}{\partial z} - \frac{\partial \tilde{\tau}_{rz}}{\partial r} \right) \approx -\frac{\overline{\rho' u_z'}}{Fr_{\tau,0}},$$

where,

$$\overline{u_z''} = -\frac{\overline{\rho' u_z'}}{\bar{\rho}}.$$

Thus, the exact equation for TKE can be written as:

$$\frac{\partial \bar{\rho} \tilde{k}}{\partial t} + \underbrace{\frac{\partial \tilde{u}_j \bar{\rho} \tilde{k}}{\partial x_j}}_C = -\underbrace{\frac{\overline{\rho' u_z'}}{Fr_{\tau,0}}}_{G_k} - \underbrace{\overline{\rho u_i'' u_j''} \frac{\partial \tilde{u}_i}{\partial x_j}}_{P_k} - \underbrace{\overline{\tau_{ij}''} \frac{\partial u_i''}{\partial x_j}}_{DS} + \underbrace{\overline{p'} \frac{\partial u_i''}{\partial x_i}}_{\pi} + \underbrace{\frac{\partial}{\partial x_j} \left(\overline{u_i'' \tau_{ij}''} - \frac{\overline{\rho u_j'' u_i'' u_i''}}{2} - \overline{p' u_j''} \right)}_{DF}, \quad (2-63)$$

where, the terms are (left to right) Temporal derivative, Convection, Buoyancy Production, Shear Production, Dissipation, Pressure-Dilatation, and Transport terms.

From equation 2-63, terms on the right-hand side need to be modeled. For eddy viscosity models, P_k is modeled using the eddy viscosity hypothesis. DS is modeled by solving its own transport equation. π will be neglected, as its magnitude is not expected to be comparable to the other terms. DF will be modeled using the Gradient Diffusion Hypothesis (GDH). In order to model G_k , it will be simplified as follows:

$$G_k \approx \frac{\overline{\rho' u_z'}}{Fr_{\tau,0}} \approx -\frac{\overline{\beta \rho T' u_z'}}{Fr_{\tau,0}}, \quad \beta = -\frac{1}{\rho} \frac{\partial \rho}{\partial T}. \quad (2-64)$$

Now, $\overline{\rho T' u_z'}$ from G_k can be modeled using simple or generalized GDH. Generalized GDH (GGDH) from [33] is a more sophisticated approach, as it accounts for anisotropy in turbulent diffusivity. Using GGDH, we get:

$$G_k \approx \frac{1}{Fr_{\tau,0}} \beta C_T T_\tau \left(\overline{\rho u_r'' u_z''} \frac{\partial \tilde{T}}{\partial r} + \overline{\rho u_z'' u_z''} \frac{\partial \tilde{T}}{\partial z} \right), \quad (2-65)$$

where, $C_T = 0.3$ is a modeling constant, and T_τ is the turbulent time scale. T_τ can be obtained as $\tilde{k}/\tilde{\epsilon}$ or $1/\tilde{\omega}$, depending on the models used. Also, since the SA model solves a transport equation for an unconventional variable, the derivation of its buoyancy production is not straightforward. Hence, a buoyancy production term will not be considered for the same.

Thus, we have an idea of the necessary assumptions and simplifications required for turbulence modeling. The transport equations for the turbulence models used in this thesis are provided in the appendix, along with the modeling constants and functions.

Also, a short introduction to semi-local scaling was provided in the section 1-3. In a nutshell, it states that the leading order effect of property variation in fully developed wall-bounded turbulent flows can effectively be captured by semi-local Reynolds number. Pecnik et al. [34] reported that if turbulence models are solved in their SLS form, much better results are obtained compared to their conventionally scaled counterparts. Otero et al. [35] rescaled SLS equations derived by Pecnik et al. [34] to conventional scales. Upon doing so, they reported that only the diffusion term takes a different form as compared to conventional models. Thus, they claimed that modifying the diffusion term in conventional turbulent transport equations is the same as solving SLS transport equations. We will make use of SLS transport equations in the form proposed by Otero et al. [35] in this thesis. The modified diffusion terms for the chosen models are also provided in the appendix.

Numerical set-up

An in-house FORTRAN RANS code [36] has been used in order to carry out the simulations for this thesis. A description of the simulation domain and the numerics of the code will be provided in this chapter.

3-1 Simulation domain

The flows this thesis focuses on have a fully developed unheated turbulent flow at the inlet. They are then heated at the wall with constant heat flux and allowed to evolve. In order to accomplish this, the RANS simulation is split up into two parts.

The first part is called the inflow generator, which is a constant property fully developed turbulent pipe flow. The length of the inflow generator was set equal to $5D$, where D is the diameter of the pipe.

The second part is a developing pipe flow. The length of the domain depends on the case being simulated. For our cases, the length was set to $30D$. The schematic of the computational domain is inserted below.

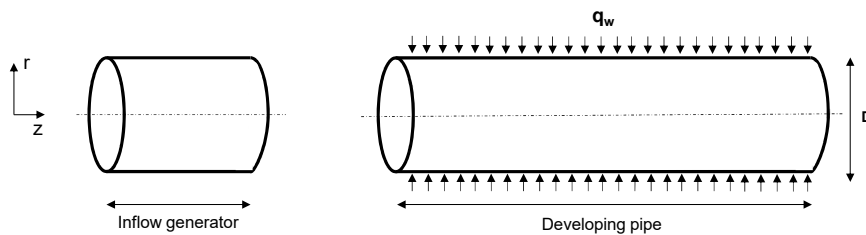


Figure 3-1: Computational domain for the RANS simulations

The numerical domain is thus an axisymmetric pipe. It uses a constant grid spacing in the streamwise direction. The mesh distribution in the wall-normal direction is non-uniform and achieved with the use of a hyperbolic tangent function. It takes the following form:

$$\frac{r(i)}{R} = \frac{\left(1 - \frac{\tanh(f_b(f_a - \frac{i}{imax}))}{\tanh(f_a f_b)}\right)}{\left(1 - \frac{\tanh(f_b(f_a - 1))}{\tanh(f_a f_b)}\right)}, \quad (3-1)$$

where, $f_a = 0.12$, $f_b = 2.4$, $R = 0.5$, and $imax$ is the number of wall-normal discretization points.

3-2 Numerical method

A staggered grid is used by this code. Thus, all the scalar equations and the scalars are discretized at the cell center, whereas the momentum equations and the velocities are discretized at the cell faces.

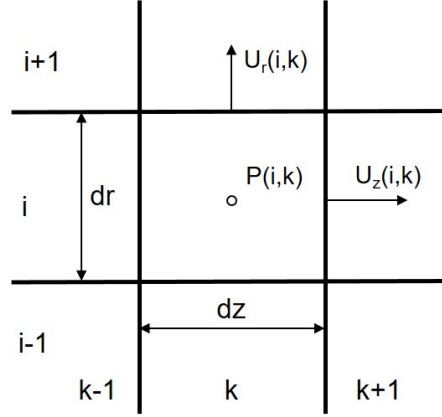


Figure 3-2: Staggered mesh cell

The RANS code solves unsteady two-dimensional streamwise and radial momentum equations 2-59 and 2-60. Energy equation 2-61 is solved by neglecting the temporal derivative, for a faster convergence rate. For all the equations, the radial diffusion terms are discretized implicitly, whereas the rest of the terms are discretized explicitly. For momentum equations, Euler time integration and second-order central differencing schemes are used for temporal and spatial discretization respectively.

The momentum equations are initially solved without considering the pressure gradient. Thus, the intermediate value of momentum does not satisfy mass conservation. After the solution of the pressure Poisson equation, the hydrodynamic pressure field is obtained. It is used to project the intermediate velocities into the space of mass-conserving velocity field. The Fast Fourier Transform (FFT) algorithm is used to solve the Poisson equation for pressure. The derivation of the pressure Poisson equation is outlined below.

The mean momentum equation in tensor notation after using Euler time integration can be written as [7]:

$$(\bar{\rho}\tilde{u}_i)^{n+1} = (\bar{\rho}\tilde{u}_i)^n + \Delta t \left[\left(-\frac{\partial \bar{\rho}\tilde{u}_i\tilde{u}_j}{\partial x_j} + \frac{\partial}{\partial x_j} \left[\left(\frac{\bar{\mu}}{Re_{\tau,0}} + \mu_t \right) \frac{\partial \tilde{u}_i}{\partial x_j} \right] \right)^n - \frac{\partial \bar{p}^{n+1}}{\partial x_i} \right], \quad (3-2)$$

where ‘ n ’ indicates the current timestep.

The intermediate momentum (‘ k ’) can thus be obtained as:

$$(\bar{\rho}\tilde{u}_i)^k = (\bar{\rho}\tilde{u}_i)^n + \Delta t \left[\left(-\frac{\partial \bar{\rho}\tilde{u}_i\tilde{u}_j}{\partial x_j} + \frac{\partial}{\partial x_j} \left[\left(\frac{\bar{\mu}}{Re_{\tau,0}} + \mu_t \right) \frac{\partial \tilde{u}_i}{\partial x_j} \right] \right)^n \right]. \quad (3-3)$$

Upon subtracting equation 3-3 from 3-2 and taking divergence of both sides, we get:

$$\frac{\partial (\bar{\rho}\tilde{u}_i)^{n+1}}{\partial x_i} - \frac{\partial (\bar{\rho}\tilde{u}_i)^k}{\partial x_i} = -\Delta t \frac{\partial^2 \bar{p}^{n+1}}{\partial x_i^2}. \quad (3-4)$$

The continuity equation for a statistically steady flow can be written as:

$$\frac{\partial(\bar{\rho}\tilde{u}_i)^{n+1}}{\partial x_i} = 0. \quad (3-5)$$

Combining equations 3-4 and 3-5, the Pressure Poisson equation is obtained as:

$$\frac{\partial(\bar{\rho}\tilde{u}_i)^k}{\partial x_i} = \Delta t \frac{\partial^2 \bar{p}^{n+1}}{\partial x_i^2}. \quad (3-6)$$

The number of equations solved for the turbulent scalars depends on the turbulence model used. The equations for turbulent scalars are also solved using a steady-state solver for faster convergence. Second-order central differencing is used for spatial discretization. Under-relaxation factors are used in order to avoid stability issues in the code. For discretization of the advection term, the face values of scalars are set using the Koren Slope limiter [37]. This helps avoid the occurrence of spurious oscillations and keeps the code stable.

For both the periodic and developing pipe simulations, no slip and no penetration boundary conditions are enforced at the wall. The inflow generator uses periodic boundary conditions for momentum and scalar equations. The inflow boundary condition for developing flow is obtained from the inflow generator. The convective outflow boundary condition is imposed at the outlet of the developing pipe for the momentum and scalar equations. The boundary conditions for turbulent scalars at the wall are provided in the appendix. The Poisson solver employs a zero Neumann boundary condition at the wall. The inflow generator uses a periodic boundary condition for pressure in the streamwise direction. The developing pipe, however, uses zero Neumann boundary conditions at the inlet and the outlet. For the energy equation, Neumann boundary condition is specified at the wall in the form of heat flux. A constant wall heat flux of $q_w = 0$ and $q_w = 2.4$ are set for the periodic inflow and the developing pipe respectively. Thus, the inflow generator stays isothermal at a reference temperature of $T = 28^\circ C$.

As mentioned before, the use of low Mach approximation allows the assumption of constant thermodynamic pressure. For our cases, we assume a constant pressure of $P_0 = 80 \text{ Bar}$. The thermophysical properties of SCO2 are then obtained by using spline interpolation from a table. Thus, the thermophysical properties are calculated as a function of averaged enthalpy at that point.

The non-dimensionalization of all the equations in this code is with respect to unheated wall parameters, as mentioned in chapter 2.

Case Description and Discussion

This chapter will initially describe the cases from [1] that have been chosen for this thesis. This will be followed by a discussion on how turbulence is modulated by the strong property variation for our cases. Finally, we will evaluate the applicability of SLS and ARN theories for the chosen cases.

4-1 Case description

This thesis aims to determine how far SLS and ARN theories can be utilized to improve turbulence models for heated developing supercritical turbulent flows. For a flow subjected to streamwise body forces resulting from property variations, ARN theory is only valid in the ‘laminarizing’ region. Thus, to utilize ARN theory for turbulence modeling, the cases need to be chosen such that the flows do not laminarize fully in their respective simulation domains.

This implies that for the cases chosen, the shear production should be higher than the buoyancy production, the Reynolds stresses should have a positive value, and the streamwise velocity profile should not attain an ‘M-shape’ for any axial location in the entire simulation domain.

Keeping in mind the above-mentioned, two cases, namely cases A and B from the Ph.D. thesis of Dr. Hassan Nemati [1] have been selected. Both of these cases have SCO2 as the working fluid, a fully developed unheated turbulent flow at the inlet, and a constant heat flux at the wall. The conditions are listed in table 4-1:

Case	Flow dirn.	L/D	P_0 (bar)	T_0 ($^{\circ}C$)	$Re_{\tau,0}$	$Pr_{w,0}$	$1/Fr_{\tau,0}$	q''
A	Horizontal	30	80	28	360	3.19	0	2.4
B	Upwards	30	80	28	360	3.19	-9.96	2.4

Table 4-1: Simulation conditions for Cases A and B

where, $q'' = q_w D / (\lambda_0 T_0) = 2.4$ is the non-dimensional heat flux.

It should be noted that the $Re_{\tau,0}$ has been calculated using the diameter (D) as the length scale. If the radius was instead of the diameter, $Re_{\tau,0}$ for both cases will be equal to 180. All the simulation parameters are identical except $1/Fr_{\tau,0}$ for cases A and B. $1/Fr_{\tau,0} = 0$ in case A implies that the gravity term is not to be considered in the mean streamwise momentum equation. This is because the flow is horizontal and free of buoyancy effects. This case has been chosen despite not having buoyancy because it still has considerable property variation

and thermal acceleration. It would be interesting to compare the performance of the various turbulence models for both cases.

The wall heat flux has been chosen for both cases such that the condition $T_b < T_{pc} < T_w$ is achieved in the simulation domain. The plots of the streamwise evolution of bulk parameters for both cases are inserted below (figure 4-1).

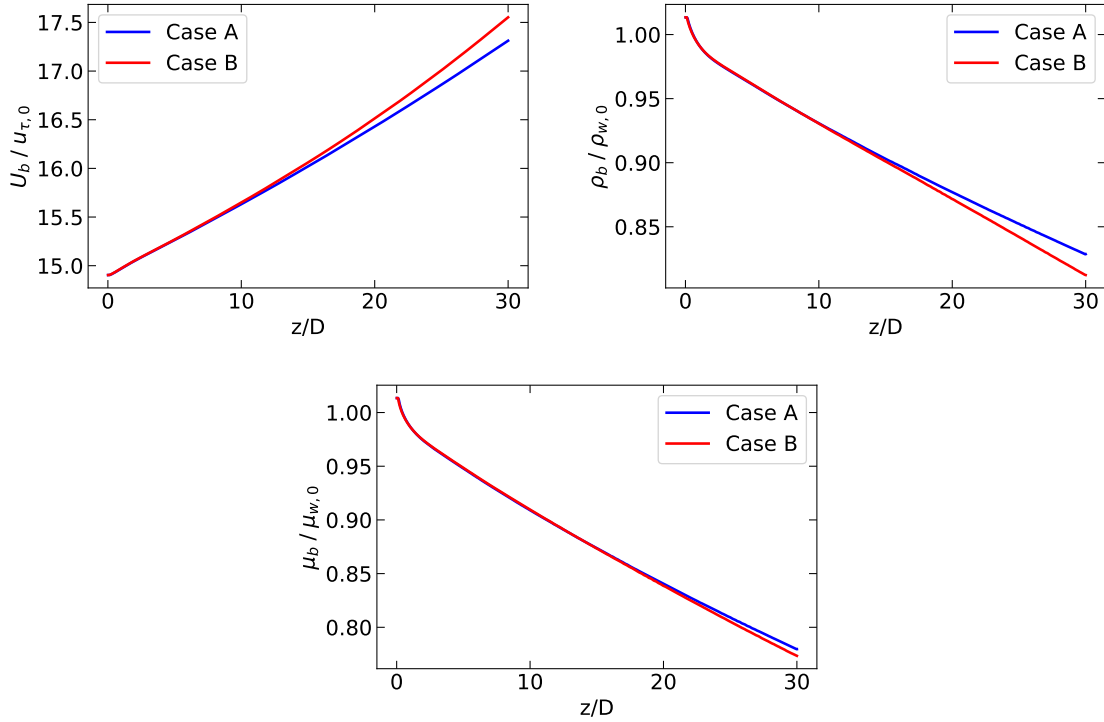


Figure 4-1: Bulk velocity, density and viscosity vs z/D for Cases A and B

Thus, the streamwise bulk velocity increases with z/D for both cases. It increases more in case B due to a stronger effect of thermal acceleration. Case B undergoes a higher heat transfer deterioration, and thus the T_b increases more than it does for case A. This is reflected in the ρ_b and μ_b profiles.

The plots of Re_τ and τ_w for both cases are inserted in figure 4-2.

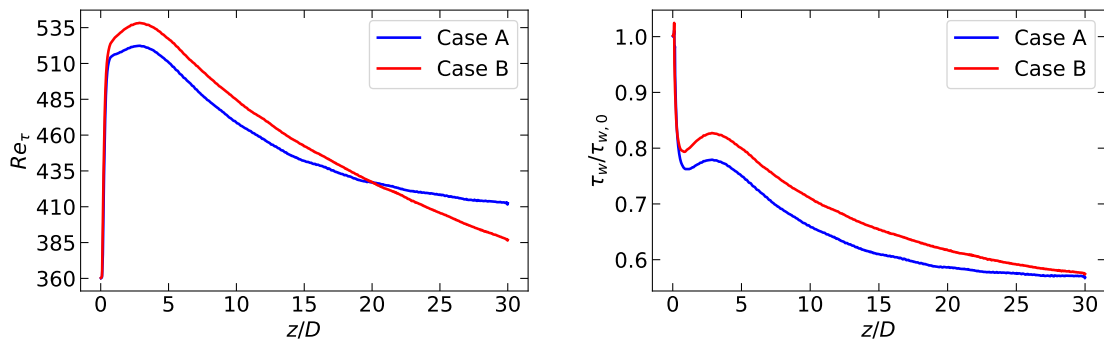


Figure 4-2: Re_τ vs z/D for Cases A and B

Re_τ for both cases is 360 at $z/D = 0$, after which there is a sharp jump in its value, due to the changes in ρ_w and μ_w when the heating starts. τ_w drops more sharply for case A than it does

for case B, as $\frac{\partial \tilde{u}_z}{\partial r}$ at the wall is higher in case B due to a higher effective near-wall acceleration due to buoyancy. This is also reflected in Re_τ till $z/D = 20$. Beyond that axial location, ρ_w and μ_w variations have a stronger effect on Re_τ than τ_w .

Semi-local Reynolds number is defined as $Re_\tau^* = \bar{\rho}^{0.5} \tau_w^{0.5} D / \bar{\mu}$. Plots of Re_τ^* for a few axial locations for both cases are inserted in figure 4-3.

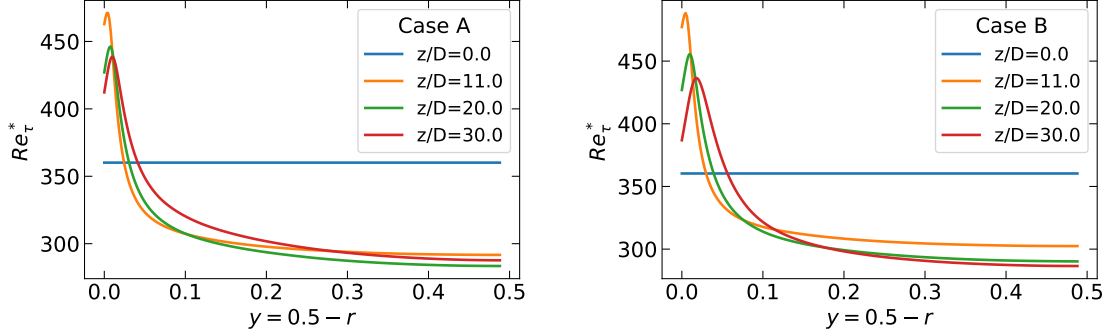


Figure 4-3: Re_τ^* vs y for Cases A and B.

Thus, the variation in Re_τ^* is not monotonic for either case. This is due to the nature of property variation in SCO2 around T_{pc} .

4-2 Discussion

This section will initially elaborate on how exactly the strong property variation affects turbulence in the chosen cases. This is important in order to evaluate the performance of the turbulence models.

Further, a brief description of the Semi-Local Scaling concept will be provided. This will be followed by an assessment of the applicability of the same for cases A and B. Later, we will do the same for the Apparent Reynolds Number theory, and evaluate the possibility of utilizing both theories simultaneously.

4-2-1 Effects of property variation on both cases

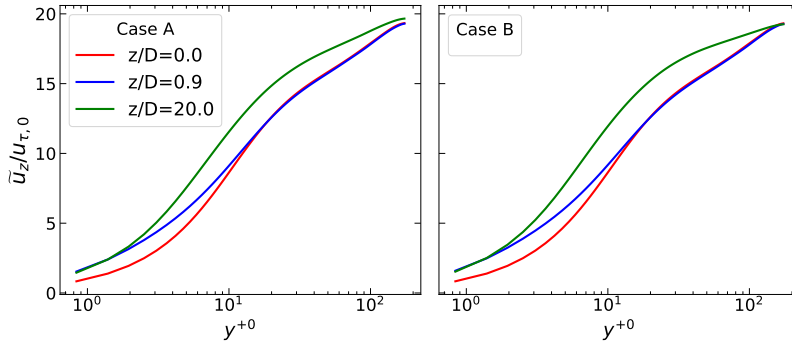


Figure 4-4: $\tilde{u}_z / u_{\tau,0}$ vs y^{+0} for Cases A and B. y^{+0} : scaled using parameters at $z/D = 0$

In subsection 1-1-2, a brief explanation of how strong property variation affects turbulence was provided. We know that a reduction in the density and viscosity in the near-wall region leads

to a near-wall acceleration of the fluid. In the case of vertical flows, we have an additional effect of buoyancy which contributes even more to the near-wall acceleration and core deceleration. These phenomena cause an increment/reduction in the slope of the streamwise velocity profile in the near wall/core regions respectively.

This can graphically be observed from figure 4-4. Both cases experience similar changes in the velocity profile. However, the effects are more pronounced in case B due to buoyancy.

We analyzed the budgets of various turbulent quantities in order to find the repercussions of the above-mentioned effect on turbulence. Following are the observations.

The leading order of magnitude term from the production of $\overline{\rho u_z'' u_z''}$ is $-2\overline{\rho u_r'' u_z''} \frac{\partial \tilde{u}_z}{\partial r}$. For both cases, between $z/D = 0$ and $z/D \approx 5$, the increase in the slope near the wall leads to an increase in the near-wall production (figure 4-5).

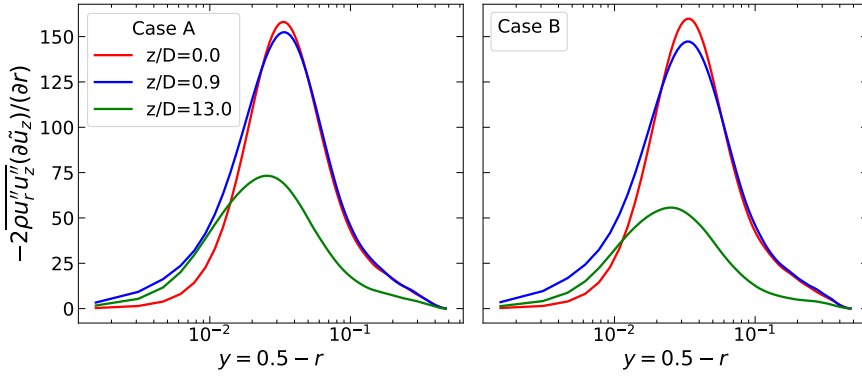


Figure 4-5: $-2\overline{\rho u_r'' u_z''} \frac{\partial \tilde{u}_z}{\partial r}$ vs y for cases A and B.

The changes in the production term naturally reflect in the values of $\overline{\rho u_z'' u_z''}$ in the mentioned region. Similar comments can be made about $\overline{\rho u_r'' u_r''}$ (between $z/D = 0$ and $z/D \approx 5$), as its leading order production term is $-\overline{\rho u_r'' u_r''} \frac{\partial \tilde{u}_z}{\partial r}$ (figure 4-6).

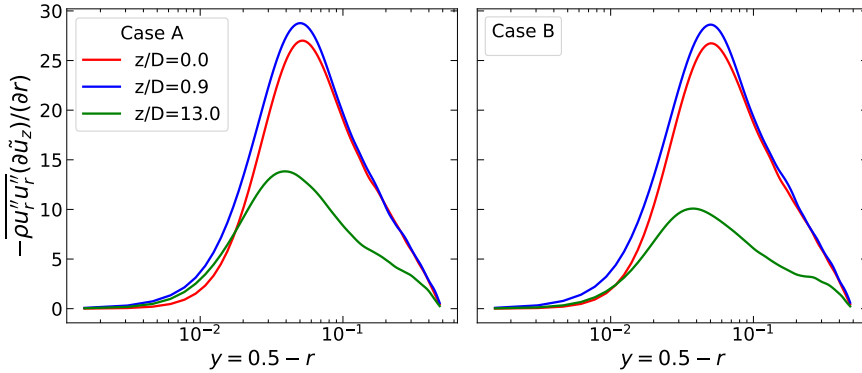


Figure 4-6: $-\overline{\rho u_r'' u_r''} \frac{\partial \tilde{u}_z}{\partial r}$ vs y for cases A and B.

Further, from $z/D = 0$ to $z/D \approx 3.5$, the magnitude of the pressure-strain correlation term also increases in the near-wall region. This term is responsible for transferring energy from streamwise Reynolds stresses to spanwise and wall-normal Reynolds stresses. Consequently, wall-normal and spanwise Reynolds stresses attain a higher value near the wall in the said region (figures 4-7 and 4-8).

Downstream of the said location, we get a steady decrease in the production of $\overline{\rho u_z'' u_z''}$ near the wall (figure 4-5). The reduction is stronger for case B compared to case A. This can not

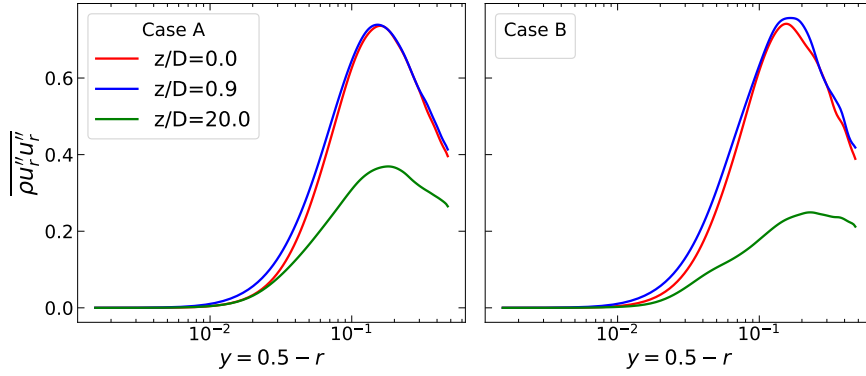


Figure 4-7: $\overline{\rho u_r'' u_r''}$ vs y for cases A and B.

be attributed to the changes in $\frac{\partial \tilde{u}_z}{\partial r}$, as it continues to increase in the near-wall region due to the effects of property variation. The reason for this is unclear, and could not be explained from the budget equation of $\overline{\rho u_z'' u_z''}$. This is a topic that can be looked into in the future. A recommendation for the same is an investigation of the vorticity transport equation.

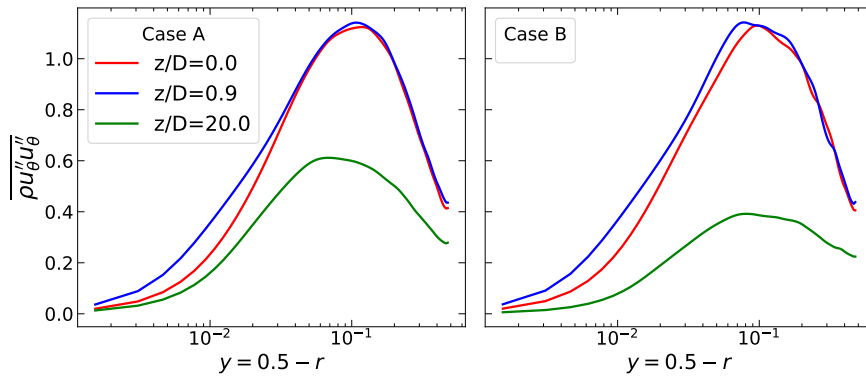


Figure 4-8: $\overline{\rho u_\theta'' u_\theta''}$ vs y for cases A and B.

As discussed, $\frac{\partial \tilde{u}_z}{\partial r}$ shows a gradual reduction in the core region upon moving downstream of the inlet. This reduction is stronger for case B due to the presence of buoyancy. This also reflects in the leading order production terms of $\overline{\rho u_z'' u_z''}$ and $\overline{\rho u_r'' u_z''}$ in the core region (figures 4-5 and 4-6). This effect continuously causes a reduction in shear production of turbulent quantities away from the wall and is the major cause of ‘laminarization’ in our cases. The reduction of streamwise Reynolds stresses in the core region also reflects in the wall-normal and spanwise Reynolds stresses (figures 4-7 and 4-8). This is because the reduction in production of streamwise Reynolds stresses also leads to a reduction in the pressure-strain correlation in the core.

These observations can be summed up as follows. The effects of property variation cause an increase in the near wall value of streamwise Reynolds stresses and Reynolds shear stresses from $z/D = 0$ to $z/D \approx 3.5$. Due to a rise in the near wall value of pressure-strain correlation, we also have an increase in the near wall value of spanwise and wall-normal Reynolds stresses. After this region, there is a steady decrease in normal Reynolds stresses and Reynolds shear stresses as we move further downstream. The reduction is stronger in the core region as compared to the wall. Both cases experience similar effects, however, they are stronger for case B and thus lead to a greater degree of laminarization.

While it is insightful to know about the evolution of Reynolds stresses, eddy viscosity is more important from a turbulence modeling perspective. Eddy viscosity is given by $\nu_t \approx \overline{u_r'' u_z''} / (\frac{\partial \bar{u}_z}{\partial r})$. Due to the mentioned increase in the near wall value of $\overline{\rho u_r'' u_z''}$, we have a higher eddy viscosity in the near wall region from $z/D = 0$ to $z/D \approx 3.5$. Further downstream, we have a reduction in $\overline{\rho u_r'' u_z''}$. Also, $\frac{\partial \bar{u}_z}{\partial r}$ increases/decreases in the near wall/core regions respectively. As a result of these facts, the eddy viscosity progressively reduces and moves towards the core for downstream locations. This can be interpreted as the growth of the viscosity-dominated region/ movement of turbulence away from the wall. This effect is much stronger for case B (figure 4-9).

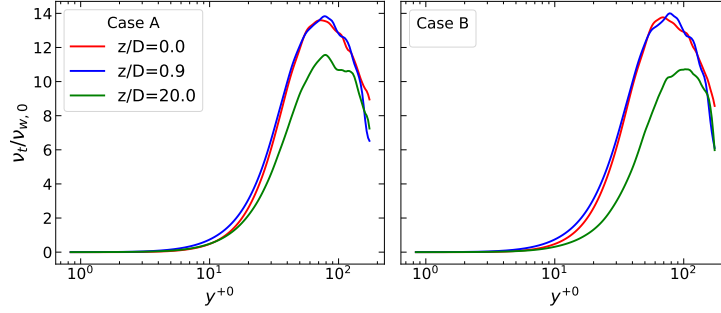


Figure 4-9: $\nu_t/\nu_{w,0}$ vs y^{+0} for cases A and B. y^{+0} : scaled using parameters at $z/D = 0$

Thus, the primary RANS modeling challenges are expected to be:

- Accurate estimation of the reduction in turbulent production term(s).
- The movement of eddy viscosity towards/away from the wall, depending on the axial location.

4-2-2 Semi-local scaling

Patel et al. (2015) [27] investigated if semi-local scaling can be used as a universal near-wall coordinate for fully developed flows with variable properties. Mathematically, they assessed the following hypothesis:

$$\overline{\rho u_i'' u_j''} / \tau_w \approx f(y^*, Re_\tau^*). \quad (4-1)$$

The above-mentioned would imply that for wall-bound turbulent flows, the turbulent statistics at a given scaled wall-normal location will depend only on the Re_τ^* profile. In other words, they assess if turbulent statistics are similar for variable property flows with different density and viscosity profiles, but similar Re_τ^* profiles.

They substituted semi-locally scaled variables in conventionally-scaled mass and momentum conservation equations. After applying Morkovin's hypothesis [8] and a few other assumptions, the following equation was obtained for a fully-developed flow:

$$\partial_{x_j} \left(\frac{\overline{\rho u_i'' u_j''}}{\tau_w} \right) \approx \partial_{x_i} \left(\frac{\bar{p}}{\tau_w} \right) + \partial_{x_j} \left(\frac{1}{Re_\tau^*} \partial_{x_j} \bar{u}_i^{vD} \right), \quad (4-2)$$

where the Einstein notation has been utilized for the sake of brevity, and \bar{u}_i^{vD} is the van Driest transformed velocity, given by $\partial \bar{u}_i^{vD} = \sqrt{\bar{\rho} / \rho_w} \partial \bar{u}_i$.

Since the streamwise pressure gradient is constant for a fully developed flow, the only governing parameter in this PDE is Re_τ^* . Thus, for flows that meet the criteria assumed in the derivation,

similar Re_τ^* profiles will yield similar $\overline{u_i^{vD}}$ and $\overline{\rho u_i'' u_j''}$ profiles. Patel et al. (2015) [27] carried out numerical experiments of fully developed flows with different Re_τ^* profiles, and successfully confirmed their hypothesis.

Upon using the same recipe for spatially developing variable property flows in a vertical orientation, we obtain the following equation:

$$\partial_{x_j} \left(\frac{\overline{\rho \tilde{u}_i \tilde{u}_j}}{\tau_w} \right) + \partial_{x_j} \left(\frac{\overline{\rho u_i'' u_j''}}{\tau_w} \right) \approx \partial_{x_i} \left(\frac{\overline{p}}{\tau_w} \right) + \partial_{x_j} \left(\frac{1}{Re_\tau^*} \partial_{x_j} \overline{u_i^{vD}} \right) \pm \frac{\overline{\rho} g h}{\tau_w} \quad (4-3)$$

Where h is the characteristic length and g is the acceleration due to gravity.

Even far away from the entrance such that we have a constant pressure gradient, the governing parameter for this PDE is not Re_τ^* , as the buoyancy and inertia terms are not governed by it.

Further, Patel et al. (2016) [38] reported that when semi-locally scaled turbulent shear stresses are plotted against y^* , a universal collapse is obtained in the inner layer for fully developed turbulent flows with strong property variation. This collapse is obtained regardless of the individual Re_τ^* profiles.

Upon wall normal integration of the semi-locally scaled streamwise momentum equation for a fully developed turbulent flow with small property fluctuations and no buoyancy, the following expression is obtained:

$$-\widetilde{\hat{u}'_z \hat{u}'_r} + \frac{h}{Re_\tau^*} \frac{\partial \overline{u_z^{vD}}}{\partial y} \approx \frac{\tau}{\tau_w} = \left(1 - \frac{y}{h} \right), \quad (4-4)$$

where the terms on the left-hand side are semi-locally scaled turbulent and viscous stresses.

In the inner region, $y \ll h$, and thus the total stresses are approximately constant for fully developed flows. Hence, the semi-locally scaled viscous stresses are also expected to provide a universal collapse in the inner region as a function of y^* . This fact was used to derive a universal scaling of streamwise velocity for variable property flows.

Fully developed flows in the absence of buoyancy are balanced only by the contribution of the streamwise pressure gradient. This happens to be linear, and thus in the inner region, it can be assumed to be approximately constant. However, in the flows complicated by spatial development and buoyancy, the total stresses are balanced by a combination of inertia and buoyancy forces and streamwise pressure gradient. While the inner region contributions from pressure gradient and inertia can be assumed to be approximately constant, the buoyancy contribution varies very sharply. Thus, it is not necessary for semi-locally scaled viscous stresses to provide a universal collapse for cases with buoyancy.

The above-mentioned discussion was purely on analytical grounds. It implies that semi-local scaling might not necessarily work for flows with spatial development and buoyancy. However, whether SLS is an effective tool to characterize developing flows with buoyancy depends on the strength of the aforementioned effects.

Silvestri et al. [39] have assessed the applicability of SLS to thermally expanding/contracting horizontal channel flows. They reported that after a certain distance in the streamwise direction, a 'return to equilibrium' region was observed. In this region the semi-locally scaled turbulent structures can be assumed to be self-similar. We need to assess if the same can be said about any of the cases being investigated.

Since cases A and B are spatially developing, we will treat each axial location analogous to a different case and investigate the collapse of a few SLS quantities. We have inserted plots of SLS turbulent and viscous stresses y^* for both cases (figures 4-10 and 4-13).

From figure 4-10, it can be seen that for case A, a fairly good collapse of SLS turbulent stresses can be obtained for axial locations downstream of $z/D \approx 5$. For case B however, a good collapse

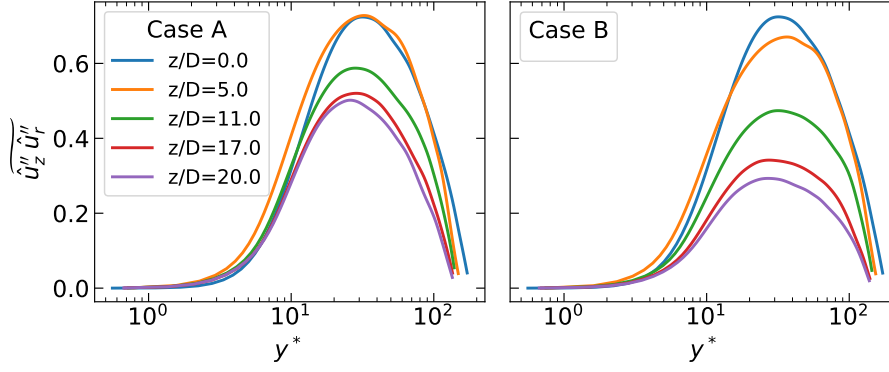


Figure 4-10: SLS turbulent stresses vs y^* for cases A and B

is not obtained for any range of axial locations. A considerable reduction in SLS turbulent stresses and a movement away from the wall is observed upon progressing downstream. In order to find out the reason for the same, a slightly deeper understanding of SLS theory is necessary.

Semi-local scaling primarily helps account for ‘local effects’. This refers to the compressibility effects caused by mean property variation in the wall-normal direction. Also, within the SLS framework, the variation in Re_τ^* matters, and not the variation in individual properties.

From Patel et al. (2016) [38], one of the effects of strong property variation is to modulate the inter-component energy transfer. When $dRe_\tau^*/dy > 0$, more energy is transferred from the streamwise to the spanwise Reynolds stresses, compared to $dRe_\tau^*/dy = 0$ cases. This leads to a decrease/increase in streamwise/spanwise turbulent stress anisotropies respectively.

Where turbulent stress anisotropy is defined as

$$b_{ij} = \frac{\overline{u_i'' u_j''}}{\tilde{k}} - \frac{\delta_{ij}}{3}. \quad (4-5)$$

The opposite happens for $dRe_\tau^*/dy < 0$ cases. However Patel et al. (2016) [38] report that $dRe_\tau^*/dy \neq 0$ does not affect the wall-normal Reynolds stress anisotropy. The modulation of inter-component energy transfer due to $dRe_\tau^*/dy \neq 0$ is only restricted to streamwise and spanwise Reynolds stresses.

Thus, wall-normal Reynolds stress anisotropy remains unchanged due to variations in local properties. The production of Reynolds shear stresses depends on wall-normal Reynolds stresses. To get a good collapse of SLS Reynolds shear stresses for different axial locations, the wall-normal Reynolds stress anisotropy needs to remain relatively unaffected across those axial locations. The plots of wall-normal Reynolds stress anisotropy against y^* are inserted in figures 4-11 and 4-12.

Thus, in the region between $z/D = 0$ to $z/D \approx 5$, $b_{u_r u_r}$ is modified even in the near wall region for both cases (figure 4-11). This explains why SLS turbulent stresses from figure 4-10 do not collapse in the mentioned region for either case.

Figure 4-12 presents $b_{u_r u_r}$ for a few axial locations downstream of $z/D \approx 5$. For the locations investigated in figure 4-12, we get a good collapse for case A. Thus, we obtain a ‘return to equilibrium’ region in case A upon moving sufficiently downstream. However, for case B, we do not get a good collapse of $b_{u_r u_r}$. This explains the discrepancy between the collapse of SLS turbulent shear stresses from figure 4-10

The discussion and observations can be summed up as follows.

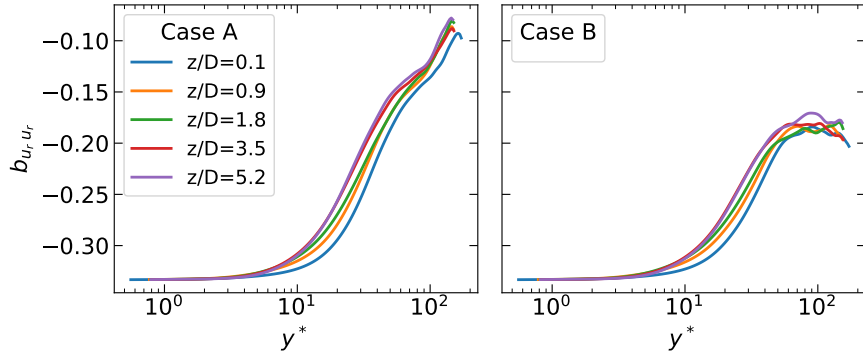


Figure 4-11: Wall normal Reynolds stress anisotropy vs y^* for cases A and B

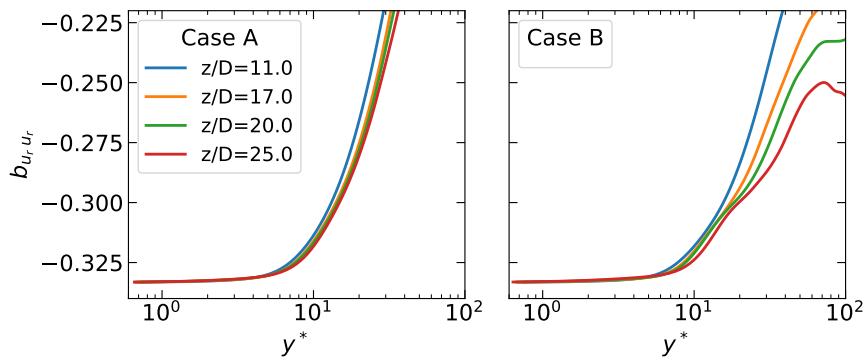


Figure 4-12: Wall normal Reynolds stress anisotropy vs y^* for cases A and B

- During the initial region (between $z/D = 0$ and $z/D \approx 5$), we have a strong change in the wall-normal Reynolds stress anisotropy for both cases. This does not result from a local variation of properties and SLS cannot effectively characterize the turbulence for either case in the mentioned region.
- For case A, upon moving sufficiently downstream, the turbulence can be characterized well by SLS.
- For case B, the dominant effects of heating on turbulence are not due to local property variation. Thus, SLS by itself is not expected to be enough to characterize this flow.

Plots of SLS viscous stresses are attached in figure 4-13. Since we do not get an excellent collapse of this quantity against y^* , the universal velocity transformation is not going to work for our cases. From the figure, the collapse of SLS viscous stresses is similar to the collapse of SLS turbulent stresses for case A. However, for case B, the collapse of SLS turbulent stresses is much worse than SLS viscous stresses. This discrepancy can be attributed to the fact that case B has the presence of buoyancy force. As discussed before, this renders the assumption of constant total stresses in the near-wall region invalid.

4-2-3 ARN theory

The Apparent Reynolds Number (ARN) theory was introduced in the literature review section of this thesis. It proposes that the turbulent statistics and eddy viscosity of a flow subjected to streamwise non-uniform body forces (resulting from property variation and inertia in our cases)

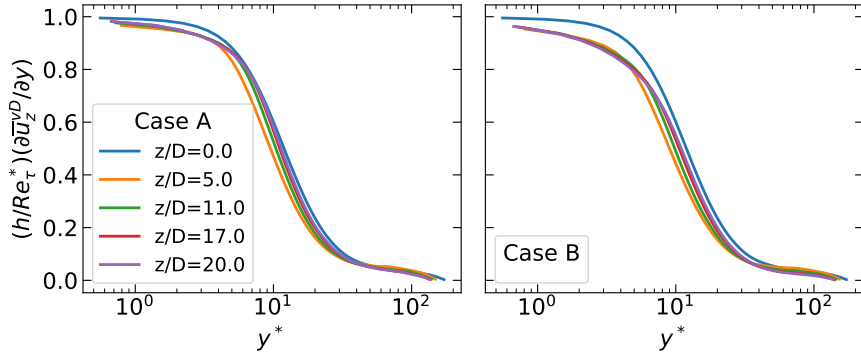


Figure 4-13: SLS viscous stresses vs y^* for cases A and B

remain largely unchanged with respect to its EPG reference flow. The latter is a constant property fully developed turbulent flow at a different Reynolds number, known as the Apparent Reynolds number. This theory is explained in more detail in chapter 5.

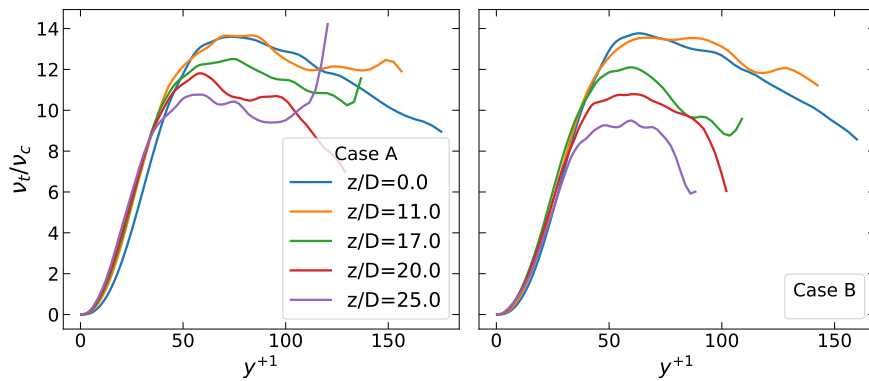


Figure 4-14: Eddy viscosity scaled with centerline viscosity vs y^{+1} for cases A and B

Further, S. He et al. [28] and J. He et al. [4] proposed that the quantity ' y^{+1} ' as the scaled wall normal distance, which is the y^+ of the EPG reference flow. If this theory holds for our cases, we should get a good collapse of eddy viscosity against y^{+1} . Plots of the same for both cases are inserted in figure 4-14.

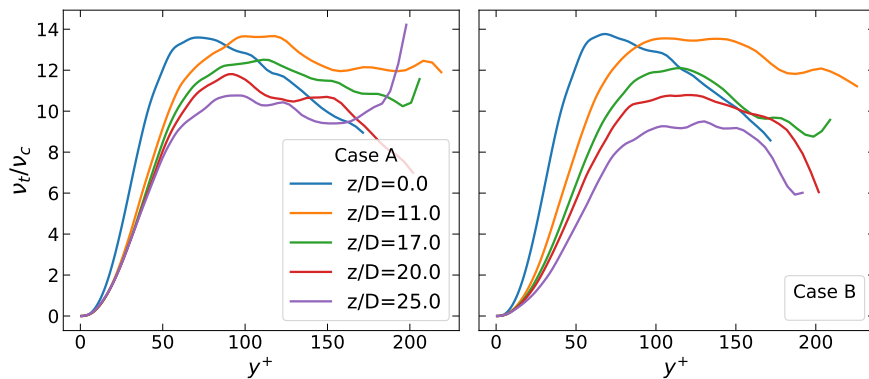


Figure 4-15: Eddy viscosity scaled with centerline viscosity vs y^+ for cases A and B

In order to provide a reference for comparison, plots of eddy viscosity against y^+ are inserted in figure 4-15.

Thus, it can be observed that plotting eddy viscosity against y^{*1} provides a much better collapse than against y^+ . Similar results have been obtained for turbulent stresses. This makes it tempting to use ARN theory to improve predictions of turbulence models for both cases A and B. However, the use of the theoretical framework proposed by J. He et al. [4] requires the thermophysical property distribution of the final flow field. This can not be known before carrying out the simulation, because the velocity and thermal fields are strongly coupled. In order to try and circumvent this issue, a methodology to use ARN with RANS is proposed in chapter 5.

4-2-4 Simultaneous application of SLS and ARN theories

In the context of heated developing supercritical turbulent flows, SLS is not guaranteed to provide better results, as it does not inherently account for strong buoyancy and thermal acceleration effects. Also, ARN theory is an approximation, and a perfect collapse is not always obtained using the same. This raises the question of whether a better collapse of eddy viscosity could be obtained by combining concepts from both theories.

SLS makes use of locally averaged properties for defining y^* along with the wall shear stress. ARN utilizes the averaged properties at the centerline along with the wall shear stress of the EPG reference flow (τ_{wp}) for defining y^{*1} . If we construct a new parameter such that it makes use of locally averaged properties and τ_{wp} , we get:

$$y^{*1} = \frac{\bar{\rho}^{0.5} \tau_{wp}^{0.5} y}{\bar{\mu}} \quad (4-6)$$

Thus, making y^{*1} as the scaled distance could help us account for the effects of wall-normal variations of averaged properties along with effects that can not be characterized well by SLS. In order to verify the same, plots of eddy viscosity against y^{*1} for both cases are inserted below (figure 4-16). It is scaled with locally averaged viscosity, to be consistent with equation 4-6.

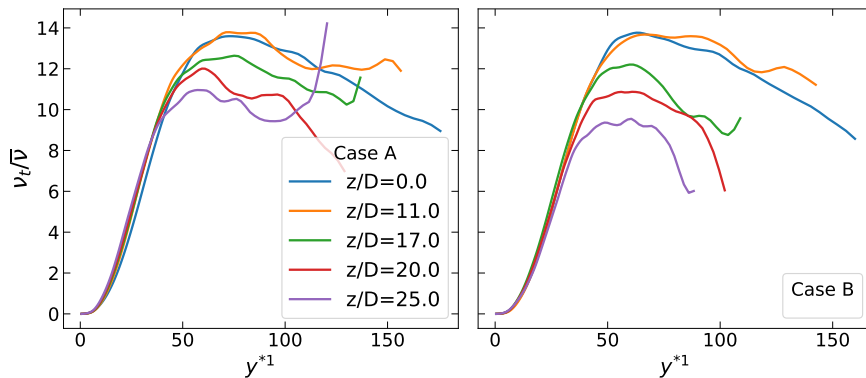


Figure 4-16: Eddy viscosity scaled with locally averaged viscosity vs y^{*1} for cases A and B

It can be observed that a slightly better collapse in the near wall region is obtained upon plotting eddy viscosity against y^{*1} . This can be thought of as sensitizing SLS to the additional effects arising from the streamwise body forces (inertia and buoyancy). This concept will also be utilized in our effort to improve turbulence model predictions.

The following chapter will describe the methodology developed in order to use the previously mentioned theories in a turbulence modeling context.

Chapter 5

Methodology

This chapter will initially provide an in-depth explanation of ARN theory and outline how it can practically be used with DNS data. Then, a method to do the same in RANS context will be proposed. Finally, a method to simultaneously use SLS and ARN theories for RANS will be proposed.

5-1 ARN theory

This theory proposes that the turbulence characteristics of flows with strong property variation (or flows subjected to streamwise body forces) remain unchanged with respect to their ‘EPG reference flow’. The EPG reference flow as discussed in [4] is a constant property fully developed turbulent flow. Thus, the commonly used turbulence models can be used in order to give a good estimation of the eddy viscosity of EPG reference flow. This eddy viscosity could then be used to solve the mean flow equations of the actual flow. In order to fully understand this claim, it is important to understand how the ARN theory actually works. An in-depth explanation along with the relevant equations will be provided below.

Consider the example of a fully developed turbulent flow with density and viscosity variations. For now, this flow will be referred to as the ‘total flow’. The streamwise mean momentum equation for the same after invoking the eddy viscosity hypothesis is given as follows:

$$-\frac{\partial \bar{p}}{\partial z} + \frac{1}{r Re_{\tau,0}} \frac{\partial}{\partial r} \left(r (\bar{\rho} \nu_t + \bar{\mu}) \frac{\partial \bar{u}_z}{\partial r} \right) = 0, \quad (5-1)$$

where, $\nu_t = \mu_t / \bar{\rho}$.

The streamwise mean momentum equation for the EPG reference flow of the above-mentioned flow is given by:

$$-\frac{\partial \bar{p}_p}{\partial z} + \frac{1}{r Re_{\tau,0}} \frac{\partial}{\partial r} \left(r (\rho_p \nu_{tp} + \mu_p) \frac{\partial \bar{u}_p}{\partial r} \right) = 0. \quad (5-2)$$

Here, the subscript ‘p’ stands for EPG reference flow, and u_p is its streamwise velocity. ρ_p and μ_p are equal to the centerline values of $\bar{\rho}$ and $\bar{\mu}$ from the total flow.

$-\left(\frac{\partial \bar{p}_p}{\partial z}\right)$ is the driving force of the EPG reference flow. According to [4], whether $\frac{\partial \bar{p}_p}{\partial z}$ is the same as $\frac{\partial \bar{p}}{\partial z}$ or not depends on the nature of body forces acting on the flow. Fully nonlinear body forces (non-zero gradient of body force in wall normal direction) do not alter the turbulence

dynamics and do not cause $\frac{\partial \bar{p}_p}{\partial z}$ to deviate from $\frac{\partial \bar{p}}{\partial z}$. The body forces acting on the flow due to viscosity and density variation (equations 5-6 and 5-7) are in fact fully nonlinear. This implies:

$$\frac{\partial \bar{p}}{\partial z} = \frac{\partial \bar{p}_p}{\partial z}. \quad (5-3)$$

Upon subtracting equation 5-2 from equation 5-1, and rearranging a few terms, we get the governing equation of the ‘perturbation flow’ (subscript ‘f’, explained below):

$$\frac{1}{rRe_{\tau,0}} \frac{\partial}{\partial r} \left(r (\bar{\rho}\nu_{tp} + \bar{\mu}) \frac{\partial \bar{u}_f}{\partial r} \right) + f_{1b} + f_{1c} = 0, \quad (5-4)$$

where,

$$\bar{u}_f = \tilde{u}_z - \bar{u}_p, \quad (5-5)$$

$$f_{1b} = \frac{1}{rRe_{\tau,0}} \frac{\partial}{\partial r} \left(r (\bar{\mu} - \mu_p) \frac{\partial \bar{u}_p}{\partial r} \right), \quad (5-6)$$

$$f_{1c} = \frac{1}{rRe_{\tau,0}} \frac{\partial}{\partial r} \left(r (\bar{\rho} - \rho_p) \frac{\partial \bar{u}_p}{\partial r} \right). \quad (5-7)$$

The physical interpretation of these equations is as follows. The ‘total flow’ can be represented as the sum of the EPG reference flow (equation 5-2) and the perturbation flow (equation 5-4). The effect of property variations on the flow can be looked at as ‘pseudo body forces’, which are given by f_{1b} and f_{1c} . Thus, the density and viscosity variation leads to (and acts as a driving force for) a perturbation flow on the top of the EPG reference flow. Also, the EPG reference flow and perturbation flow both have their own turbulent shear stresses. Their contributions can thus be summed up to obtain the turbulent shear stress of the total flow. It should be noted that the eddy viscosity of the total flow and the perturbation flow are the same as the eddy viscosity of the EPG reference flow, which is the main claim of this theory.

For the sake of simplicity, the above-mentioned explanation was for fully developed flows with density and viscosity variation. However, the flows that are relevant to this thesis are further complicated by spatial development (inertia) and buoyancy force in the streamwise direction. The streamwise momentum equation for such flows far enough from the start of the heating ($z/D > 1$) is given by:

$$-\frac{\partial(\bar{\rho}\tilde{u}_z\tilde{u}_z)}{\partial z} - \frac{1}{r} \frac{\partial(r\bar{\rho}\tilde{u}_r\tilde{u}_z)}{\partial r} - \frac{\partial \bar{p}}{\partial z} + \frac{1}{rRe_{\tau,0}} \frac{\partial}{\partial r} \left(r(\bar{\rho}\nu_t + \bar{\mu}) \frac{\partial \tilde{u}_z}{\partial r} \right) - \frac{\bar{\rho}}{Fr_{\tau,0}^2} = 0. \quad (5-8)$$

For further discussion, this flow will be referred to as the total flow. It was proposed in [4] that the effect of inertia and buoyancy forces can also be explained using ARN theory. However, the nature of body forces acting on the flow due to inertia and buoyancy is different than the body forces acting merely due to density and viscosity variation. This is because the body forces due to inertia and buoyancy are not fully non-linear. The linear part of the body forces due to inertia and buoyancy will affect the turbulence dynamics, and hence the driving force of the EPG reference flow.

Thus, it is necessary to split these forces into their linear and non-linear components. J. He et al. [4] propose that the value of these forces at the center of the pipe be taken as the linear component. The non-linear component can then be obtained by subtracting the linear component from the total force. Mathematically, it can be explained as follows:

Let the inertia force, its uniform, and non-uniform components be represented by f_2 , f_{2U} , and f_{2N} respectively.

$$f_2 = -\frac{\partial(\bar{\rho}\tilde{u}_z\tilde{u}_z)}{\partial z} - \frac{1}{r} \frac{\partial(r\bar{\rho}\tilde{u}_r\tilde{u}_z)}{\partial r}. \quad (5-9)$$

$$f_{2U} = f_2(r=0). \quad (5-10)$$

$$f_{2N} = f_2 - f_2(r=0) = f_2 - f_{2U}. \quad (5-11)$$

Similarly, let the buoyancy force, its uniform, and non-uniform components be represented by f_{1a} , $f_{1a,U}$ and $f_{1a,N}$.

$$f_{1a} = -\frac{\bar{\rho}}{Fr_{\tau,0}^2}. \quad (5-12)$$

$$f_{1a,U} = f_{1a}(r=0) = -\frac{\bar{\rho}_c}{Fr_{\tau,0}^2}. \quad (5-13)$$

$$f_{1a,N} = f_{1a} - f_{1a}(r=0) = -\frac{(\bar{\rho} - \bar{\rho}_c)}{Fr_{\tau,0}^2}. \quad (5-14)$$

Thus, the driving force of the EPG reference flow is the summation of all the uniform forces in the domain. This driving force, referred to as the total modified pressure gradient is given by:

$$-\left(\frac{\partial P}{\partial z}\right)_p = -\frac{\partial \bar{p}}{\partial z} + f_{1a,U} + f_{2U} = -\frac{\partial \bar{p}}{\partial z} - \frac{\bar{\rho}_c}{Fr_{\tau,0}^2} + f_{2U}. \quad (5-15)$$

Consequently, the streamwise momentum equation of the EPG reference flow for developing flows with effects of buoyancy, inertia and property variation is given by:

$$-\left(\frac{\partial P}{\partial z}\right)_p + \frac{1}{rRe_{\tau,0}} \frac{\partial}{\partial r} \left(r(\rho_c \nu_{tp} + \mu_c) \frac{\partial \bar{u}_p}{\partial r} \right) = 0. \quad (5-16)$$

The streamwise momentum equation for the perturbation flow is given by:

$$\frac{1}{rRe_{\tau,0}} \frac{\partial}{\partial r} \left(r(\bar{\rho}\nu_{tp} + \bar{\mu}) \frac{\partial \bar{u}_f}{\partial r} \right) + f_{1a,N} + f_{1b} + f_{1c} + f_{2N} = 0. \quad (5-17)$$

Where, $f_{1a,N}$, f_{1b} , f_{1c} and f_{2N} can be obtained from equations 5-14, 5-6, 5-7 and 5-11 respectively.

To reiterate, this theory implies that the non-uniform body forces do not affect the eddy viscosity of the total flow. They just cause a perturbation flow which can be summed up with the EPG reference flow to obtain the total flow. It is important to note that each axial location in the total flow will have a different EPG reference flow, as the pseudo-body forces will depend on the thermophysical property distribution at that point.

In order to graphically illustrate the above-mentioned, the plot of streamwise mean momentum balance at the axial location $z/D=25$ from the 'Case B' of [1] is inserted (figure 5-1).

The plot on the left shows the contribution by total source term (Buoyancy + Inertia + Pressure gradient) and total stress. The plot on the right shows the linear components of the total source and stress along with the total source and stress. The plot of the linear components is the same as the streamwise mean momentum budget of the EPG reference flow corresponding to $z/D=25$. Thus, ARN theory claims that the eddy viscosity of the flow represented by the dotted lines is the same as the eddy viscosity of the flow represented by the solid lines (figure 5-1).

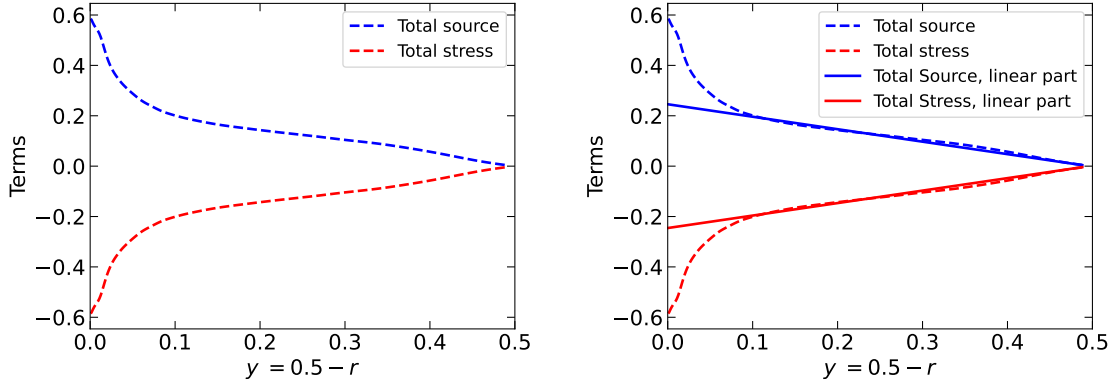


Figure 5-1: Streamwise mean momentum budget, case B [1]

The claim made in the last line of the previous paragraph is quite strong, and it needs to be substantiated. This is where the quantity y^{+1} comes into the picture. y^{+1} is defined as follows:

$$y^{+1} = \frac{\bar{\rho}_c y u_{\tau p}}{\bar{\mu}_c}, \quad (5-18)$$

where,

$$u_{\tau p} = \sqrt{\frac{\tau_{wp}}{\bar{\rho}_c}}. \quad (5-19)$$

τ_{wp} is defined as the linear contribution of total stress at the wall. It is the same as the total stress at the wall for the EPG reference flow. It is given by:

$$\tau_{wp} = -\frac{R}{2} \left(\frac{\partial P}{\partial z} \right)_p. \quad (5-20)$$

Thus, y^{+1} of the total flow is in fact y^{+} of the EPG reference flow at that axial location. Getting a good collapse of eddy viscosity against y^{+1} indicates that the leading order effect of property variation and body forces on a flow can be captured well by ARN theory.

In figure 4-14, we have shown that ν_t indeed collapses well against y^{+1} . S. He et al. [4] and J. He et al. [28] have tested out this theory on multiple flows subjected to streamwise body forces, and have reported a successful collapse of ν_t against y^{+1} .

J. He et al. [4] have made use of the theoretical framework mentioned above, in order to reconstruct the total flow using ARN theory. In order to take inspiration from this theory for RANS modeling, it is important to understand the same. The procedure followed by them is discussed in the following section.

5-2 Reconstruction of flow field using ARN theory

The key statement of ARN theory is that the total flow can be represented by the EPG reference flow plus a perturbation flow induced by pseudo-body forces.

The algorithm 1 can be followed in order to reconstruct the total flow using ARN theory. Its goal is not to build a predictive model, it is just to evaluate the applicability of the claims made in the paper. Thus, it assumes that one has the DNS data of the total flow, and also access to DNS data of standard unheated pipe flows at various Re_τ

Algorithm 1 Reconstruction of the total flow field using ARN theory

Require: DNS data of total flow.

Calculate $\left(\frac{\partial P}{\partial z}\right)_p$ using equation 5-15.

Compute τ_{wp} .

$$\tau_{wp} \leftarrow -(\mathbf{R}/2)(\partial P/\partial z)_p.$$

Compute $Re_{\tau p}$.

$$Re_{\tau p} \leftarrow (\bar{\rho}_c^{0.5} \tau_{wp}^{0.5} D) / \bar{\mu}_c.$$

Obtain \mathbf{u}_p and ν_{tp} of a standard unheated flow at $Re_{\tau} = Re_{\tau p}$.

Calculate total pseudo body force:

$$\mathbf{f}_T \leftarrow \mathbf{f}_{1a} + \mathbf{f}_{1b} + \mathbf{f}_{1c} + \mathbf{f}_{2N} \text{ (use equations 5-14, 5-6, 5-7 \& 5-11)}.$$

Calculate the velocity field of perturbation flow ($\bar{\mathbf{u}}_f$) (use equation 5-17).

Sum up equations 5-16 and 5-17 to obtain the total flow.

J. He et al. [4] followed the steps mentioned in algorithm 1 and showed the reconstructed flow field for two different flows. Although this framework can't directly be used in order to make RANS modeling improvements, borrowing a few concepts can prove useful for the same. The approach followed for improving RANS models will be discussed in the next section.

5-3 ARN theory to improve RANS models

The scope of this thesis has been limited to eddy viscosity turbulence models. Their main function is to provide the relevant turbulent length and time scales to compute the eddy viscosity. This eddy viscosity is then used by the mean flow equations to provide closure for the relevant turbulent quantities.

Based on the explanation provided in the previous section, it is clear that the eddy viscosity of flows with property variation and streamwise body forces primarily depends on the ARN, which is calculated from the driving force of EPG reference flow. This driving force is a function of the linear part of the source (or total stress) term of the total flow.

If we can calculate the driving force and the ARN of EPG reference flow at each location, we could obtain the eddy viscosity of the same. This eddy viscosity is the same as the eddy viscosity of the total flow and can be provided to the mean flow equations of the total flow. In other words, we solve the turbulence model equations for the EPG reference flows instead of the total flow.

The prediction of the driving force of the EPG reference flows a priori proved to be a challenging task. It was not possible with the current understanding of the theory. Making a good prediction of $\left(\frac{\partial P}{\partial z}\right)_p = f(\tau_{wp})$ is a topic that could be pursued in the future. Currently, the value of τ_{wp} has been taken from the DNS data.

After getting τ_{wp} , $Re_{\tau p}$ for every iteration can be calculated using $\bar{\rho}_c$ and $\bar{\mu}_c$ corresponding to the total flow field. $\bar{\rho}_c$ and $\bar{\mu}_c$ will approach their true values as the simulation converges. The task that remains, is computing the eddy viscosities of the EPG reference flow(s).

Ideally, this would involve carrying out constant property periodic RANS simulations at each axial location, with $Re_{\tau} = Re_{\tau p}$. The goal would be to obtain μ_t at each axial location, which in turn needs $Re_{\tau p}$, and the streamwise (u_p) and wall-normal (v_p) velocity fields of the EPG reference flow. However, solving for u_p and v_p would be computationally expensive due to the convergence requirements of inner iterations at each timestep. This process could be bypassed if we could get an approximation of u_p and v_p necessary for the turbulence model instead of having to solve for the same. This would allow us to only have to solve the equations for turbulent

scalars and calculate μ_t .

Thus, Re_{τ_p} can be computed as mentioned before, $v_p = 0$ for a fully developed flow, and u_p can be approximated by integrating the equation 5-16.

The following algorithm was followed in order to utilize ARN theory for RANS modeling. However, as mentioned before, this assumes the knowledge of τ_{wp} (and thus $(\frac{\partial P}{\partial z})_p$) a priori.

Algorithm 2 Modification of RANS solver with ARN theory

Require: $(\frac{\partial P}{\partial z})_p = f(\tau_{wp})$

Initialize the flow field with periodic inflow.

Start iterating.

if Residuals > Convergence criteria **then**

Obtain the fields of the EPG reference flows as follows:

Set $\mathbf{v}_p \leftarrow 0$.

Obtain \mathbf{u}_p (equation 5-16).

Set $\bar{\rho}_p = \bar{\rho}_c$, $\bar{\mu}_p = \bar{\mu}_c$.

Solve the turbulence model equations for the EPG reference flows and obtain μ_t

Calculate α_t from μ_t

Solve the mean energy equation (use α_t).

Solve the mean momentum equations (use μ_t).

end if

5-4 Combining SLS and ARN theories

In the previous chapter, the possibility of simultaneously utilizing SLS and ARN theories was discussed. This was based on the good collapse of eddy viscosity obtained upon plotting it against y^{*1} given by equation 4-6. The physical interpretation of this can be explained as follows.

We know from section 5-1, that ARN theory is capable of characterizing wall-normal variation of properties in fully developed flows. It does so by approximating the eddy viscosity of the total flow with the eddy viscosity of the EPG reference flow. However, this is an approximation. It leads to some errors in the reconstruction of the total flow field using ARN theory, as can be found in [28] and [4]. The same can be said about the use of ARN to characterize buoyancy and inertia forces.

We know that SLS has a high level of accuracy when it comes to characterizing fully developed turbulent flows with strong property variation. Thus, if our reference flow was a variable property fully developed flow, SLS turbulence model equations [35] could be used in order to get an accurate prediction of the same. Thus, the errors from the use of ARN would only be limited to the effects of inertia and buoyancy forces.

This would involve making the modulation in turbulent shear stresses and viscous friction due to mean property variation (refer subsection 1-1-2) a part of the reference flow itself. The body forces that arise due to the changes in turbulent shear stress and viscous friction are f_{1b} (equation 5-6) and f_{1c} (equation 5-7). Thus, they will not be a part of the perturbation flow. It will only be caused by inertia (f_{2N} ; equation 5-11) and buoyancy forces ($f_{1a,N}$; equation 5-14). If the total flow is horizontally oriented, $f_{1a,N}$ won't be considered either.

Thus, the streamwise momentum equation of a fully developed variable property EPG reference flow (VEPG henceforth) can be given as:

$$-\left(\frac{\partial P}{\partial z}\right)_p + \frac{1}{rRe_{\tau,0}} \frac{\partial}{\partial r} \left(r(\bar{\rho}\nu_{tp} + \bar{\mu}) \frac{\partial \tilde{u}_p}{\partial r} \right) = 0 \quad (5-21)$$

The driving force of this reference flow will still be given by equation 5-15. This is because the pseudo body forces f_{1b} and f_{1c} do not play a role in altering the driving force of the reference flow.

Finally, to completely define the VEPG reference flow, a few comments on the temperature and thus the $\bar{\rho}$ and $\bar{\mu}$ fields are necessary. The fundamental basis behind the proposition of a VEPG reference flow is the figure 4-16. Looking at the same, we can draw an analogy with the constant property EPG reference flow concept.

The proposal for using ARN theory is motivated by the collapse of eddy viscosity against y^{+1} , which is interpreted as the y^+ of the EPG reference flow. y^{+1} is calculated using the $\bar{\rho}$ and $\bar{\mu}$ at the centerline of the total flow (equation 5-18). This leads to the conclusion that the EPG reference flow is a constant property flow with $\bar{\rho} = \rho_c$ and $\bar{\mu} = \mu_c$.

Similarly, y^{*1} can be thought of as the y^* of the VEPG reference flow. In figure 4-16, y^{*1} was calculated using the locally averaged properties in the total flow (equation 4-6). On the basis of above mentioned, the \bar{T} , and thus the $\bar{\rho}$ and $\bar{\mu}$ of each VEPG reference flow must be identical to the \bar{T} , $\bar{\rho}$ and $\bar{\mu}$ of the total flow at that axial location.

Thus, the algorithm 2 can be modified as follows:

Algorithm 3 Modification of RANS solver using SLS and ARN theories

Require: $\left(\frac{\partial P}{\partial z}\right)_p = f(\tau_{wp})$

Initialize the flow field with periodic inflow.

Start iterating

if Residuals > Convergence criteria **then**

Obtain the fields for the EPG reference flows as follows:

Set $\mathbf{v}_p \leftarrow 0$.

Obtain \mathbf{u}_p (equation 5-21).

Set $\bar{\rho}_p = \bar{\rho}$, $\bar{\mu}_p = \bar{\mu}$ for each axial location.

Solve the turbulence model equations in the semi-locally scaled form [35] for the VEPG reference flows and obtain $\boldsymbol{\mu}_t$

Calculate $\boldsymbol{\alpha}_t$ from $\boldsymbol{\mu}_t$

Solve the mean energy equation (use $\boldsymbol{\alpha}_t$).

Solve the mean momentum equations (use $\boldsymbol{\mu}_t$).

end if

Results and Discussion

In this chapter, the results obtained from carrying out RANS simulations for Cases A and B will be reported and compared with the DNS data.

Most of the conventional turbulence models have been derived for and have had their modeling constants tuned to fully developed constant property turbulent flows. Thus, they do not take into account the effects resulting from strong property variation in spatially developing heated turbulent flows. As a result, their performance will differ depending on the case being simulated. Similarly, semi-locally scaled (SLS) turbulence models do not intrinsically take buoyancy and thermal acceleration effects into account.

The objective of this chapter is to assess whether by utilizing the Apparent Reynolds Number (ARN) theory and ARN + SLS theories (section 5-4), we can improve the performance of the conventional turbulence models. Thus, the purpose of the comments on the results is to shed light on whether the same is possible, and if not then to indicate the reason.

We will refer to the different implementations of the turbulence models based on their choice of scaled wall-normal distance. Thus, the conventional, SLS, ARN, and SLS+ARN implementations are referred to as y^+ , y^* , y^{+1} , and y^{*1} respectively. It is important to note that these implementations only differ in the way they calculate the eddy viscosity. We use a constant Pr_t to model eddy diffusivity (α_t) which makes the latter strongly dependent on the eddy viscosity. Hence, the differences in our thermal and flow fields are primarily arising from differences in eddy viscosity.

Also, turbulent heat flux is the dominant mode of heat transfer in the cases chosen. In the actual flow (DNS), radial and turbulent heat flux both contribute to the transport of heat. However, in the RANS model predictions, the axial turbulent heat flux could not be reproduced by any of the models. This is due to the use of the simple gradient diffusion hypothesis (SGDH) for modeling the turbulent heat flux. The use of SGDH makes the turbulent heat flux depend directly on the gradient of enthalpy. Since the axial enthalpy gradients are not large enough for our cases, this approach does not provide a good prediction of the axial turbulent heat flux. The models still provide a reasonable estimation of the temperature profile because they overestimate the radial turbulent heat flux compared to the DNS.

6-1 Case A

This case is heated supercritical developing turbulent flow in the horizontal direction. Thus, it is free from the effects of buoyancy but still laminarizes due to the effects of strong property variation.

6-1-1 MK turbulence model

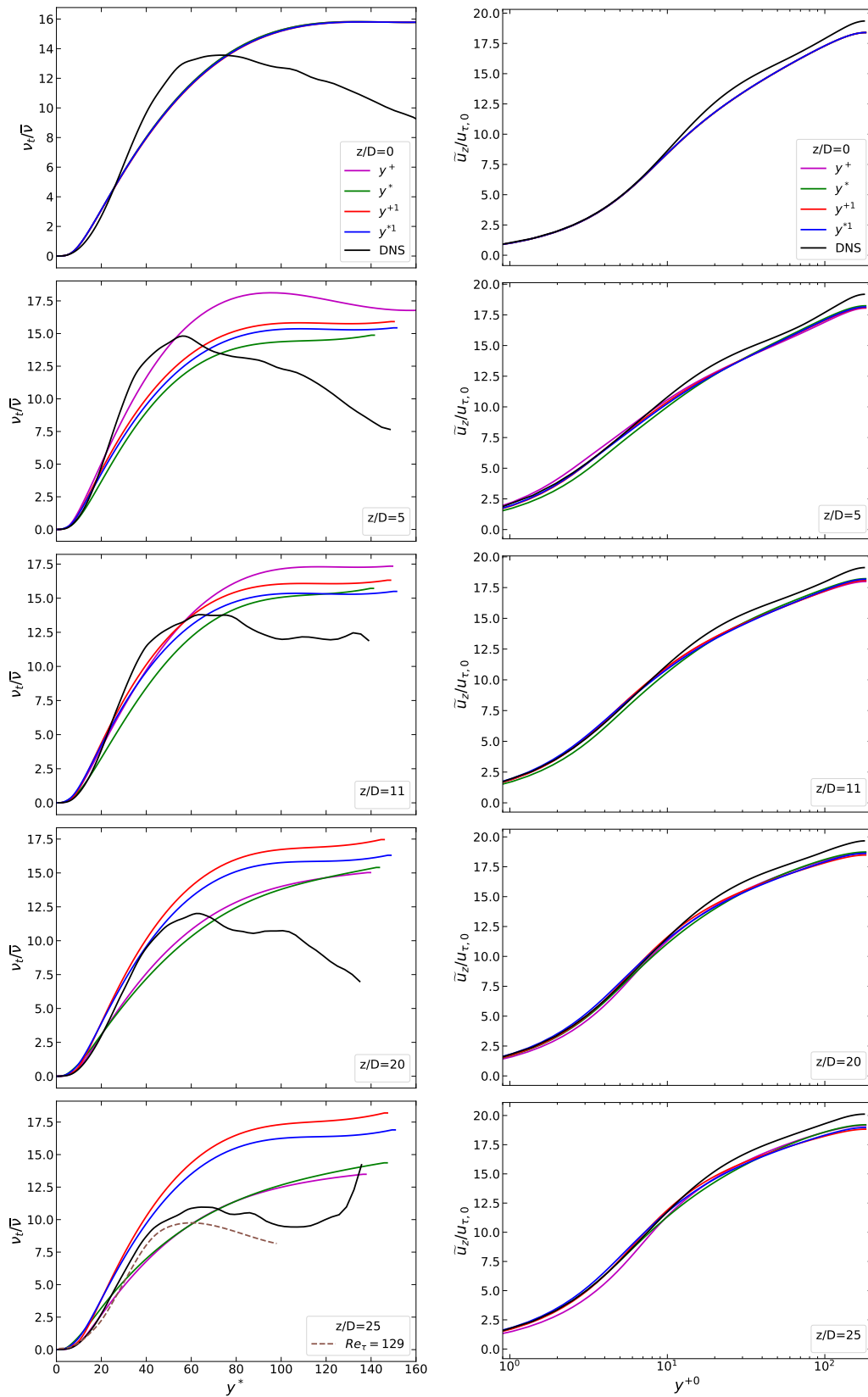


Figure 6-1: Eddy viscosity and streamwise velocity for various axial locations (Case A, MK). y^{+0} : scaled using parameters at $z/D = 0$

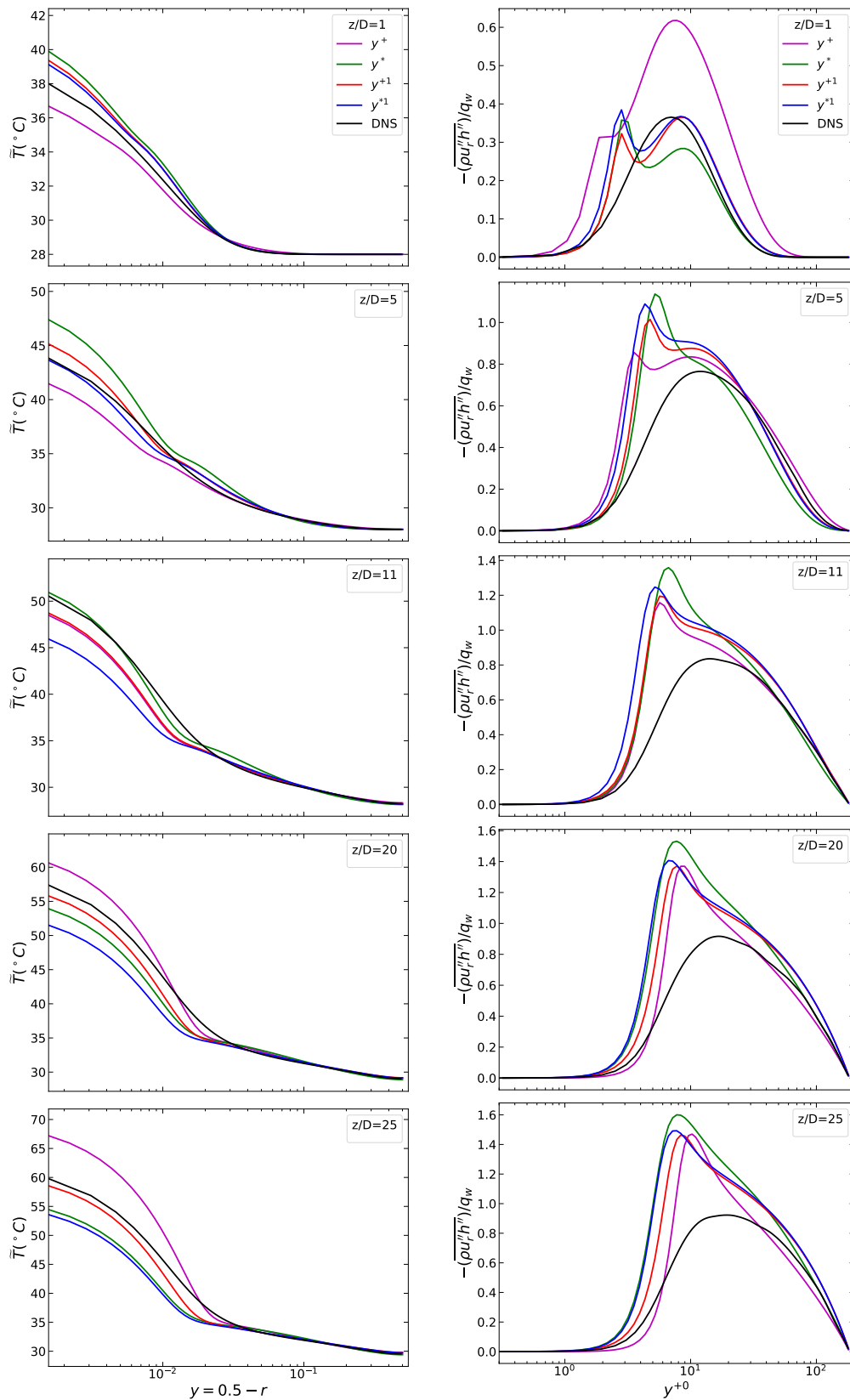


Figure 6-2: Radial temperature profile and Radial turbulent heat flux for various axial locations (Case A, MK).

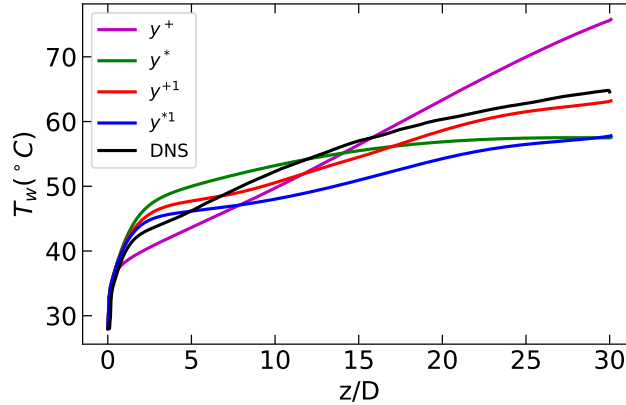


Figure 6-3: Wall temperature comparison (Case A, MK).

Eddy viscosity and velocity

From figure 6-1, y^+ implementation provides an overestimation of near-wall turbulence activity in the initial region ($z/D = 0$ to $z/D \approx 5$). For this discussion, the near-wall region corresponds to approximately $y^* \leq 25$. Upon moving downstream, it does a better job of predicting the reduction of turbulence in the near-wall region.

The y^* implementation is unable to predict the increase in near-wall turbulence activity in the initial region ($z/D = 0$ to $z/D \approx 5$). Upon moving downstream, it progressively provides an overestimation of eddy viscosity in the near-wall region. This is in spite of getting a good collapse of SLS turbulent shear stresses in the latter half of the domain. This is expected to be due to history effects i.e. the performance downstream is not independent of the performance upstream.

The y^{+1} and y^{*1} implementations display a very similar behavior near the wall. A good adherence to DNS data is observed in the initial region. Upon moving beyond a certain axial location ($z/D \approx 17$), y^{+1} and y^{*1} implementations show a visible shift compared to the DNS data. This is attributed to the Low-Reynolds number effects.

In the process of solving turbulence models using y^{+1} and y^{*1} theories, we are approximating the eddy viscosity at each axial location with the eddy viscosity of a fully developed flow. When the Apparent Reynolds Number of the same falls below a certain value, the turbulence models are unable to give a good prediction of the eddy viscosity. To substantiate this claim, the eddy viscosity of a fully developed constant property turbulent flow at $Re_\tau = 129$ (DNS) is provided in figure 6-1, from [28]. This is approximately the ARN corresponding to $z/D = 25$, and we can see that the eddy viscosity of $Re_\tau = 129$ flow adheres more closely to the DNS than the turbulence model prediction. Thus, as the Apparent Reynolds Number falls below a certain threshold, the turbulence model will not give a good prediction of eddy viscosity.

The velocity predictions of y^{+1} and y^{*1} implementations are relatively more robust than other implementations. However, none of the implementations are able to predict the streamwise velocity well. They show a lower log-law constant as compared to the DNS. This is attributed to the fact that the Reynolds number in the entire simulation domain is low.

Temperature

A constant $Pr_t = 0.9$ was utilized for modeling the thermal turbulence. From chapter 1, we know that turbulent heat flux is the primary mode of heat transfer for the chosen flows. Also, the effects of thermal advection do not differ considerably for the different implementations.

This is because their velocity predictions are not significantly different.

As discussed before, the use of SGDH does not provide a good prediction of axial turbulent heat flux due to the small value of axial enthalpy gradients. Thus, the thermal fields of all the implementations are primarily influenced by the radial turbulent heat flux. The differences in the radial temperature profiles of all implementations can be explained by looking at the near-wall values of radial turbulent heat flux. The turbulent heat flux in turn primarily depends on the prediction of eddy viscosity, as $\alpha_t = \nu_t/Pr_t$. As a result, the implementations with a higher value of near wall ν_t lead to a lower radial temperature distribution. This can be observed from figure 6-2. However, the trends of model predictions relative to DNS can not be explained by just looking at the radial turbulent heat flux. This is because axial turbulent heat flux is also important for some locations in the actual flow.

6-1-2 SA Turbulence model

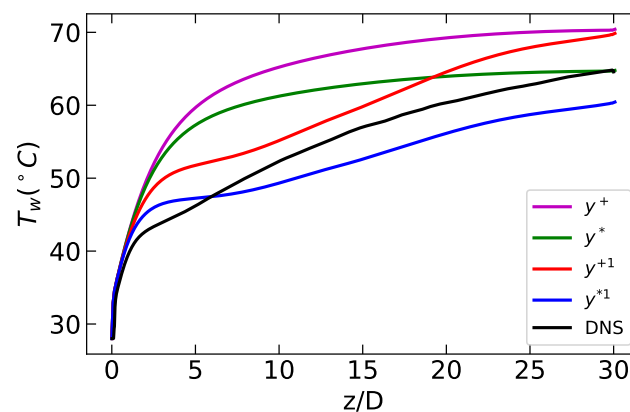


Figure 6-4: Wall temperature comparison (Case A, SA).

Eddy viscosity and velocity

From figure 6-5, both y^+ and y^* implementations display a very similar performance in the near wall and the core region. Between $z/D = 0$ to $z/D \approx 5$, they show a reduction in near-wall turbulence activity instead of an expected increase. For the locations further downstream, a better near-wall collapse is observed. The large difference between the near-wall eddy viscosities of y^+ and y^* implementations compared to DNS data is also reflected in the velocity profiles.

The y^{+1} and y^{*1} implementations provide good adherence to the DNS data for initial locations. As before, upon moving sufficiently downstream, a visible shift in eddy viscosity is observed compared to DNS. This is due to the low value of the Apparent Reynolds Number.

The velocity profiles obtained using the SA model do not show a lower log-law constant. This is an interesting observation, as it implies that SA model might be better suited for modeling low Reynolds number turbulent flows.

Temperature

The radial temperature profile trends for the different implementations remain almost the same throughout the simulation domain. The increase in near-wall eddy viscosity of y^* implementation around $z/D = 20$ causes the near-wall turbulent heat flux of y^* based implementation to increase, compared to y^{*1} (figure 6-6). This change is also reflected in the temperature profile.

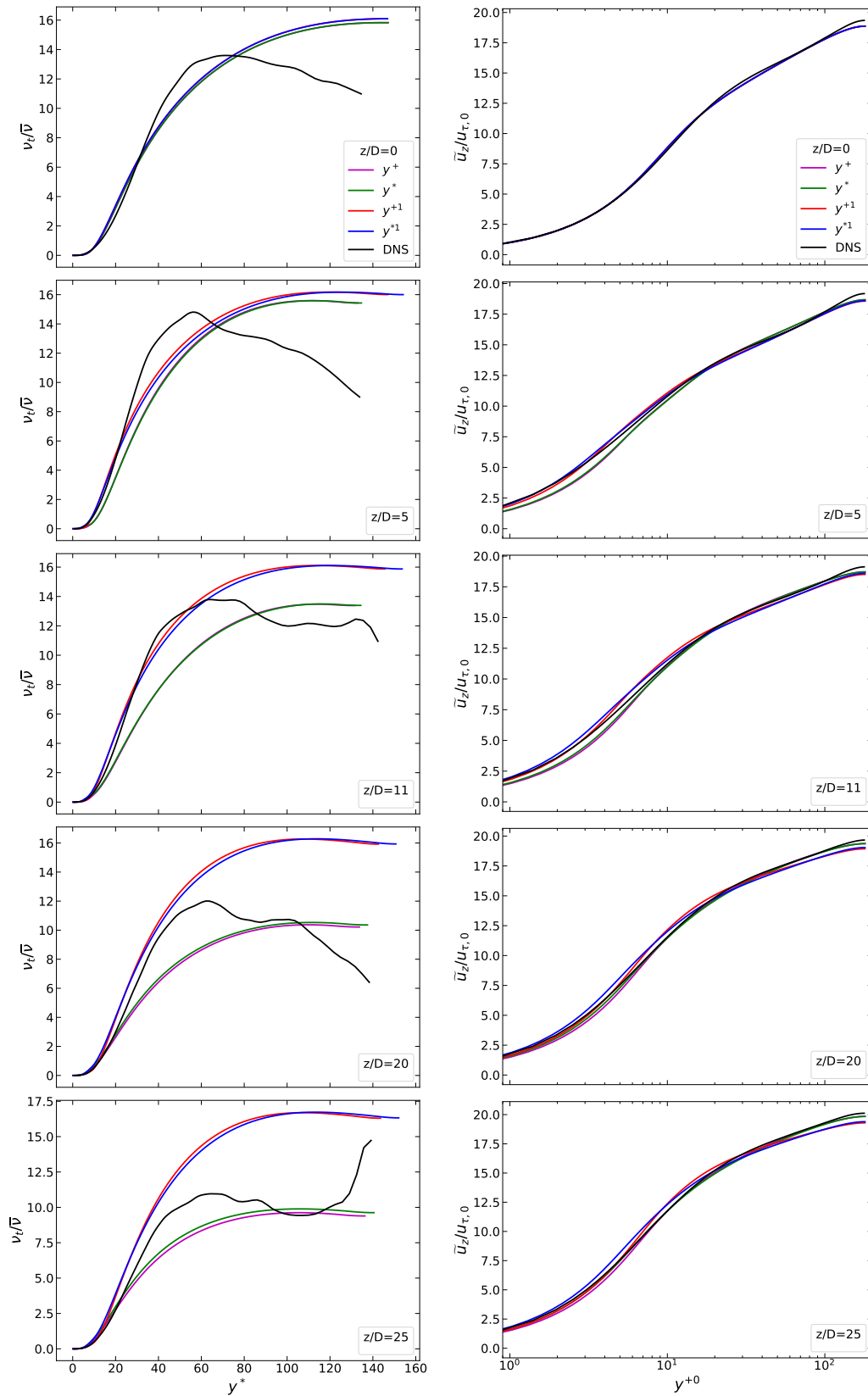


Figure 6-5: Eddy viscosity and streamwise velocity for various axial locations (Case A, SA).

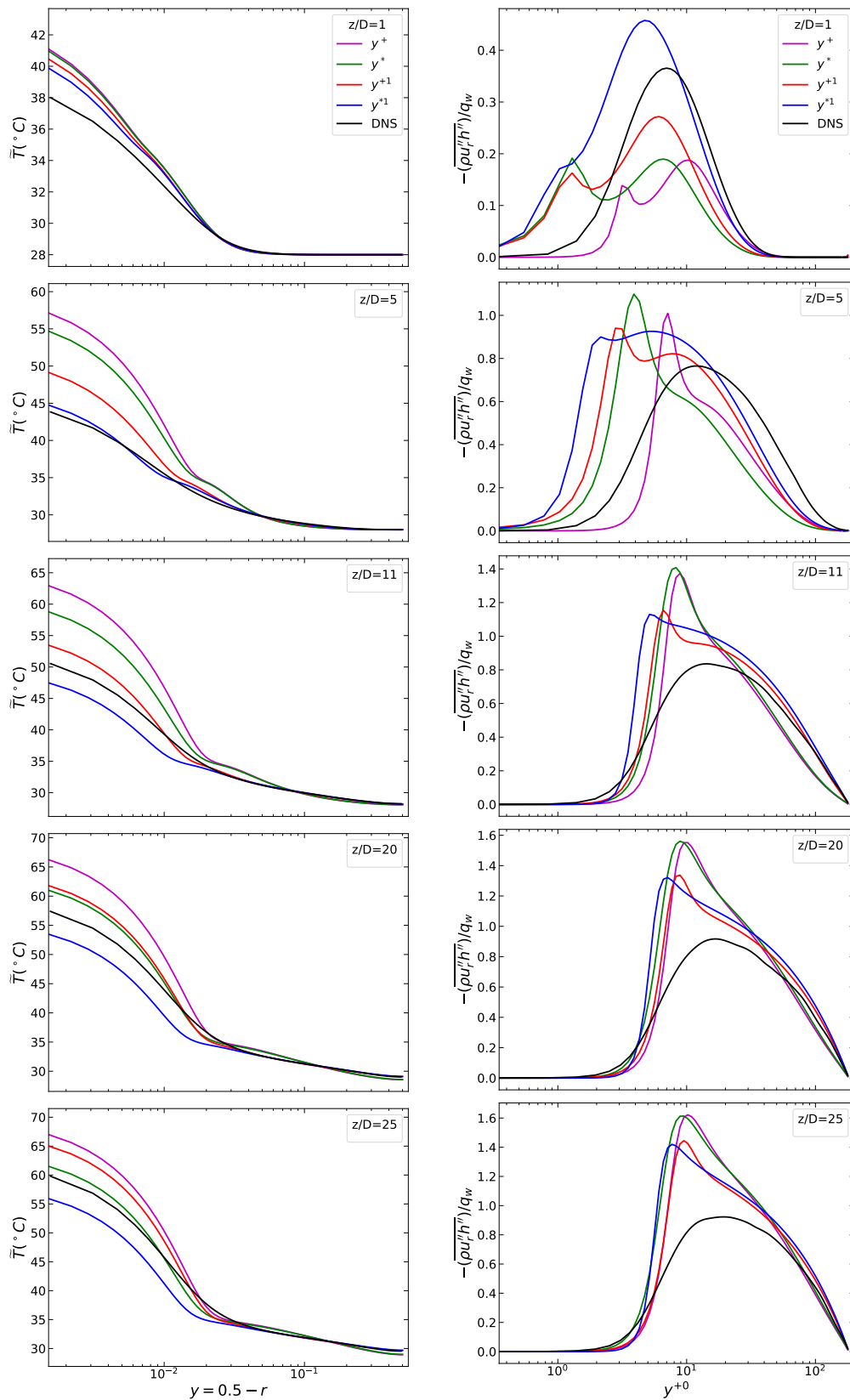


Figure 6-6: Radial temperature profile and Radial turbulent heat flux for various axial locations (Case A, SA).

6-1-3 $k - \omega$ SST turbulence model

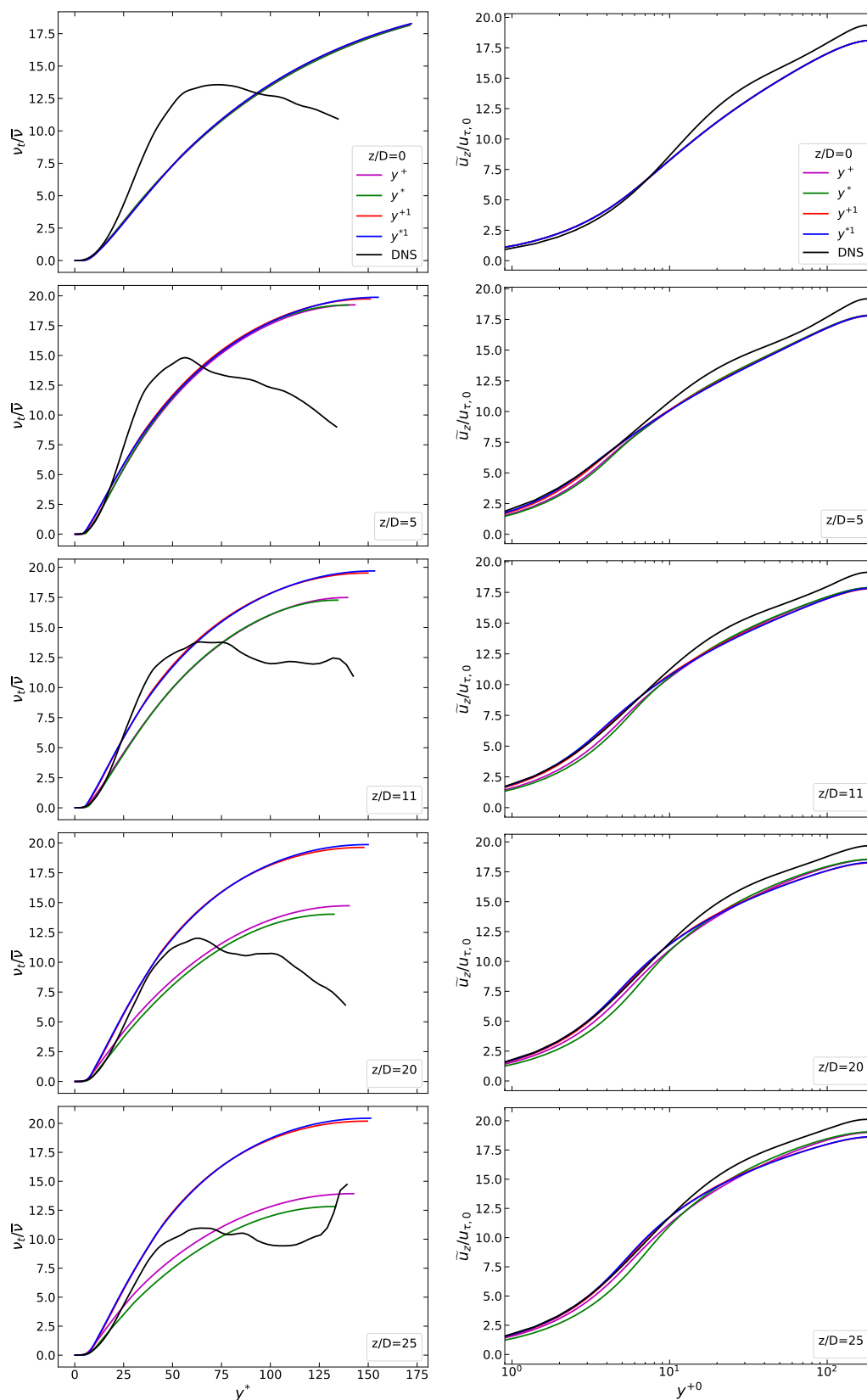


Figure 6-7: Eddy viscosity and streamwise velocity for various axial locations (Case A, SST).

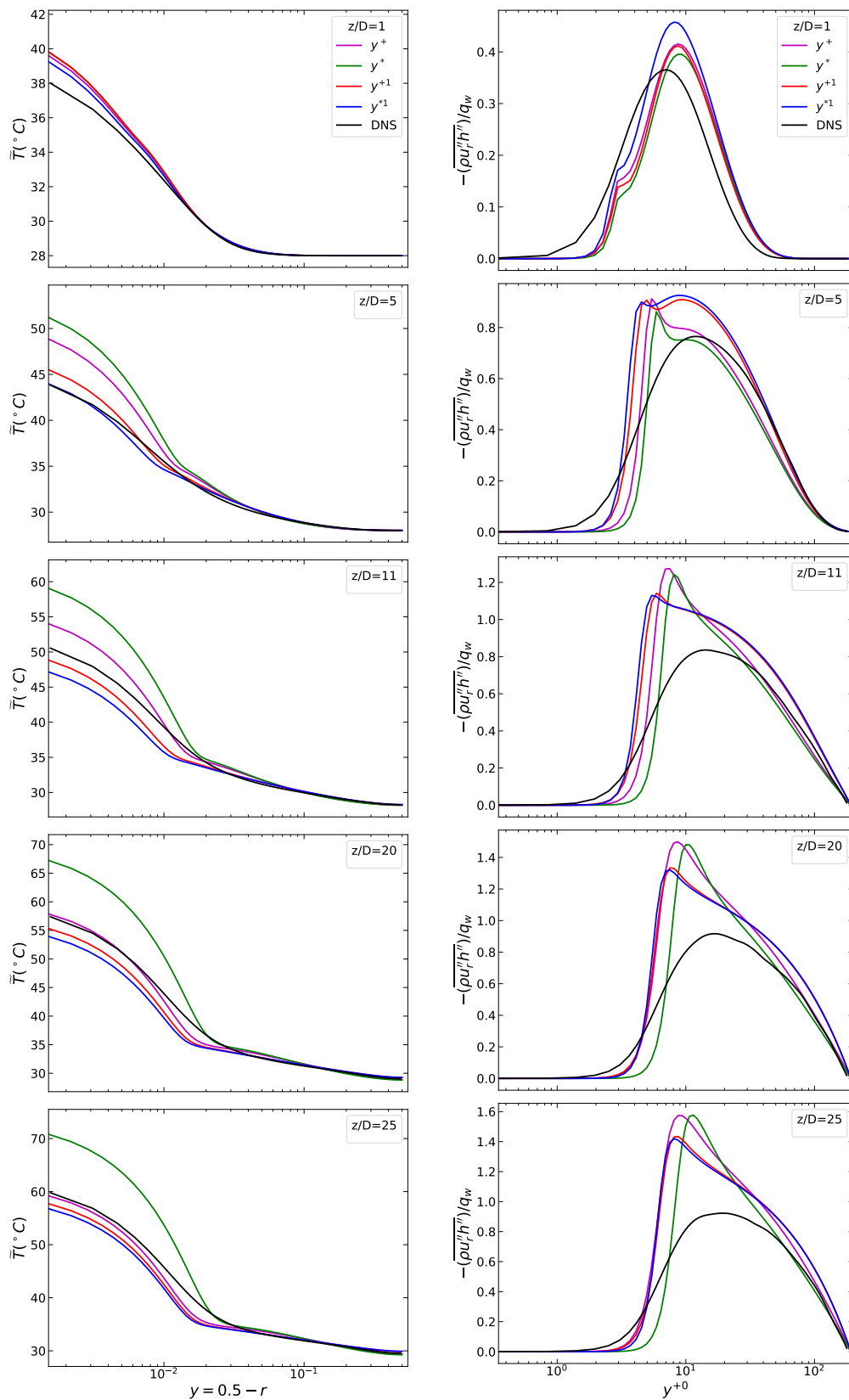


Figure 6-8: Radial temperature profile and Radial turbulent heat flux for various axial locations (Case A, SST).

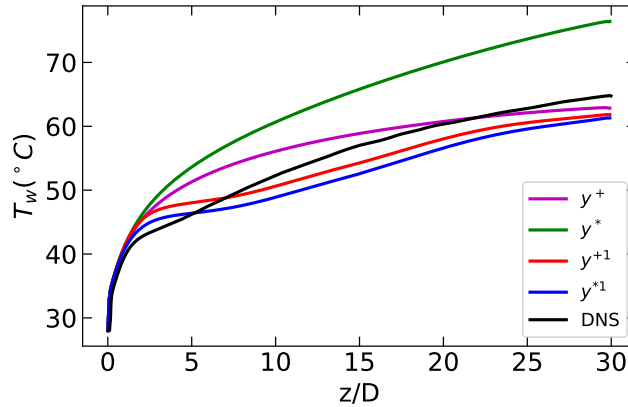


Figure 6-9: Wall temperature comparison (Case A, SST).

Eddy viscosity and velocity

The y^+ and y^* implementations display a very similar performance between $z/D = 0$ and $z/D \approx 11$. Both of them are able to predict the increase in the near wall turbulence between $z/D = 0$ and $z/D \approx 5$. Downstream of $z/D \approx 17$, the y^+ implementation overestimates the near wall eddy viscosity. However, y^* implementation either gives a similar or slightly lower near-wall eddy viscosity. Observations about velocity profiles are consistent with the observations of eddy viscosity.

As before, the performance of y^{+1} and y^{*1} implementations is good in the initial region and shows a visible shift for downstream locations. Thus, the predictions of y^{+1} and y^{*1} based implementations are pretty consistent, regardless of the turbulence models employed. To reiterate, y^{+1} and y^{*1} implementations approximate the eddy viscosity of each axial location with the eddy viscosity of a fully developed flow. The latter can be predicted well by most conventional turbulence models. Thus, this is a robust approach that can be used to sensitize conventional turbulence models to the effects of buoyancy and thermal acceleration.

Temperature

The trend of radial temperature for different implementations remains the same and can be predicted from the near-wall value of radial turbulent heat flux (figure 6-8). The y^* based implementation provides a very large overestimation of near-wall temperature as we move downstream. This is because the radial turbulent heat flux remains low in the near-wall region, as can be seen from figure 6-8. This is attributed to a relatively low near-wall eddy viscosity obtained using this implementation.

6-2 Case B

This case is a heated developing supercritical turbulent flow in the vertical direction. Thus, the strong property variation leads to an additional mechanism of buoyancy (subsection 1-1-2). This leads to a stronger laminarization of case B as compared to case A.

6-2-1 MK turbulence model

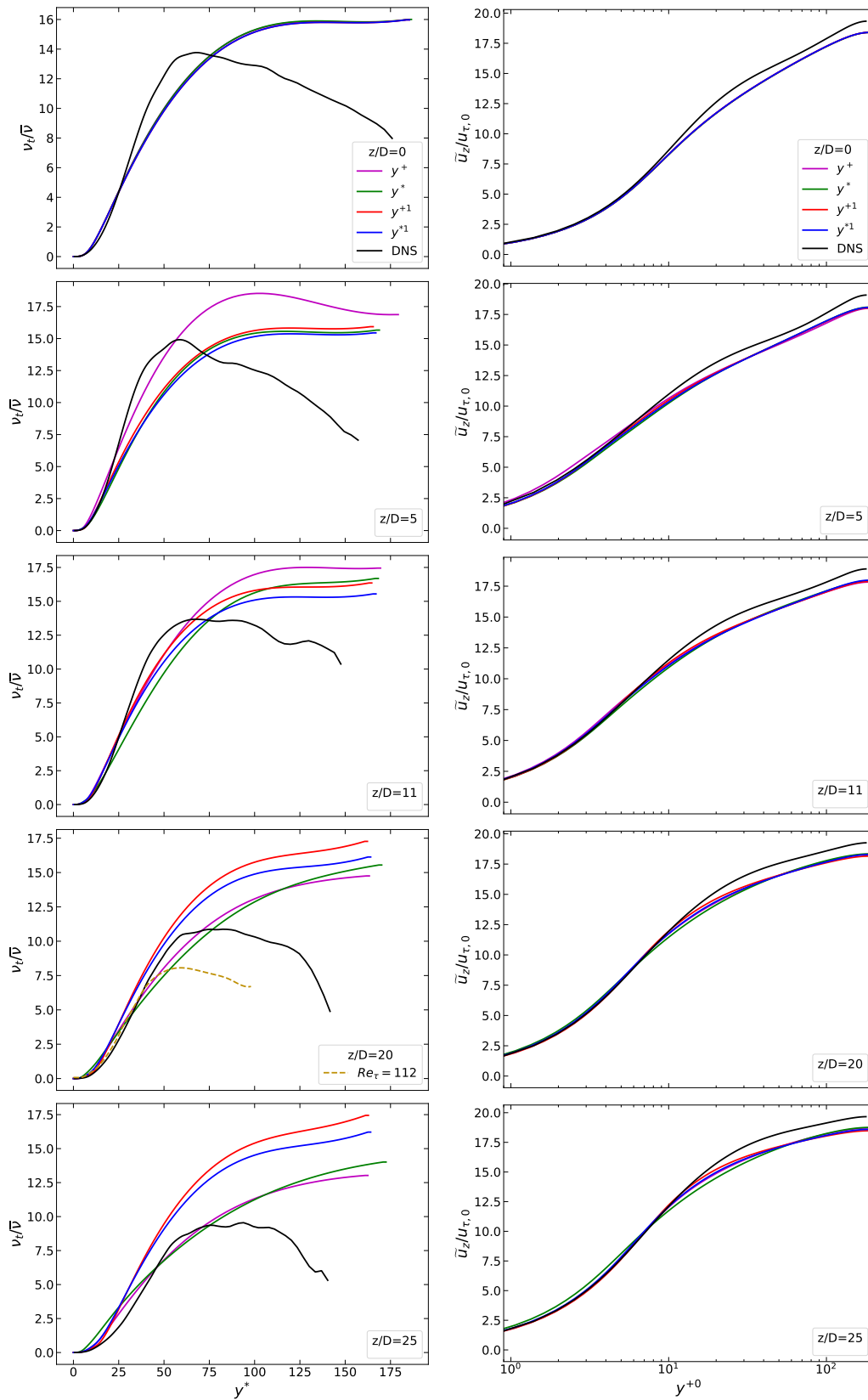


Figure 6-10: Eddy viscosity and streamwise velocity for various axial locations (Case B, MK).

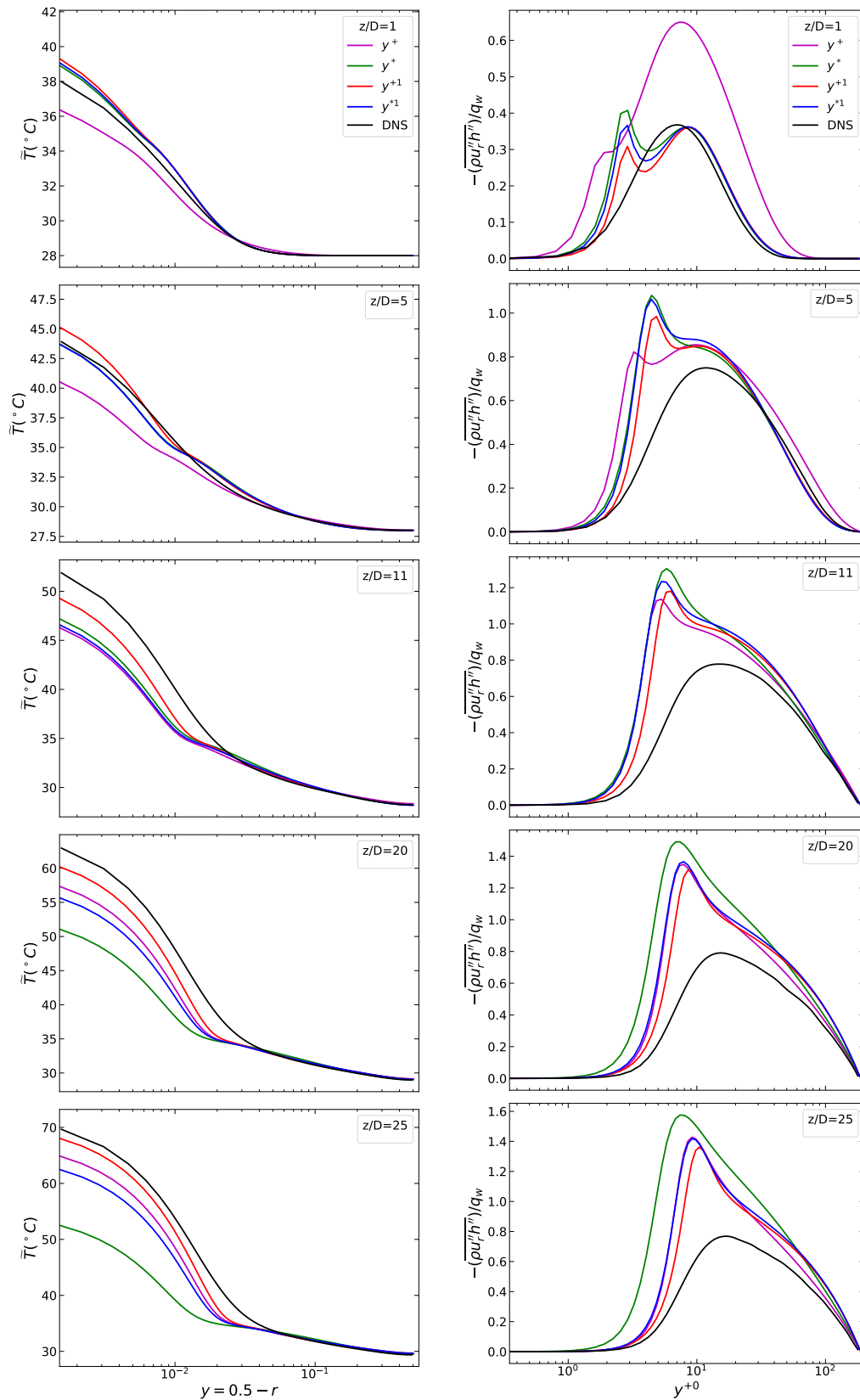


Figure 6-11: Radial temperature profile and Radial turbulent heat flux for various axial locations (Case B, MK).

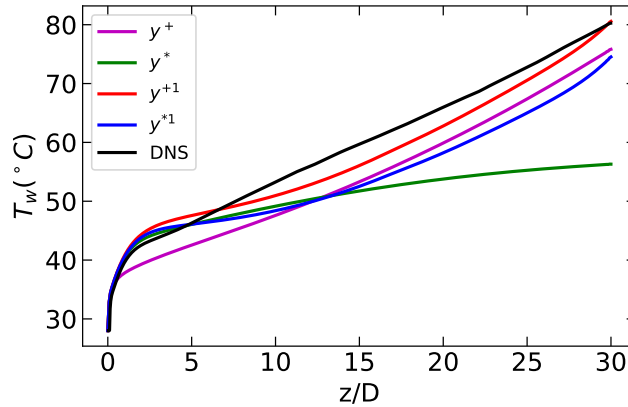


Figure 6-12: Wall temperature comparison (Case B, MK).

Eddy viscosity and velocity

Qualitatively, the performance of the different implementations for case B is similar to case A. Hence, only the observations that are different as compared to case A will be mentioned in the discussion henceforth.

The extent to which the y^* implementation overpredicts the near wall eddy viscosity increases in case B for downstream locations. The reason for the same can be explained as follows. We discussed in subsection 4-2-2, that case B has a considerable change in wall-normal Reynolds stress anisotropy even for downstream locations. It causes the Reynolds shear stresses (and thus eddy viscosity) to move away from the wall. This effect is not due to local property variation, and can not be characterized by semi-local scaling. This in combination with history effects leads to a strong overprediction of eddy viscosity in the near wall region by y^* implementation. This problem is exacerbated in the MK model due to the use and formulation of the damping function.

MK turbulence model uses a damping function depending upon the scaled wall-normal distance to predict the effects of viscous damping on turbulence. Due to it being strongly correlated with wall distance, it fails to provide a good prediction of the extent of the viscosity-dominated region.

As before, the y^{+1} and y^{*1} implementations start showing a visible shift compared to DNS for downstream locations. This is again due to Low Reynolds Number effects. To back this claim, we have provided the eddy viscosity of a fully developed turbulent flow corresponding to the ARN of $z/D = 20$ in figure 6-10. As the effects of laminarization are stronger for case B, the Apparent Reynolds Number for downstream locations is lower than for case A. This leads to a greater discrepancy between DNS and y^{+1}/y^{*1} results.

6-2-2 SA turbulence model

Eddy viscosity and velocity

From figure 6-13, for $z/D = 0$ to $z/D \approx 11$, it can be seen that y^+ and y^* implementations provide a strong underprediction of eddy viscosity throughout the radial domain. Upon moving downstream, the reduction becomes more prominent in the core region. This is due to a strong reduction in the production of turbulence.

In the SA model, the production of turbulence strongly depends on the absolute value of vorticity. Case B has the presence of buoyancy force which causes a stronger near-wall acceleration

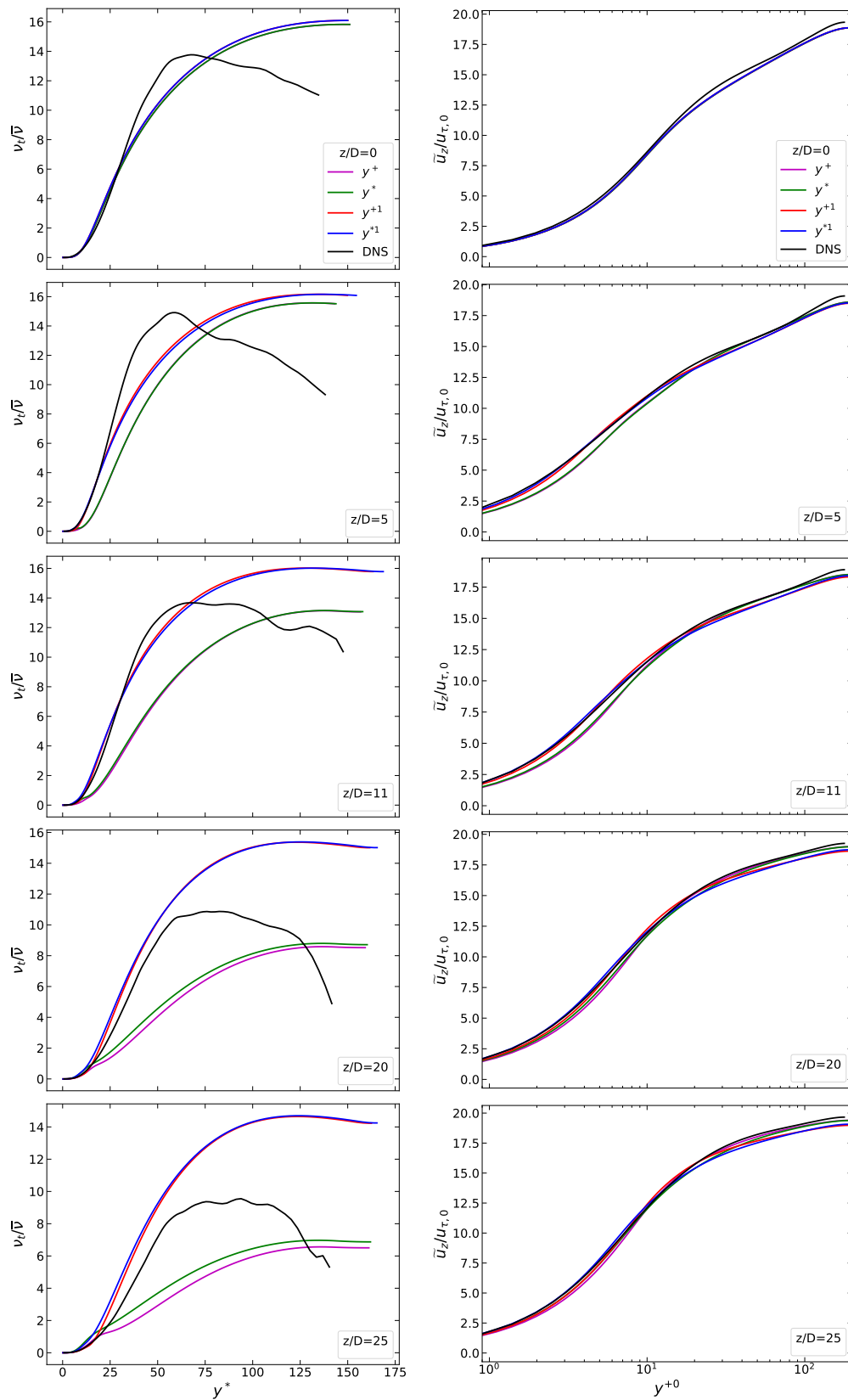


Figure 6-13: Eddy viscosity and streamwise velocity for various axial locations (Case B, SA).

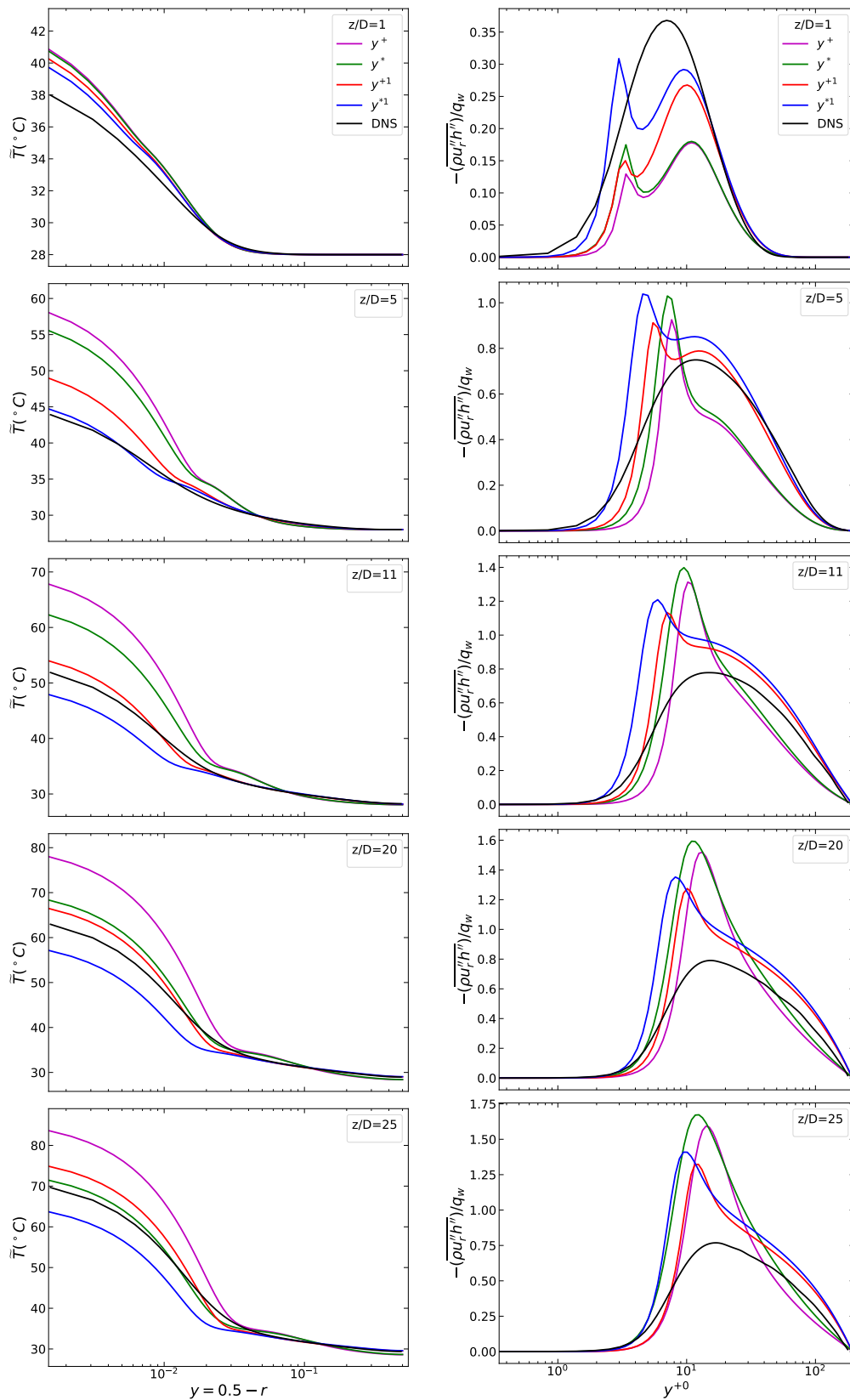


Figure 6-14: Radial temperature profile and Radial turbulent heat flux for various axial locations (Case B, SA).

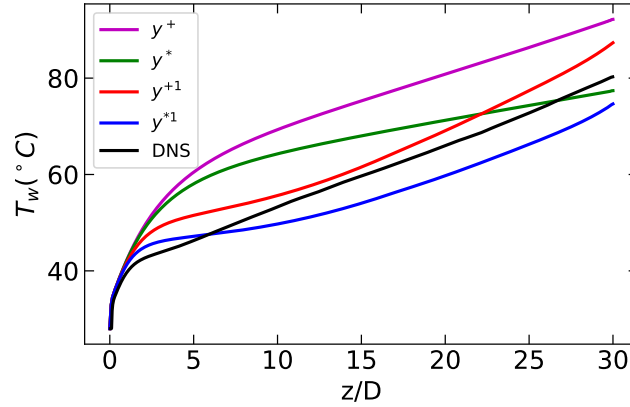


Figure 6-15: Wall temperature comparison (Case B, SA).

and core deceleration than case A. The deceleration in the core causes a strong reduction in the value of vorticity and thus the production in the core region.

The y^{+1} and y^{*1} implementations do not suffer from this issue. This is because, for both of them, we solve turbulence model equations for EPG reference flows. These flows are fully developed flows. They do not feel the influence of acceleration directly, but indirectly through their ARN.

The inability of y^{+} and y^{*} based implementations to get a good prediction of eddy viscosity also reflects in the streamwise velocity profiles.

6-2-3 $k - \omega$ SST turbulence model

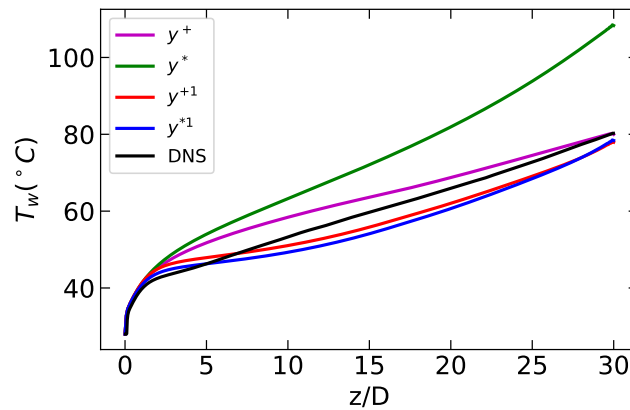


Figure 6-16: Wall temperature comparison (Case B, SST).

Eddy viscosity and velocity

From figure 6-18, y^{+} implementation provides relatively satisfactory near-wall eddy viscosity throughout the domain. The y^{*} based implementation, however, provides a severe underprediction of eddy viscosity in the near-wall region as we move downstream. This has strong repercussions on the velocity and temperature predictions of the y^{*} implementation.

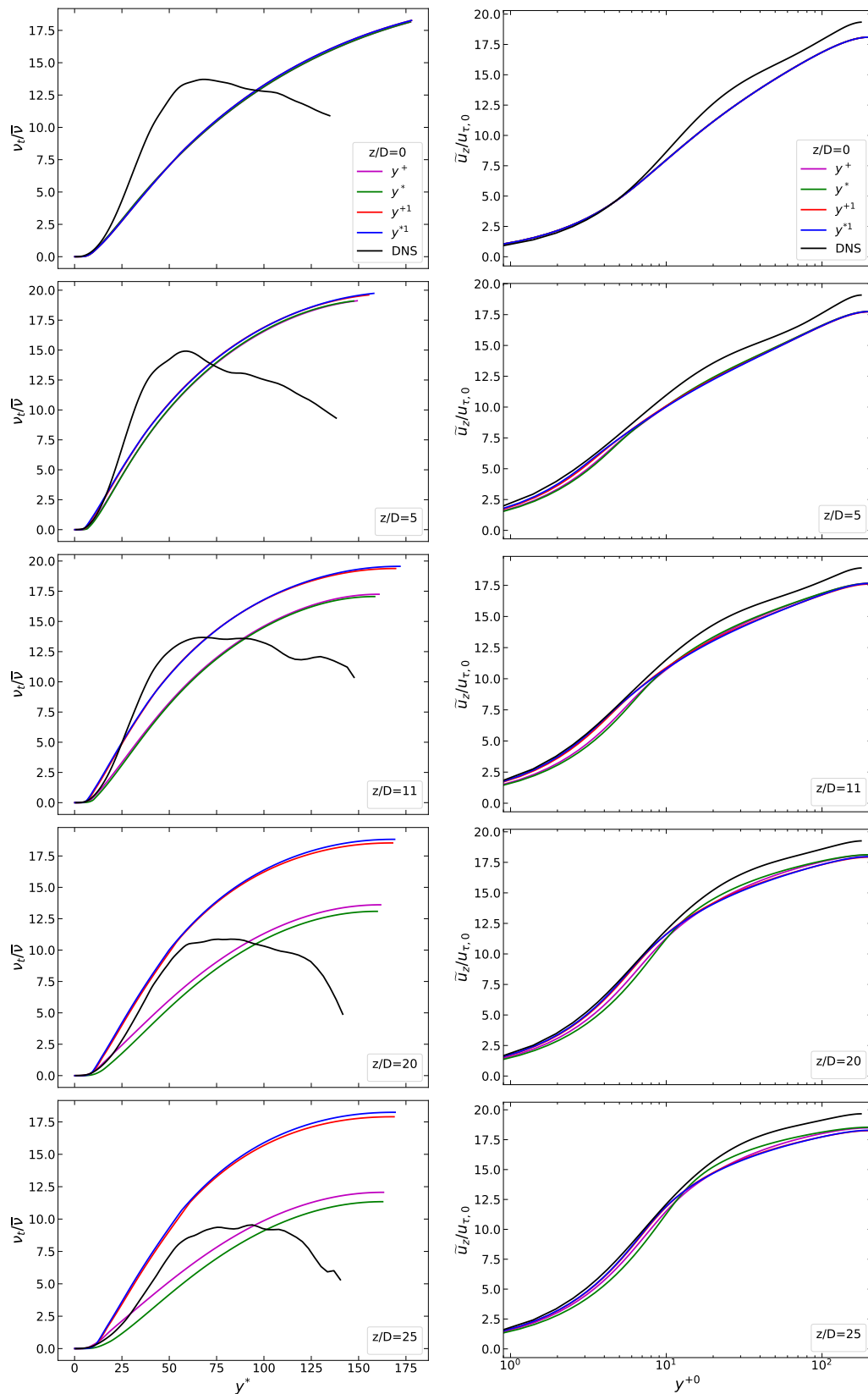


Figure 6-17: Eddy viscosity and streamwise velocity for various axial locations (Case B, SST).

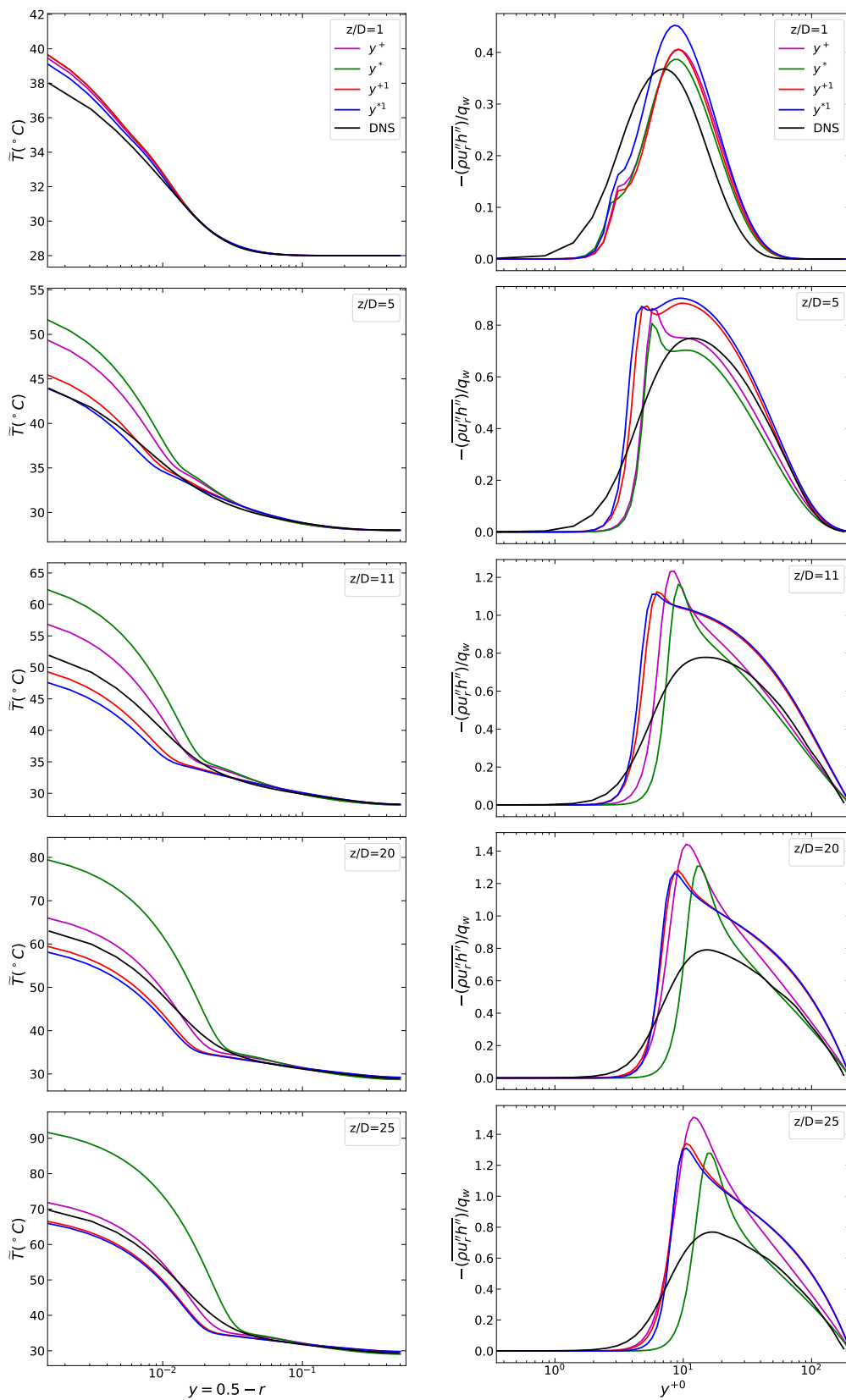


Figure 6-18: Radial temperature profile and Radial turbulent heat flux for various axial locations (Case B, SST).

Temperature

Due to the low near-wall eddy viscosity obtained by the y^* implementation, the radial turbulent heat flux also remains low for the same near the wall. As a result, we get a strong overprediction of the radial temperature profile using the y^* implementation. As before, the trend of radial temperature distribution for the different implementations remains consistent with the near-wall radial turbulent heat flux.

Summary and Conclusions

The present work aimed at improving the modeling techniques for developing heated supercritical turbulent flows. The strong variation of thermophysical properties at supercritical pressure and complex flow physics resulting from it makes this task challenging. The conventional approach for improving model predictions involves proposing new closure techniques or modifying pre-existing closure techniques. We tried an alternative approach, making use of Semi-Local scaling (SLS) and Apparent Reynolds Number (ARN) theories.

Two cases from the Ph.D. thesis of Dr. Hassan Nematı [1] were chosen to be analyzed and simulated in this work. Both are heated developing supercritical turbulent flows with SCO₂ as the working fluid. Both cases experience near-wall acceleration and the consequent core deceleration due to property variation. Cases A and B are horizontally and vertically oriented respectively. Thus, Case B has the additional effect of buoyancy, which makes the acceleration/deceleration in the near-wall/core regions stronger. Both cases were chosen such that ‘full laminarization’ does not occur in the simulation domain. This is crucial for ARN theory to be valid throughout the domain.

In the initial part of the domain, the near-wall acceleration causes an increase in the production of streamwise Reynolds stresses near the wall. The pressure-strain correlation also increases in the near-wall region, which in turn increases the spanwise and wall-normal Reynolds stresses near the wall. The latter coupled with the increase in the slope increases the near-wall value of Reynolds shear stresses. The strength of this effect is comparable for both cases.

Upon moving sufficiently downstream, a considerable reduction in the slope of streamwise velocity is obtained near the core. As a result, the leading order production terms of streamwise Reynolds stresses and Reynolds shear stresses decrease in the core region. Naturally, the pressure-strain correlation also decreases in the core region. Thus, a reduction of Reynolds normal and shear stresses is obtained in the core region upon moving downstream. This effect is stronger for case B compared to case A. The decrease in turbulence production in the core region is stronger than the increase obtained in the near-wall region. This leads to an overall reduction in turbulence downstream, also known as ‘laminarization’.

SLS cannot characterize the changes in Reynolds shear stresses in the initial region for either case. This is attributed to the strong changes in wall-normal Reynolds stress anisotropy, as explained in chapter 4. For case A, upon moving downstream, a region of ‘thermal equilibrium’ is obtained. This is the region where the semi-locally scaled turbulent structures can be considered self-similar. As a result, we get a good collapse of SLS Reynolds shear stresses in that region. However the same can not be said about case B. This is attributed to the fact that the wall-normal Reynolds stress anisotropy shows considerable evolution even for downstream locations. Investigating the reason for this is a topic that could be pursued in the future.

ARN theory proposes the usage of ‘linear part of stresses’ instead of wall shear stress to define the wall-scaled distance. This choice drastically improves the collapse of Reynolds stresses and Eddy viscosity. This modified scaling approach helps deal with the effects that conventional and semi-local scales fail at.

A methodology was proposed in order to use ARN theory by itself, and in combination with SLS for RANS in chapter 5. The results obtained using this methodology were compared with the performance of conventional and SLS turbulence models. Three commonly used turbulence models were chosen for this purpose: Myong Kasagi (MK) [19], Menter’s $k - \omega$ SST [31], and Spalart Allmaras (SA) [32].

The conventional and SLS implementations of these models do not give excellent results in either case. They have not been sensitized to the previously mentioned effects that arise when supercritical turbulent flows are strongly heated and allowed to develop spatially. Their performance is case-specific, depending on the formulation of their transport equations and damping functions. The primary discrepancy in their results is observed in the near-wall eddy viscosity.

We used a constant $Pr_t = 0.9$ to model the thermal turbulence. The radial turbulent heat flux is the main mode of heat transfer in the modeled flows. It depends very strongly on the near-wall value of eddy viscosity due to the use of a constant Pr_t . As a result, the inability of the conventional and SLS turbulence models to correctly predict the near-wall eddy viscosity is reflected also in the temperature profile. This inadvertently affects the predictions of turbulence and mean momentum, as the fields are strongly coupled.

The ARN and ARN+SLS-based implementations of the models provide a relatively good prediction of turbulence in the initial region. They are not as sensitive to the choice of turbulence model and provide pretty consistent results across different models. However, upon moving downstream, the prediction accuracy progressively worsens. This is due to Low Reynolds Number effects. In using ARN theory, we estimate the eddy viscosity of each axial location with the eddy viscosity of a fully developed turbulent flow. The Reynolds number of the latter is known as ARN, and it reduces as we move downstream. Upon reduction below a certain value, the RANS models become incapable of giving a good prediction of the eddy viscosity. This effect is stronger for case B, as the ARN reduces more strongly for that case.

The use of a constant Pr_t makes the results very sensitive to the near-wall eddy viscosity value. Hence, the use of more complicated techniques for modeling the thermal turbulence is proposed for future extensions of this work. This could involve making use of Algebraic models for calculating Pr_t or solving additional transport equations for enthalpy variance and its dissipation to model α_t .

Appendix A

A-1 Experiments, Turbulence models and Working Fluids for the numerical studies

Numerical Study	Experimental study	Turbulence Models	Fluid
S. He et al. (2004) [14]	Weinberg [40]	LS [15], CH [16], LB [17], AKN [22], MK [19], k- ω [18]	SCO2
S. He et al. (2005) [12]	Jiang et al. [41]	LS [15]	SCO2
S. He et al. (2008a) [20]	Bae et al. (DNS) [26]	LS [15], YS [21], AKN [22], CH [16], MK [19], V2F [23]	SCO2
S. He et al. (2008b) [13]	Fewster et al. [42]	AKN [22], V2F [23]	SCO2
Pucciarelli et al. [25]	Watts [43], Jackson [44]	AKN [45], Deng [46], Zhang [47]	SCO2
Zhao et al. [24]	Li et al. [48]	LS [15], MK [19], AKN [22]	SCO2

Table A-1: Details of numerical experiments from the surveyed literature.

Appendix B

B-1 Modeled turbulent transport equations

B-1-1 Myong-Kasagi turbulence model

The modeled **TKE** equation is given as:

$$\frac{\partial \bar{\rho} \tilde{k}}{\partial t} + \frac{1}{r} \frac{\partial r \bar{\rho} \tilde{k} \tilde{u}_r}{\partial r} + \frac{\partial \bar{\rho} \tilde{k} \tilde{u}_z}{\partial z} = \frac{1}{r} \frac{\partial}{\partial r} \left(r \left(\frac{\bar{\mu}}{Re_{\tau,0}} + \frac{\mu_t}{\sigma_k} \right) \frac{\partial \tilde{k}}{\partial r} \right) + \frac{\partial}{\partial z} \left(\left(\frac{\bar{\mu}}{Re_{\tau,0}} + \frac{\mu_t}{\sigma_k} \right) \frac{\partial \tilde{k}}{\partial z} \right) + P_k + G_k - \bar{\rho}(\tilde{\epsilon}). \quad (\text{B-1})$$

The **TKE dissipation** is modeled in a similar fashion to the TKE equation, as follows:

$$\frac{\partial \bar{\rho} \tilde{\epsilon}}{\partial t} + \frac{1}{r} \frac{\partial r \bar{\rho} \tilde{\epsilon} \tilde{u}_r}{\partial r} + \frac{\partial \bar{\rho} \tilde{\epsilon} \tilde{u}_z}{\partial z} = \frac{1}{r} \frac{\partial}{\partial r} \left(r \left(\frac{\bar{\mu}}{Re_{\tau,0}} + \frac{\mu_t}{\sigma_\epsilon} \right) \frac{\partial \tilde{\epsilon}}{\partial r} \right) + \frac{\partial}{\partial z} \left(\left(\frac{\bar{\mu}}{Re_{\tau,0}} + \frac{\mu_t}{\sigma_\epsilon} \right) \frac{\partial \tilde{\epsilon}}{\partial z} \right) + C_{\epsilon 1} P_k \frac{\tilde{\epsilon}}{\tilde{k}} + C_{\epsilon 1} G_k \frac{\tilde{\epsilon}}{\tilde{k}} - C_{\epsilon 2} f_\epsilon \frac{\bar{\rho} \tilde{\epsilon}^2}{\tilde{k}}. \quad (\text{B-2})$$

Eddy viscosity can be obtained as:

$$\mu_t = \bar{\rho} C_\mu f_\mu \tilde{k}^2 / \tilde{\epsilon}. \quad (\text{B-3})$$

The model **constants** and **functions** are as follows:

$C_{\epsilon 1} = 1.4$, $C_{\epsilon 2} = 1.8$, $C_\mu = 1.4$, $\sigma_k = 1.4$, and $\sigma_\epsilon = 1.3$.

$$f_\mu = \left(1 - e^{(-y^+/70)} \right) \left(1 + 3.45 / \sqrt{Re_t} \right), \quad (\text{B-4})$$

$$f_\epsilon = \left(1 - (2/9) e^{-(Re_t/6)^2} \right) \left(1 - e^{(-y^+/5)} \right)^2. \quad (\text{B-5})$$

where, $Re_t = \bar{\rho} \tilde{k}^2 / \bar{\mu} \tilde{\epsilon}$.

Boundary conditions for scalars:

$$\tilde{k}_w = 0, \text{ and } \tilde{\epsilon}_w = (\mu_w / \rho_w) \left(\partial^2 \tilde{k} / \partial r^2 \right) \Big|_w \approx (2\mu_w k_1) / (\rho_w y_w^2).$$

B-1-2 Menter's $k - \omega$ SST turbulence model

The TKE equation of $k - \omega$ SST model remains similar to equation B-1, with the exception of dissipation and production term. P_k and $\bar{\rho}\tilde{\epsilon}$ are replaced with P_k^{lim} and $\beta^*\bar{\rho}\tilde{k}\tilde{\omega}$. $\tilde{\omega}$ is the specific dissipation rate and P_k^{lim} is defined as:

$$P_k^{\text{lim}} = \min(P_k, 20\beta^*\bar{\rho}\tilde{k}\tilde{\omega}). \quad (\text{B-6})$$

The specific **TKE dissipation** rate equation is modeled as follows:

$$\begin{aligned} \frac{\partial \bar{\rho}\tilde{\omega}}{\partial t} + \frac{1}{r} \frac{\partial r \bar{\rho}\tilde{\omega}\tilde{u}_r}{\partial r} + \frac{\partial \bar{\rho}\tilde{\omega}\tilde{u}_z}{\partial z} = \frac{1}{r} \frac{\partial}{\partial r} \left(r \left(\frac{\bar{\mu}}{Re_{\tau,0}} + \mu_t \sigma_\omega \right) \frac{\partial \tilde{\omega}}{\partial r} \right) + \frac{\partial}{\partial z} \left(\left(\frac{\bar{\mu}}{Re_{\tau,0}} + \mu_t \sigma_\omega \right) \frac{\partial \tilde{\omega}}{\partial z} \right) + \\ \underbrace{(1 - f_1) \frac{2\bar{\rho}\sigma_\omega}{\tilde{\omega}} \left(\frac{\partial \tilde{k}}{\partial z} \frac{\partial \tilde{\omega}}{\partial z} + \frac{\partial \tilde{k}}{\partial r} \frac{\partial \tilde{\omega}}{\partial r} \right)}_{CD_{k\omega}} + \frac{\alpha \bar{\rho}}{\mu_t} P_k + \frac{\alpha \bar{\rho}}{\mu_t} G_k - \beta \bar{\rho} \tilde{\omega}^2. \end{aligned} \quad (\text{B-7})$$

Eddy viscosity can be obtained as:

$$\mu_t = \frac{\bar{\rho} C_\mu \tilde{k}}{\max(C_\mu \tilde{\omega}, \Omega f_2)} \quad (\text{B-8})$$

For $k - \omega$ SST transport equations, β^* , σ_k , σ_ω , $\sigma_{\omega 2}$, α , β and C_μ are **modeling constants**. Ω represents absolute value of **vorticity**, and f_1 , and f_2 are **blending functions**. The blending functions are utilized to ensure a smooth transition from $k - \omega$ formulation near the wall to $k - \epsilon$ formulation in the free stream.

If ϕ_1 and ϕ_2 represent constants in $k - \omega$ and $k - \epsilon$ formulations respectively, the **effective constant** ϕ is given as:

$$\phi = f_1 \phi_1 + (1 - f_1) \phi_2 \quad (\text{B-9})$$

The aforementioned **model constants** and **blending functions** are:

$$\beta^* = 0.09, C_\mu = 0.31, \beta_1 = 0.075, \beta_2 = 0.0828, \sigma_{k1} = 0.85, \sigma_{k2} = 0.5, \sigma_{\omega 1} = 1, \sigma_{\omega 2} = 0.856, \\ \alpha_1 = \beta_1/\beta^* - \sigma_{\omega 1} \kappa^2/\sqrt{\beta^*}, \alpha_2 = \beta_2/\beta^* - \sigma_{\omega 2} \kappa^2/\sqrt{\beta^*}.$$

$$f_1 = \tanh((\min(\max(\gamma_1, \gamma_2), \gamma_3))^4), \quad (\text{B-10})$$

$$f_2 = \tanh((\max(2\gamma_1, \gamma_2))^2), \quad (\text{B-11})$$

where, $\gamma_1 = \sqrt{k}/(\beta^* \omega y)$, $\gamma_2 = 500\bar{\mu}/(\bar{\rho} y_w^2 \tilde{\omega})$, $\gamma_3 = 4\bar{\rho} \sigma_{\omega 2} k/(y_w^2 \cdot \max(CD_{k\omega}, 10^{-20}))$.

Boundary conditions for scalars:

$$\tilde{k}_w = 0, \text{ and } \tilde{\omega}_w = 60\mu_w/\rho_w \beta_1 y_w^2.$$

For the MK and SST models, the shear production term of the TKE equation (P_k) can be modeled as follows:

$$P_k = \mu_t \left(2 \left(\left(\frac{\partial \tilde{u}_r}{\partial r} \right)^2 + \left(\frac{\partial \tilde{u}_z}{\partial z} \right)^2 + \left(\frac{\tilde{u}_r}{r} \right)^2 \right) + \left(\frac{\partial \tilde{u}_z}{\partial r} + \frac{\partial \tilde{u}_r}{\partial z} \right)^2 \right) - \frac{2}{3} (\bar{\rho} \tilde{k} + \mu_t \nabla \cdot \tilde{u}) \nabla \cdot \tilde{u}. \quad (\text{B-12})$$

B-1-3 Spalart-Allmaras turbulence model

This turbulence model solves a transport equation for a scalar $\check{\nu}$, from which μ_t can be calculated. The transport equation can be written as:

$$\begin{aligned} \frac{\partial \check{\nu}}{\partial t} + \frac{1}{r} \frac{\partial r \check{\nu} \tilde{u}_r}{\partial r} + \frac{\partial \check{\nu} \tilde{u}_z}{\partial z} = \frac{1}{c_{b3}} \frac{1}{r} \frac{\partial}{\partial r} \left(r \left(\frac{\bar{\nu}}{Re_{\tau,0}} + \check{\nu} \right) \frac{\partial \check{\nu}}{\partial r} \right) + \frac{1}{c_{b3}} \frac{\partial}{\partial z} \left(\left(\frac{\bar{\nu}}{Re_{\tau,0}} + \check{\nu} \right) \frac{\partial \check{\nu}}{\partial z} \right) + \\ \frac{c_{b2}}{c_{b3}} \left(\left(\frac{\partial \check{\nu}}{\partial z} \right)^2 + \left(\frac{\partial \check{\nu}}{\partial r} \right)^2 \right) + c_{b1} \check{S} \check{\nu} - c_{w1} f_w \left(\frac{\check{\nu}}{d} \right)^2, \end{aligned} \quad (\text{B-13})$$

where,

$$\check{S} = \Omega + \frac{\check{\nu}}{\kappa^2 d^2} f_{v2}. \quad (\text{B-14})$$

The **eddy viscosity** can be obtained as:

$$\mu_t = \bar{\rho} \check{\nu} f_{v1}. \quad (\text{B-15})$$

From equations B-13-B-15, c_{b1} , c_{b2} , c_{b3} , c_{w1} , c_{w2} , and κ are **model constants**, Ω is the **vorticity** magnitude, d is the **distance** from the **wall**, and f_w , and f_{v2} are **model functions**.

The **model constants and functions** are:

$$c_{b1} = 0.1355, c_{b2} = 0.622, c_{b3} = 2/3, c_{v1} = 7.1, c_{w1} = c_{b1}/\kappa^2 + (1 + c_{b2})/c_{b3}, c_{w2} = 0.3, c_{w3} = 2,$$

$$f_{v2} = 1 - \chi/(1 + \chi f_{v1}), \quad (\text{B-16})$$

$$f_{v1} = \chi^3/(\chi^3 + c_{v1}^3), \quad (\text{B-17})$$

$$\chi = \check{\nu}/\bar{\nu}, \quad (\text{B-18})$$

$$f_w = g((1 + c_{w3}^6)/(g^6 + c_{w3}^6))^{(1/6)}, \quad (\text{B-19})$$

$$g = r + c_{w2}(r^6 - r), \quad (\text{B-20})$$

$$\check{r} = \check{\nu}/(\check{S}\kappa^2 y_w^2), \quad (\text{B-21})$$

$$\Omega = \sqrt{2W_{rz}W_{rz}}, \quad W_{rz} = (1/2)(\partial\tilde{u}_r/\partial z - \partial\tilde{u}_z/\partial r). \quad (\text{B-22})$$

Boundary conditions for the scalar:

$$\check{\nu}_w = 0. \quad (\text{B-23})$$

B-2 Semi-Locally scaled transport equations

The modification of diffusion term in turbulent transport equations as reported by Otero et al. [35] is inserted below.

B-2-1 Myong Kasagi turbulence model

TKE diffusion terms:

$$\frac{1}{\sqrt{\bar{\rho}}} \frac{\partial}{\partial z} \left[\frac{1}{\sqrt{\bar{\rho}}} \left(\frac{\bar{\mu}}{Re_{\tau,0}} + \frac{\mu_t}{\sigma_k} \right) \frac{\partial \bar{\rho} \tilde{k}}{\partial z} \right] + \frac{1}{\sqrt{\bar{\rho}}} \frac{\partial}{\partial r} \left[\frac{r}{\sqrt{\bar{\rho}}} \left(\frac{\bar{\mu}}{Re_{\tau,0}} + \frac{\mu_t}{\sigma_k} \right) \frac{\partial \bar{\rho} \tilde{k}}{\partial r} \right] \quad (\text{B-24})$$

TKE dissipation diffusion terms:

$$\frac{1}{\bar{\rho}} \frac{\partial}{\partial z} \left[\frac{1}{\sqrt{\bar{\rho}}} \left(\frac{\bar{\mu}}{Re_{\tau,0}} + \frac{\mu_t}{\sigma_\epsilon} \right) \frac{\partial \bar{\rho}^{1.5} \tilde{\epsilon}}{\partial z} \right] + \frac{1}{\bar{\rho}} \frac{\partial}{\partial r} \left[\frac{r}{\sqrt{\bar{\rho}}} \left(\frac{\bar{\mu}}{Re_{\tau,0}} + \frac{\mu_t}{\sigma_\epsilon} \right) \frac{\partial \bar{\rho}^{1.5} \tilde{\epsilon}}{\partial r} \right] \quad (\text{B-25})$$

Also, instead of y^+ , y^* should be used in the damping functions.

B-2-2 Menter's $k - \omega$ SST turbulence model

TKE diffusion terms: Equation B-25

TKE dissipation diffusion terms:

$$\frac{\partial}{\partial z} \left[\frac{1}{\sqrt{\bar{\rho}}} \left(\frac{\bar{\mu}}{Re_{\tau,0}} + \sigma_{\omega} \mu_t \right) \frac{\partial \sqrt{\bar{\rho}} \tilde{\omega}}{\partial z} \right] + \frac{1}{r} \frac{\partial}{\partial r} \left[\frac{r}{\sqrt{\bar{\rho}}} \left(\frac{\bar{\mu}}{Re_{\tau,0}} + \sigma_{\omega} \mu_t \right) \frac{\partial \sqrt{\bar{\rho}} \tilde{\omega}}{\partial r} \right] \quad (\text{B-26})$$

B-2-3 Spalart-Allmaras turbulence model

Diffusion terms for the scalar $\check{\nu}$:

$$\begin{aligned} \frac{c_{b2}}{\bar{\rho} c_{b3}} \left[\left(\frac{\partial \sqrt{\bar{\rho}} \check{\nu}}{\partial z} \right)^2 + \left(\frac{\partial \sqrt{\bar{\rho}} \check{\nu}}{\partial r} \right)^2 \right] + \frac{1}{\bar{\rho} c_{b3}} \left[\frac{\partial}{\partial z} \left[\bar{\rho} \left(\frac{\bar{\nu}}{Re_{\tau,0}} + \check{\nu} \right) \left(\frac{\partial \check{\nu}}{\partial z} + \frac{\check{\nu}}{2\bar{\rho}} \frac{\partial \bar{\rho}}{\partial z} \right) \right] \right. \\ \left. + \frac{1}{r} \frac{\partial}{\partial r} \left[\bar{\rho} r \left(\frac{\bar{\nu}}{Re_{\tau,0}} + \check{\nu} \right) \left(\frac{\partial \check{\nu}}{\partial r} + \frac{\check{\nu}}{2\bar{\rho}} \frac{\partial \bar{\rho}}{\partial r} \right) \right] \right] \quad (\text{B-27}) \end{aligned}$$

C-1 RANS Code Validation

This section will provide the validation of the RANS solver used for this thesis. The DNS data from Pirozzoli et al. (2021) [49] has been used for this purpose. A constant property fully developed turbulent flow at $Re_\tau = 495$ has been chosen from the paper as reference data. Plots are attached for Reynolds shear stress and streamwise velocity, for MK [19], SA [32] and Menter's $k - \omega$ SST [31] turbulence models in figures C-1 and C-2.

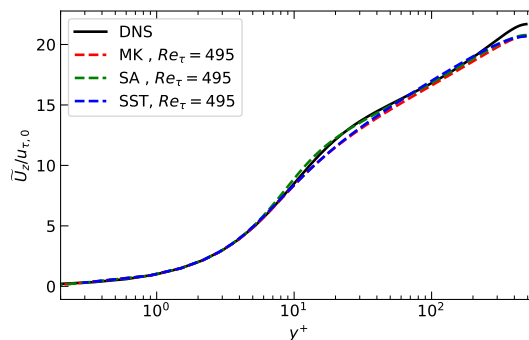


Figure C-1: Validation: streamwise velocity vs y^+

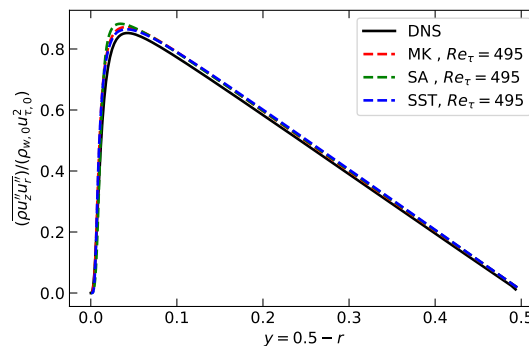


Figure C-2: Validation: Reynolds shear stress vs y

Bibliography

- [1] H. Nemati, A. Patel, B. J. Boersma, and R. Pecnik, “Mean statistics of a heated turbulent pipe flow at supercritical pressure,” *International Journal of Heat and Mass Transfer*, vol. 83, pp. 741–752, 2015.
- [2] “Supercritical water oxidation (scwo), wikipedia.”
- [3] H. Wang, L. K. Leung, W. Wang, and Q. Bi, “A review on recent heat transfer studies to supercritical pressure water in channels,” *Applied Thermal Engineering*, vol. 142, pp. 573–596, 2018.
- [4] J. He, R. Tian, P. Jiang, and S. He, “Turbulence in a heated pipe at supercritical pressure,” *Journal of Fluid Mechanics*, vol. 920, p. A45, 2021.
- [5] L. Tong, “Boiling crisis and critical heat flux.,” 1972.
- [6] H. Li, H. Wang, Y. Luo, H. Gu, X. Shi, T. Chen, E. Laurien, and Y. Zhu, “Experimental investigation on heat transfer from a heated rod with a helically wrapped wire inside a square vertical channel to water at supercritical pressures,” *Nuclear Engineering and Design*, vol. 239, no. 10, pp. 2004–2012, 2009.
- [7] A. Patel, “Turbulence modeling for heat transfer to supercritical pipe flows (msc. thesis),” 2013.
- [8] M. V. Morkovin, “Effects of compressibility on turbulent flows,” *Mécanique de la Turbulence*, vol. 367, no. 380, p. 26, 1962.
- [9] J. W. R. Peeters, R. Pecnik, M. Rohde, T. van der Hagen, and B. Boersma, “Turbulence attenuation in simultaneously heated and cooled annular flows at supercritical pressure,” *Journal of Fluid Mechanics*, vol. 799, p. 505–540, 2016.
- [10] B. Sundén, “Advanced heat transfer topics in complex duct flows,” in *Advances in Heat Transfer*, vol. 49, pp. 37–89, Elsevier, 2017.
- [11] J. Y. Yoo, “The turbulent flows of supercritical fluids with heat transfer,” *Annual review of fluid mechanics*, vol. 45, pp. 495–525, 2013.
- [12] S. He, P.-X. Jiang, Y.-J. Xu, R.-F. Shi, W. Kim, and J. Jackson, “A computational study of convection heat transfer to co2 at supercritical pressures in a vertical mini tube,” *International journal of thermal sciences*, vol. 44, no. 6, pp. 521–530, 2005.

-
- [13] S. He, W. Kim, and J. Jackson, "A computational study of convective heat transfer to carbon dioxide at a pressure just above the critical value," *Applied Thermal Engineering*, vol. 28, no. 13, pp. 1662–1675, 2008.
- [14] S. He, W. Kim, P. Jiang, and J. Jackson, "Simulation of mixed convection heat transfer to carbon dioxide at supercritical pressure," *Proceedings of the Institution of Mechanical Engineers, Part C: Journal of Mechanical Engineering Science*, vol. 218, no. 11, pp. 1281–1296, 2004.
- [15] B. E. Launder and B. I. Sharma, "Application of the energy-dissipation model of turbulence to the calculation of flow near a spinning disc," *Letters in heat and mass transfer*, vol. 1, no. 2, pp. 131–137, 1974.
- [16] K.-Y. Chien, "Predictions of channel and boundary-layer flows with a low-reynolds-number turbulence model," *AIAA journal*, vol. 20, no. 1, pp. 33–38, 1982.
- [17] K. Bremhorst, "Modified form of the kw model for predicting wall turbulence," *Journal of Fluid Engineering*, vol. 103, pp. 456–460, 1981.
- [18] D. C. Wilcox, "Reassessment of the scale-determining equation for advanced turbulence models," *AIAA journal*, vol. 26, no. 11, pp. 1299–1310, 1988.
- [19] H. K. Myong and N. Kasagi, "A new approach to the improvement of k- ϵ turbulence model for wall-bounded shear flows," *JSME international journal. Ser. 2, Fluids engineering, heat transfer, power, combustion, thermophysical properties*, vol. 33, no. 1, pp. 63–72, 1990.
- [20] S. He, W. Kim, and J. Bae, "Assessment of performance of turbulence models in predicting supercritical pressure heat transfer in a vertical tube," *International Journal of Heat and Mass Transfer*, vol. 51, no. 19-20, pp. 4659–4675, 2008.
- [21] Z. Yang and T.-H. Shih, "New time scale based k-epsilon model for near-wall turbulence," *AIAA journal*, vol. 31, no. 7, pp. 1191–1198, 1993.
- [22] K. Abe, T. Kondoh, and Y. Nagano, "A new turbulence model for predicting fluid flow and heat transfer in separating and reattaching flows—i. flow field calculations," *International journal of heat and mass transfer*, vol. 37, no. 1, pp. 139–151, 1994.
- [23] M. Behnia, S. Parneix, and P. A. Durbin, "Prediction of heat transfer in an axisymmetric turbulent jet impinging on a flat plate," *International journal of heat and mass transfer*, vol. 41, no. 12, pp. 1845–1855, 1998.
- [24] C.-R. Zhao, Z. Zhang, P.-X. Jiang, and H.-L. Bo, "Influence of various aspects of low reynolds number k- ϵ turbulence models on predicting in-tube buoyancy affected heat transfer to supercritical pressure fluids," *Nuclear Engineering and Design*, vol. 313, pp. 401–413, 2017.
- [25] A. Pucciarelli, I. Borroni, M. Sharabi, and W. Ambrosini, "Results of 4-equation turbulence models in the prediction of heat transfer to supercritical pressure fluids," *Nuclear Engineering and Design*, vol. 281, pp. 5–14, 2015.
- [26] J. H. Bae, J. Y. Yoo, and H. Choi, "Direct numerical simulation of turbulent supercritical flows with heat transfer," *Physics of fluids*, vol. 17, no. 10, p. 105104, 2005.
- [27] A. Patel, J. W. Peeters, B. J. Boersma, and R. Pecnik, "Semi-local scaling and turbulence modulation in variable property turbulent channel flows," *Physics of Fluids*, vol. 27, no. 9, p. 095101, 2015.

- [28] S. He, K. He, and M. Seddighi, "Laminarisation of flow at low reynolds number due to streamwise body force," *Journal of Fluid mechanics*, vol. 809, pp. 31–71, 2016.
- [29] F. Nieuwstadt, B. Boersma, and J. Westerweck, *Introduction to Theory and Applications of Turbulent Flows*. Springer, 2016.
- [30] P. Huang, G. Coleman, and P. Bradshaw, "Compressible turbulent channel flows: Dns results and modeling," *Journal of Fluid Mechanics*, vol. 305, pp. 185–218, 1995.
- [31] F. Menter, "Zonal two equation kw turbulence models for aerodynamic flows," in *23rd fluid dynamics, plasmadynamics, and lasers conference*, p. 2906, 1993.
- [32] P. Spalart and S. Allmaras, "A one-equation turbulence model for aerodynamic flows," in *30th aerospace sciences meeting and exhibit*, p. 439, 1992.
- [33] N. Ince and B. Launder, "Three-dimensional and heat-loss effects on turbulent flow in a nominally two-dimensional cavity," *International journal of heat and fluid flow*, vol. 16, no. 3, pp. 171–177, 1995.
- [34] R. Pecnik and A. Patel, "Scaling and modelling of turbulence in variable property channel flows," *Journal of Fluid Mechanics*, vol. 823, p. R1, 2017.
- [35] A. Patel, R. Diez, R. Pecnik, *et al.*, "Turbulence modelling for flows with strong variations in thermo-physical properties," *International Journal of Heat and Fluid Flow*, vol. 73, pp. 114–123, 2018.
- [36] S. Smit, "Rans code to solve turbulent pipe flow with a fluid undergoing heat transfer at supercritical pressure." Available at https://github.com/Fluid-Dynamics-Of-Energy-Systems-Team/RANS_pipe.
- [37] B. Koren, *A robust upwind discretization method for advection, diffusion and source terms*, vol. 45. Centrum voor Wiskunde en Informatica Amsterdam, 1993.
- [38] A. Patel, B. J. Boersma, and R. Pecnik, "The influence of near-wall density and viscosity gradients on turbulence in channel flows," *Journal of Fluid Mechanics*, vol. 809, pp. 793–820, 2016.
- [39] S. Silvestri and R. Pecnik, "Turbulence modulation in thermally expanding and contracting flows," *Journal of Fluid Mechanics*, vol. 926, p. A30, 2021.
- [40] R. S. Weinberg, *Experimental and theoretical study of buoyancy effects in forced convection to supercritical pressure carbon dioxide*. PhD thesis, University of Manchester, 1972.
- [41] P.-X. Jiang, Y.-J. Xu, J. Lv, R.-F. Shi, S. He, and J. Jackson, "Experimental investigation of convection heat transfer of co2 at super-critical pressures in vertical mini-tubes and in porous media," *Applied Thermal Engineering*, vol. 24, no. 8-9, pp. 1255–1270, 2004.
- [42] J. Fewster and J. Jackson, "Some experiments on heat transfer to carbon dioxide at supercritical pressure in tubes," in *Proceedings of the International Congress on Advances in Nuclear Power Plants (ICAPP'04), Pittsburgh, PA, USA, 2004*.
- [43] M. J. Watts, *Heat transfer to supercritical pressure water: Mixed convection with upflow or downflow in a vertical tube*. PhD thesis, The University of Manchester, 1980.
- [44] J. Jackson, "Heat transfer studies at manchester with carbon dioxide at supercritical and near-critical pressures," *Report produced for AECL in connection with the database on SCWR Heat Transfer being established by IAEA, Ref. JDJ/IAEA/CRP/Report*, no. 1, 2009.

-
- [45] K. Abe, T. Kondoh, and Y. Nagano, “A new turbulence model for predicting fluid flow and heat transfer in separating and reattaching flows—ii. thermal field calculations,” *International Journal of Heat and Mass Transfer*, vol. 38, no. 8, pp. 1467–1481, 1995.
- [46] B. Deng, W. Wu, and S. Xi, “A near-wall two-equation heat transfer model for wall turbulent flows,” *International journal of heat and mass transfer*, vol. 44, no. 4, pp. 691–698, 2001.
- [47] H. Zhang, Z. Xie, and Y. Yang, “Numerical study on supercritical fluids flow and heat transfer under buoyancy,” in *The 8th International Topical Meeting on Nuclear Thermal-Hydraulics, Operation and Safety (NUTHOS-8), Shanghai, China*, pp. 10–14, 2010.
- [48] Z.-H. Li, P.-X. Jiang, C.-R. Zhao, and Y. Zhang, “Experimental investigation of convection heat transfer of co2 at supercritical pressures in a vertical circular tube,” *Experimental thermal and fluid science*, vol. 34, no. 8, pp. 1162–1171, 2010.
- [49] S. Pirozzoli, J. Romero, M. Fatica, R. Verzicco, and P. Orlandi, “One-point statistics for turbulent pipe flow up to,” *Journal of fluid mechanics*, vol. 926, p. A28, 2021.